CRREL
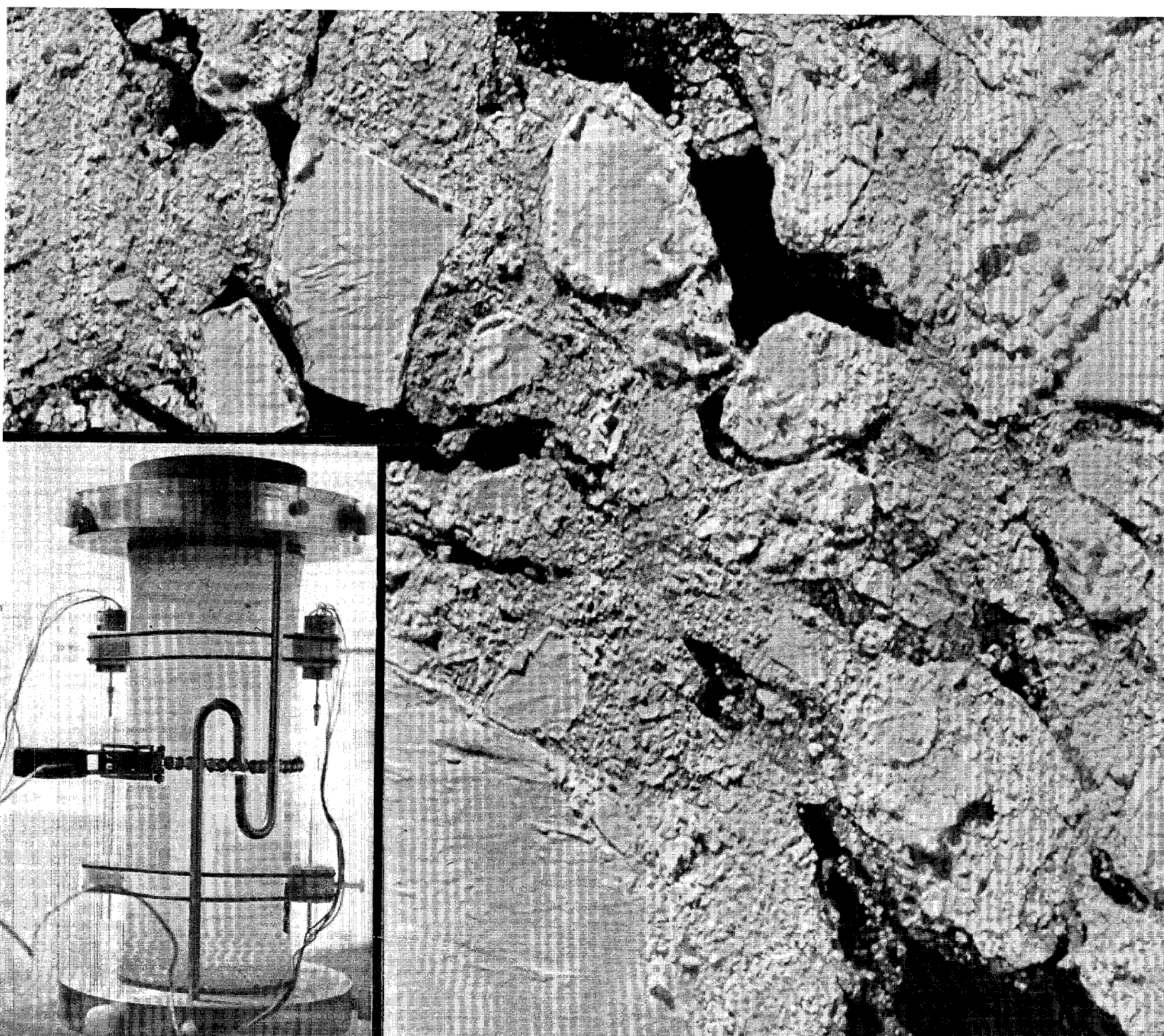## REPORT 85-16

**US Army Corps
of Engineers**

Cold Regions Research &
Engineering Laboratory

Mechanical properties of multi-year sea ice
Phase II: Test results

*For conversion of SI metric units to U.S./British
customary units of measurement consult ASTM
Standard E380,* Metric Practice Guide, *published
by the American Society for Testing and Materi-
als, 1916 Race St., Philadelphia, Pa. 19103.*

*Cover: An instrumented test specimen super-
imposed over aerial photograph of
pack ice in the Beaufort Sea.*

REPORT DOCUMENTATION PAGE		READ INSTRUCTIONS BEFORE COMPLETING FORM
1. REPORT NUMBER CRREL Report 85-16	2. GOVT ACCESSION NO.	3. RECIPIENT'S CATALOG NUMBER
4. TITLE *(and Subtitle)* MECHANICAL PROPERTIES OF MULTI-YEAR SEA ICE Phase II: Test Results		5. TYPE OF REPORT & PERIOD COVERED
		6. PERFORMING ORG. REPORT NUMBER
7. AUTHOR(s) G.F.N. Cox, J.A. Richter-Menge, W.F. Weeks, H. Bosworth, N. Perron, M. Mellor and G. Durell		8. CONTRACT OR GRANT NUMBER(s)
9. PERFORMING ORGANIZATION NAME AND ADDRESS U.S. Army Cold Regions Research and Engineering Laboratory Hanover, New Hampshire 03755-1290		10. PROGRAM ELEMENT, PROJECT, TASK AREA & WORK UNIT NUMBERS
11. CONTROLLING OFFICE NAME AND ADDRESS Minerals Management Service U.S. Department of Interior Reston, Virginia 22092		12. REPORT DATE October 1985
		13. NUMBER OF PAGES 89
14. MONITORING AGENCY NAME & ADDRESS*(If different from Controlling Office)*		15. SECURITY CLASS. *(of this report)* Unclassified
		15a. DECLASSIFICATION/DOWNGRADING SCHEDULE

16. DISTRIBUTION STATEMENT *(of this Report)*

Approved for public release; distribution unlimited.

17. DISTRIBUTION STATEMENT *(of the abstract entered in Block 20, if different from Report)*

18. SUPPLEMENTARY NOTES

19. KEY WORDS *(Continue on reverse side if necessary and identify by block number)*
Ice
Ice properties
Mechanical properties
Sea ice

20. ABSTRACT *(Continue on reverse side if necessary and identify by block number)*
This report presents the results of the second phase of a test program designed to obtain a comprehensive understanding of the mechanical properties of multi-year sea ice from the Alaskan Beaufort Sea. In Phase II, 62 constant-strain-rate uniaxial compression tests were performed on horizontal and vertical ice samples from multi-year pressure ridges to examine the effect of sample orientation on ice strength. Also conducted were 36 constant-strain-rate tension tests, 55 conventional triaxial tests and 35 constant-load compression tests on multi-year pressure ridge samples to provide data for developing

20. Abstract (cont'd).

ice yield criteria and constitutive laws. Data are presented on the strength, failure strain and modulus of multi-year sea ice under different loading conditions. The effects of ice temperature, porosity, structure, strain rate, confining pressure and sample orientation on the mechanical properties of multi-year sea ice are examined.

PREFACE

The contents of this report are not to be used for advertising or promotional purposes. Citation of brand names does not constitute an official endorsement or approval of the use of such commercial products.

CONTENTS

ILLUSTRATIONS

TABLES

MECHANICAL PROPERTIES OF
MULTI-YEAR SEA ICE
Phase II: Test Results

G.F.N. Cox, J.A. Richter-Menge, W.F. Weeks,
H. Bosworth, N. Perron, M. Mellor and G. Durell

INTRODUCTION

This report presents the test results from the second phase of a continuing, government–industry study designed to obtain a comprehensive understanding of the structure and mechanical properties of ice samples obtained from multi-year pressure ridges. We are particularly interested in the mechanical properties of multi-year ice, as multi-year pressure ridges may govern the design of offshore structures in exposed areas of the Beaufort and Chukchi Seas.

The first phase of the study included a field sampling program in the southern Beaufort Sea, developing a variety of ice testing techniques, and performing a total of 282 uniaxial compression, tension and conventional triaxial tests. In Phase I, the majority of the tests were uniaxial, constant-strain-rate compression tests. We were interested in determining the variation of ice strength within and between each of 10 sampled ridges. These tests were conducted at two strain rates (10^{-5} and 10^{-3} s^{-1}) and two temperatures (-20° and -5°C). In addition, a limited number of constant-strain-rate tension, constant-load compression and conventional triaxial tests were performed on ice samples obtained from a multi-year floe. We did these tests to establish our testing techniques and procedures. The results from Phase I are given in three reports: Mellor et al. (1984) describe the testing techniques used in the program, Cox et al. (1984) present the test results, and Rand and Mellor (in prep.) describe the coring equipment specially developed for this study to obtain 4¼-in. (10.8-cm) diameter core.

In Phase II, ice samples were again obtained from multi-year pressure ridges in the Beaufort Sea and shipped to CRREL for testing. As no significant difference was found between the mean strength of ridges during Phase I, sampling was restricted to four ridges to simplify the logistics. Unlike Phase I, the tests in Phase II were divided among constant-strain-rate compression and tension, constant-load compression and triaxial tests. There were a total of 188 tests.

This report includes a discussion of the field sampling program and presents the test results of the second phase of the program. The sample preparation and testing techniques used in Phase II have already been described in detail by Mellor et al. (1984).

FIELD SAMPLING PROGRAM

We had originally scheduled the field program for the first two weeks of April, as in Phase I. However, delays associated with establishing the funding level of the project prevented the field operation from starting until 14 April 1982. We were very concerned that a period of warm weather would cause us difficulties, such that we would have to pack the ice sample boxes with dry ice while at the sampling sites. Fortunately, this did not occur. We were also favored with extremely good flying and working weather (limited ice fog and light winds). This good fortune, combined with the excellent performance of our coring systems, allowed us to exceed our sampling goals and complete the program in 10 days. We mention this good fortune to stress the point that, in planning field programs, such optimal working conditions and system performance cannot be relied upon.

Under more typical conditions we estimate that our field program could have taken up to 16 days to complete.

Site selection and description

During the winter of 1982, there were relatively few multi-year floes with ridges in the Prudhoe Bay area. Fortunately, we were able to arrange for ice reconnaissance flights by Shell and Oceanographic Services. As these flights were completed before we arrived in Deadhorse, we were able to fly directly to the most likely locations in our area to select ridges for sampling. Even so, we found it difficult to select suitable ridges as the majority of the multi-year floes were quite small and the ridges were unimpressive. In addition, many of the ridges appeared to be located on second-year ice. The ridge profiles were still somewhat blocky and the surfaces of the undeformed floes did not show well-developed melt relief. Based on the 1981 sampling program, we found that second-year ridges contained a large number of voids. Ice from such ridges provides relatively few good test specimens as it is difficult to obtain suitably long cores. We finally selected a floe north of Leavitt Island where a number of floes that were near to each other contained several well-rounded ridges that we estimated to be at least two summers old (Fig. 1). The first sampling location (ridge A) was on a thick multi-year floe with lateral dimensions of roughly 50 m. Although the ice had been deformed, there were no clearly delineated linear

ridges. Therefore, we chose two of our sampling locations on high points and two sampling locations in swales. A sketch map showing the general topography of the sampling area is given in Figure 2. Figure 3 shows an oblique aerial photograph of the site (located in the foreground). The small, one-room building (which was transported to the site by helicopter) provides a sense of scale. Figure 4 shows a surface view of the floe. The 1- to 1.5-m freeboard is evident. A total of 11 sites were sampled at this location for a total core length of 48.70 m. The ice at this location was generally characterized by a high volume of included air as compared with the ridges that we had sampled in 1981. We therefore decided to sample several other ridges in the vicinity to see if they also contained large amounts of air, or if perhaps they would prove to be similar to the ridges we sampled during Phase I.

These ridges were found on two floes located approximately 200 m to the north of our first sampling area. The second ridge (ridge B) was approximately 27 m long and was located on the smaller of these two floes (Fig. 5). It is possible that these two floes were initially part of the same larger floe, which had been split. The ice proved to be quite solid and massive with significantly less air voids. A sketch of a profile of this ridge showing the location of specific core sites is given in Figure 6. Note the sharp vertical termination of the ridge on the "right-hand" edge of the floe. The total length of core obtained from this ridge was 50.32 m.
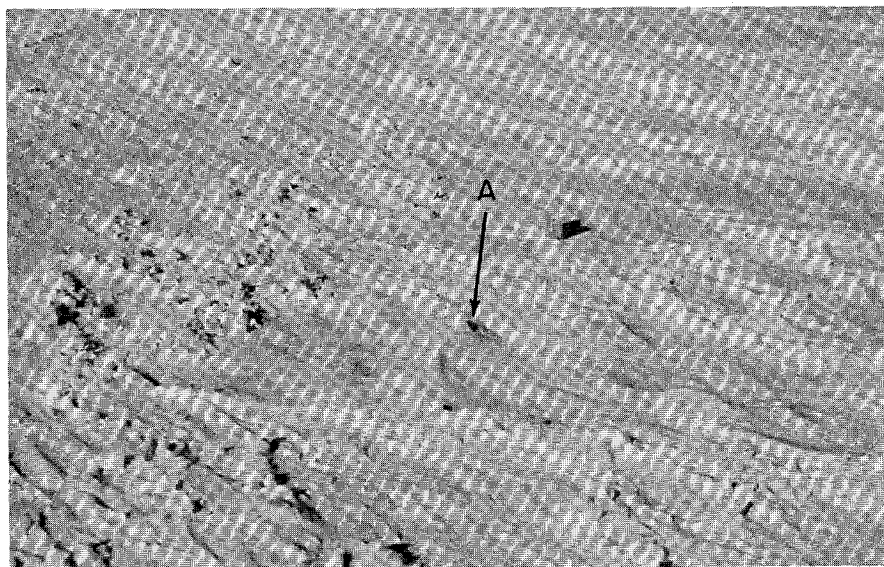
Figure 1. Aerial view of multi-year floe, designated as ridge A, where first 11 cores were obtained.
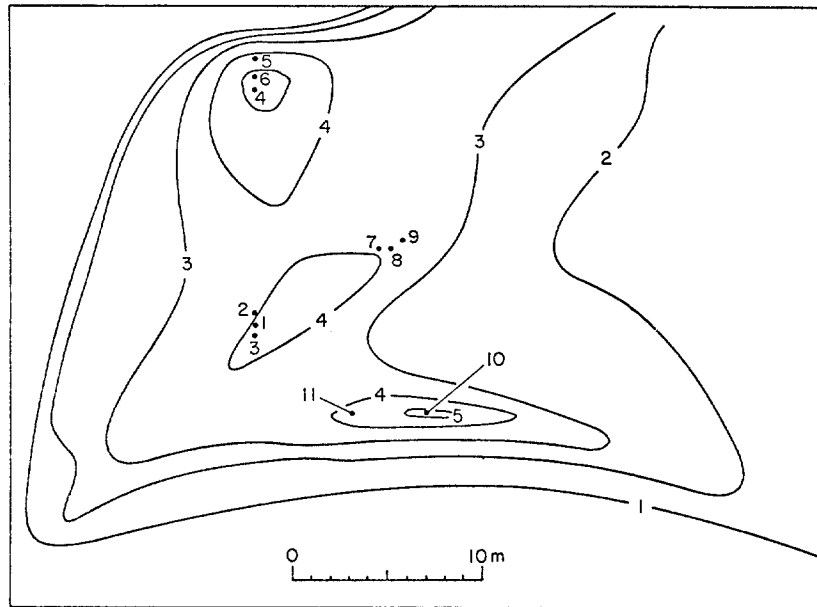
Figure 2. Sketch map of ridge A showing location of the ice sampling sites (contours in metres).

Figure 3. Oblique aerial view of ridge A sampling site.

3

Figure 4. Surface view of ridge A sampling site.
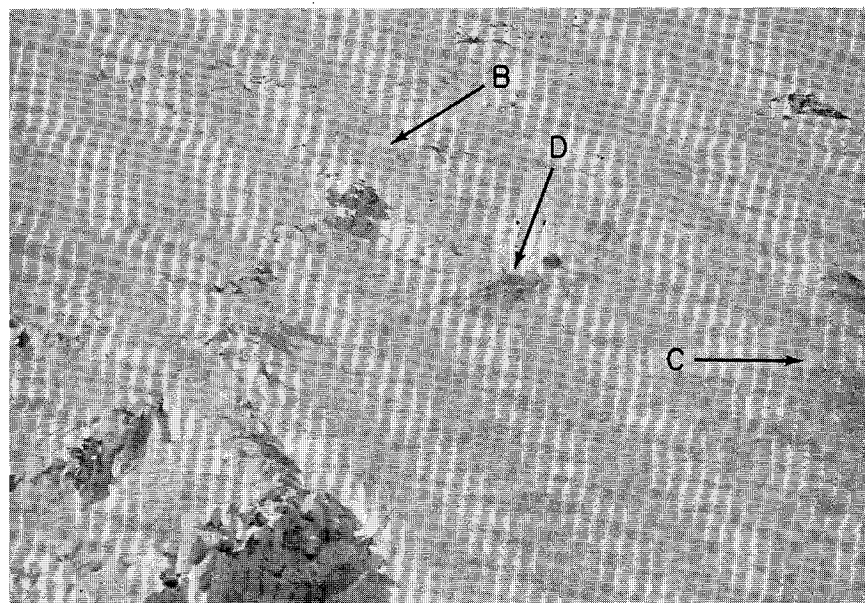
Figure 5. Aerial view of sampling area containing ridges B, C and D.
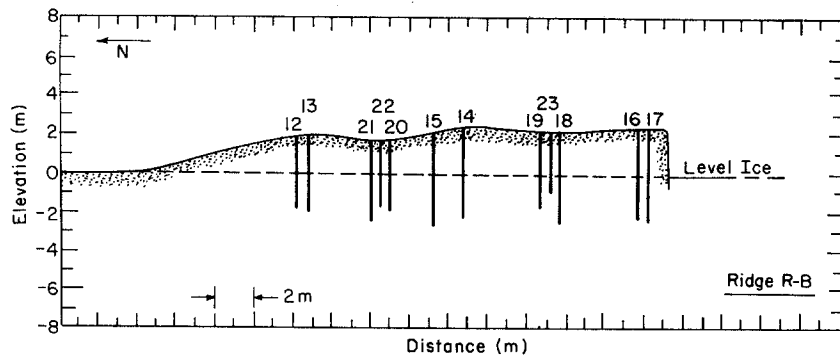
Figure 6. Sketch of ridge B profile showing the location of the ice sampling sites.
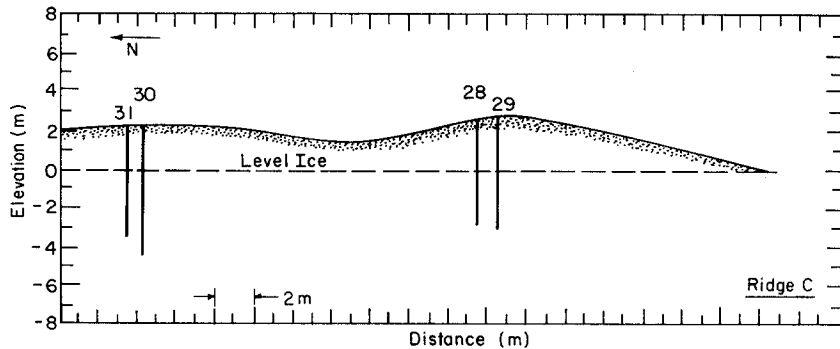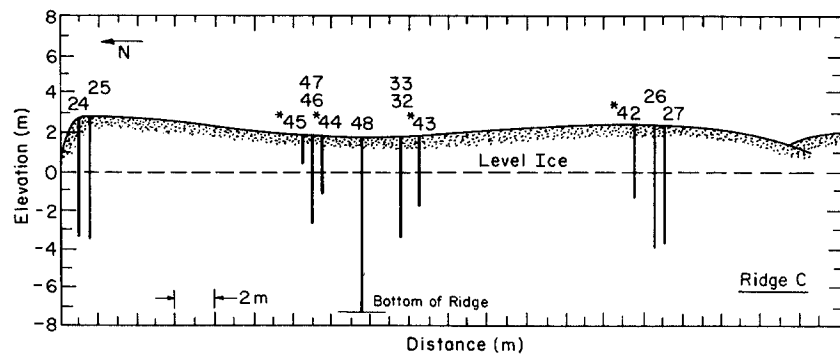
Figure 7. Sketch of ridge C profile showing the location of the ice sampling sites (*30.5-cm [12-in.] holes).

The third ridge sampled was approximately 75 m long and was the largest ridge on the adjoining floe. A profile of this ridge (ridge C) is given in Figure 7. Figure 5 shows an aerial view of this ridge as well as of ridges B and D. Ridge C, although broad, was quite clearly defined. Figure 8 shows coring underway on this ridge. A total of 67.11 m of core were obtained from this ridge for use as test specimens. A 9.53-m core was also obtained through the ridge to use in petrographic studies.

The last ridge sampled ran roughly parallel to ridge C. Ridge D can also be seen in Figure 5. This ridge was 53.6 m in length and was clearly delineated. Figure 9 shows the split end of the ridge where its blocky deformed structure could be examined. The total core recovery from ridge D was 47.93 m.

In addition, 3.83 m of core were obtained from a floe that appeared to contain undeformed multiyear ice. Figure 10 shows an aerial view of the site. Table 1 summarizes the height of the top of each

5
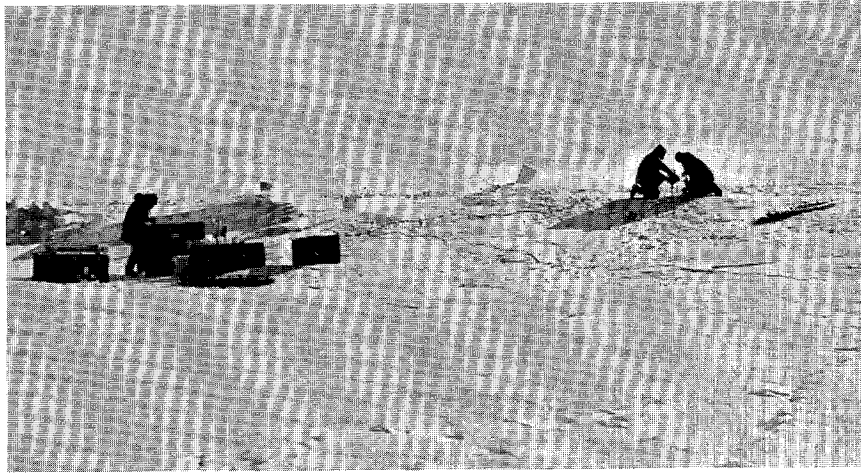
Figure 8. Coring operation on ridge C.
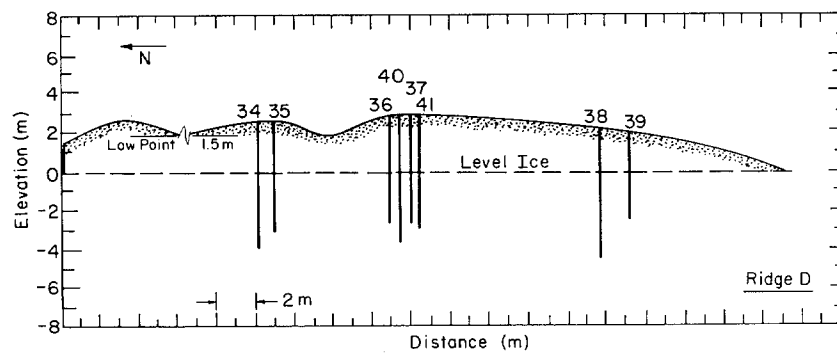
a. Sketch of ridge D profile showing the location of the sampling sites.

b. Split end portion.

Figure 9. Ridge D.

6
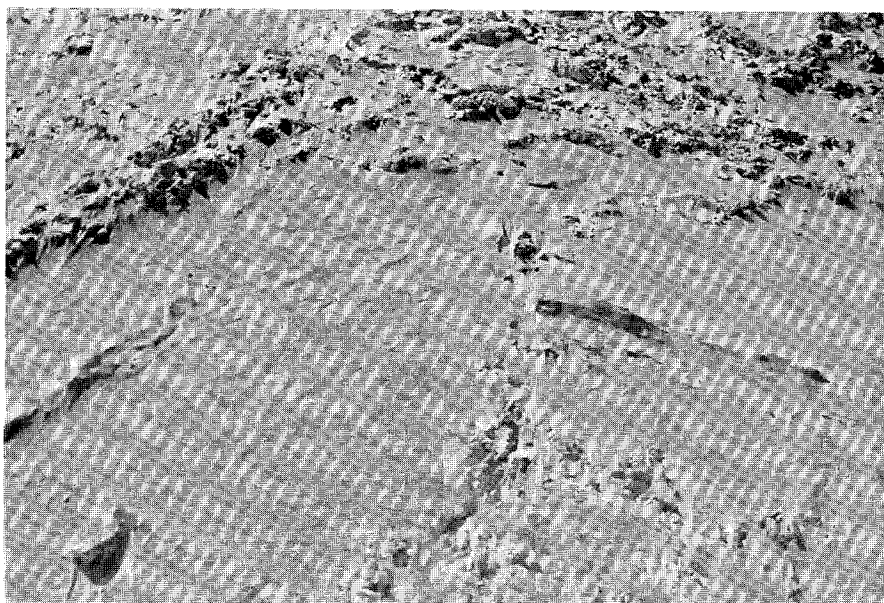
Figure 10. Aerial view of multi-year floe where undeformed samples were obtained.

core hole above level ice (approxiate sea level). The heights were estimated using a hand level. Also given is the penetration depth (the total length cored from each hole). Table 2 gives the daily drilling log and Table 3 provides a summary of these data. The primary part of the coring program was carried out with the 4¼-in. (10.8-cm) corer in four days (15–18 April) with a total of 205.6 m of core recovered. The total number of vertical samples obtained from this core were 439 or roughly 100 samples per day. The total length of 12-in. (30.5-cm) diameter core obtained was 12.79 m, which resulted in 61 horizontal specimens, giving a grand total of 500 specimens for the season. As mentioned earlier, we also obtained 9.53 m of core for petrographic studies.

Coring procedures

Much of the success of the field program can be credited to the efficiency with which our coring equipment obtained the samples. The 4¼-in.-diameter coring augers were the same augers that were used in 1981, with some important modifications. In 1981, we experienced difficulty with the core dogs. They did not grip the sample firmly to produce a clean break at the base of the core. Instead the dogs frequently made long gouges in the sides of the samples. These gouges were of sufficient depth such that the gouged ice could not be used for test specimens. During the 1982 field season, this problem was resolved. A new core dog was designed and built to provide a better cutting edge. An inverted impact hammer was also added to give the extension rods a sharp upward impact. This impact both seated the dogs and caused the core to break cleanly at the bottom of the hole. Figure 11 shows the impact hammer in use. A third change that was made to the 4¼-in. coring system was the addition of a short length of helical flighting directly above the augers. This kept snow from packing into the top of the core barrel and reduced the friction when the core barrel was being removed from the hole. The helical flighting can be seen in Figure 12. We believe that this attachment allowed the drillers to obtain longer cores than those obtained in 1981, ranging in length from 100 cm to a maximum of 128 cm.

The major addition to the coring equipment in Phase II was a 12-in. (30.5-cm) diameter coring system. Large diameter core was needed to provide horizontal test specimens from deep within the ridges. The auger itself was designed to obtain 12-in.-diameter samples up to 1 m in length. Simply stated, it was an exploded version of the 4¼-in. auger. Figure 13 shows the auger attached to the winch and drive system. A commercial, gasoline-powered post hole digger was modified to provide the rotation and lifting requirements to operate the drill. Figure 14 shows the mobile drilling rig winching itself up a pressure ridge.

The following procedure was used to obtain the large-diameter core and horizontal test samples.

7

Table 1. Ridge heights (above estimated sea level) and penetration depths, April 1982.

Location	Date	Hole no.	Height (cm)	(ft)	Depth (cm)	(ft)	Diameter (cm)*	Remarks
Ridge A	15 April	1	230	7.7	461	15.0	10.8	
		2	234	7.7	384	12.6	10.8	
		3	234	7.7	473	14.3	10.8	
		4	300	9.8	581	19.1	10.8	
		5	345	11.3	454	14.9	10.8	
		6	300	9.8	502	16.5	10.8	
		7	234	7.7	373	12.2	10.8	
		8	234	7.7	373	12.2	10.8	
		9	234	7.7	377	12.4	10.8	
		10	503	16.5	601	19.7	10.8	
		11	406	13.3	327	10.7	10.8	
Ridge B	16 April	12	203	6.7	380	12.5	10.8	
		13	203	6.7	409	13.4	10.8	
		14	249	8.2	472	15.5	10.8	
		15	218	7.2	479	15.7	10.8	
		16	249	8.2	473	15.5	10.8	
		17	249	8.2	482	15.8	10.8	
		18	234	7.7	473	15.5	10.8	
		19	234	7.7	396	13.0	10.8	
		20	185	6.1	361	11.8	10.8	
		21	185	6.1	427	14.0	10.8	
		22	185	6.1	354	11.6	10.8	
		23	234	7.7	326	10.7	10.8	
Ridge C	17 April	24	269	8.8	624	20.5	10.8	
		25	269	8.8	639	21.0	10.8	
		26	234	7.7	652	21.4	10.8	
		27	234	7.7	544	17.8	10.8	
		28	269	8.8	565	18.5	10.8	
		29	269	8.8	558	18.3	10.8	
		30	221	7.3	680	22.3	10.8	
		31	221	7.3	576	18.9	10.8	
		32	173	5.7	563	18.5	10.8	Sail height 1.63 m (5.3 ft)
		33	173	5.7	470	15.4	10.8	Water depth 14.1 m (46.3 ft)
	19 April	42	234	7.7	404	13.3	30.3	
	20 April	43	173	5.7	389	12.8	30.3	Sail height 1.63 m (5.3 ft)
		44	173	5.7	323	10.6	30.3	Sail height 1.63 m (5.3 ft)
		45	173	5.7	163	5.3	30.3	Sail height 1.63 m (5.3 ft)
		46	173	5.7	364	11.9	10.8	Sail height 1.63 m (5.3 ft)
		47	173	5.7	476	15.6	10.8	Sail height 1.63 m (5.3 ft)
	22 April	48	173	5.7	953	31.3	10.8	Sail height 1.63 m (5.3 ft)
Ridge D	18 April	34	269	8.8	676	22.2	10.8	
		35	269	8.8	564	18.5	10.8	
		36	300	9.8	567	18.6	10.8	
		37	300	9.8	577	18.9	10.8	
		38	218	7.2	682	22.4	10.8	
		39	218	7.2	466	15.3	10.8	
		40	300	9.8	678	22.2	10.8	
		41	300	9.8	583	19.1	10.8	
Ridge E	22 April	49	30	1.0	383	12.6	10.8	Sail height 0.53 m (1.7 ft)
								Water depth 19.2 m (63 ft)

* 10.8 cm (4.25 in.); 30.3 cm (12 in.).

8

Table 2. Daily core log, April 1982

Location	Date	Hole no.	Total depth (m)	Core lengths (cm)
Ridge A	15 April	1	4.62	122, 108, 100, 94, 37
		2	3.84	122, 112, 97, 53
		3	4.37	119, 115, 98, 66, 39
		4	5.81	128, 102, 102, 94, 100, 55
		5	4.54	122, 92, 91, 102, 46
		6	5.02	126, 104, 100, 96, 76
		7	3.73	121, 112, 95, 45
		8	3.73	127, 103, 105, 38
		9	3.77	125, 106, 99, 47
		10	6.01	127, 101, 105, 92, 105, 71
		11	3.27	74, 48, 98, 107
Ridge B	16 April	12	3.80	127, 105, 56, 32, 40
		13	4.09	130, 91, 108, 80
		14	4.72	115, 111, 104, 96, 46
		15	4.79	118, 107, 106, 98, 50
		16	4.73	119, 105 ,102, 101, 46
		17	4.82	118, 114, 98, 106, 46
		18	4.73	121 ,105, 110, 92, 45
		19	3.96	110, 111, 102, 73
		20	3.61	122, 104, 98, 37
		21	4.27	121, 116, 103, 87
		22	3.54	126, 107, 96, 24
		23	3.26	121, 106, 99
Ridge C	17 April	24	6.24	105, 113, 100, 106, 102, 98
		25	6.39	128, 102, 96, 101, 99, 113
		26	6.52	120, 114, 106, 114, 96, 102
		27	5.44	120, 126, 120, 80, 98
		28	5.65	117, 126, 124, 100, 98
		29	5.58	106, 109, 121, 116, 106
		30	6.80	114, 123, 100, 123, 110, 110
		31	5.76	121, 108, 115, 112, 120
		32	5.63	110, 110, 116, 110, 117
		33	4.70	126, 107, 121, 116
	19 April	42	4.04	96, 82, 100, 60, 66
	20 April	43	3.89	103, 80, 88, 52, 66
		44	3.23	94, 102, 71, 56
		45	1.63	101, 62
		46	3.64	120, 122, 122
		47	4.76	121, 117, 124, 114
	21 April			No drilling—high winds and blowing snow
	22 April	48	9.53	112, 116, 124, 113, 112, 102, 46, 58, 103, 67*
Ridge D	18 April	34	6.76	114, 119, 111, 106, 123, 103
		35	5.64	115, 110, 109, 120, 110
		36	5.67	110, 117, 122, 113, 105
		37	5.77	116, 112, 125, 114, 110
		38	6.82	122, 111, 122, 113, 120, 94
		39	4.66	121, 112, 112, 121
		40	6.78	120, 123, 112, 124, 89, 110
		41	5.83	120, 114, 122, 124, 103
Ridge E	22 April	49	3.83	114, 30, 100, 68, 66*

* Denotes bottom of pressure ridge.

Table 3. Summary of daily drilling, April 1982.

Date	No. of holes	No. of cores	Avg. core length (cm)	Total length of core obtained (m)
15 April	11	52	93	48.7
16 April	12	53	95	50.32
17 April	10	53	110	58.71
18 April	8	42	114	47.93
19 April	1	5	81	4.04
20 April	3	11	79	8.75
	2	7	120	8.4
22 April	2	13	92	13.36

Total length of 10.8-cm (4-in.)-diameter core obtained—226.09 m.

Total length of 30.5-cm (12-in.)-diameter core obtained—12.79 m.

Longest 10.8-cm-diameter core obtained—128 cm; hole 25.

Longest 30.5-cm-diameter core obtained—103 cm; hole 43.

Once the drill had augered approximately 1 m, the drill was removed from the hole. A core retrieval system (Fig. 15) was then lowered into the hole to break and catch the core. A horizontally mounted hydraulic cylinder at the top of the core catcher was next activated to shear the core at the bottom of the hole. Two core dogs located at the bottom of the catcher held the core in the barrel as it was lifted to the surface. The core was then removed from the retrieval system (Fig. 16) and placed in a carrier to move the core to the horizontal sampling drill. To obtain horizontal samples, a simple drill press was designed such that 4¼-in.-diameter cores could be obtained from the 12 in. core. Figure 17 shows this system in operation. The only problem encountered while using this system was drill-induced vibration. This can be easily corrected by adding additional stiffening elements to the drill frame.

The entire 12-in. drilling system was carried to the sampling site by sling-loading the mobile frame under a helicopter. Once on the ground, a winch allowed the operators to maneuver the system to the drilling location.

Core logging procedures

There were some differences in the core logging procedures between the 1981 and 1982 field seasons. As a result of the Phase I testing program, we had found that some of our field measurements did not prove to be particularly useful. For instance, in 1981, we took rather detailed temperature and salinity profiles in the field. As the important temperature is the ice temperature at the time of testing, we reduced the number of temper-

ature measurements in the 1982 field program to three or four per core. This was sufficient to indicate the general temperature profile in the ice. We also reduced the number of subsidiary salinity measurements. We have found that brine drainage is not an important problem in low salinity multi-year ice and our routine laboratory procedures include a salinity determination on each test specimen.

In 1981, we shipped large quantities of extra core back to CRREL for use in petrographic studies. Much of this core had been damaged during extraction when the extended core dogs gouged the core sides instead of cleanly breaking the core off at the bottom of the hole. Such core could not be used for test specimens. In 1982, this problem was resolved and very little damaged core was obtained. We also had found that we were able to save sufficient ice from each 33-cm rough-cut test specimen as collected in the field to provide end pieces for petrographic analysis should the sample be destroyed during the test. Therefore, it was not necessary to ship extra-long test specimens or to include extra ice from each core. Samples were cut to 33-cm lengths in the field. This resulted in a great saving in time and in shipping costs.

Shipping and storage of ice samples

Upon removal from the ice, ice cores were cut to length, cataloged, and packed in core tubes. In Deadhorse, gaps in the core tubes were packed with paper to protect the core ends from damage by excessive motion during shipment. The core tubes were then placed in insulated shipping boxes. The core shipping boxes were constructed of heavy-weight, wax-coated cardboard with 8-cm-thick styrofoam on the bottom, sides, and top of the container. Each box could accommodate six, 1-m-long tubes, snow for packing and dry ice for refrigeration. The shipping boxes were kept in an unheated trailer at ambient temperatures. As temperatures were sufficiently low, it was not necessary to refrigerate the samples. There were no problems with brine drainage.

The ice samples were shipped directly to CRREL in two consignments. Each shipping box was packed with 5 to 8 cm of snow and charged with about 35 kg of dry ice. The snow was placed on top of the core tubes to prevent thermal cracking of the core that might result from direct contact with the dry ice.

The ice samples were shipped via Alaska International Air Cargo (AIA) to Emery Air Freight in Anchorage. Before each shipment left Deadhorse, Emery reserved space on a Flying Tigers flight to

10

Figure 11. Impact hammer used to engage core dogs and break core.
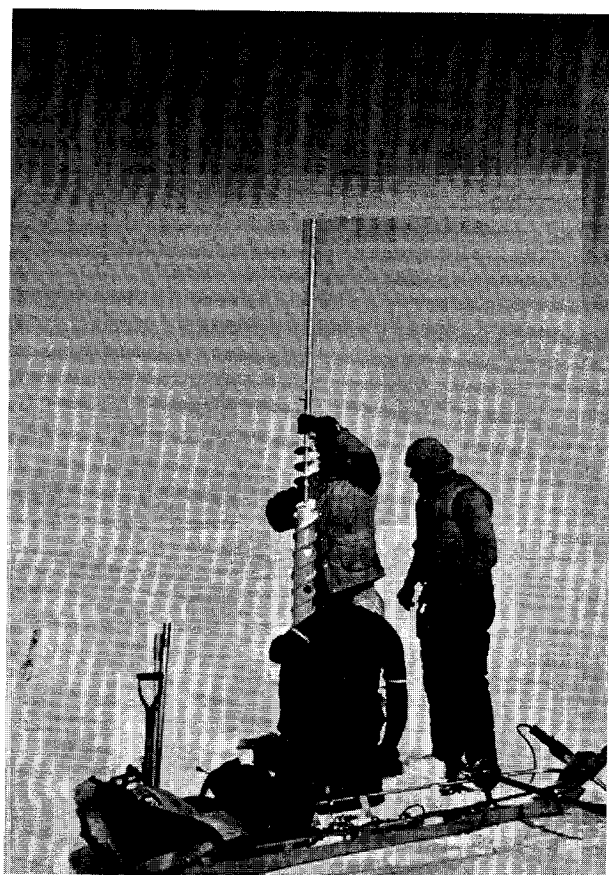
Figure 12. Helical flight on top of core barrel to prevent packing of cuttings above core barrel.
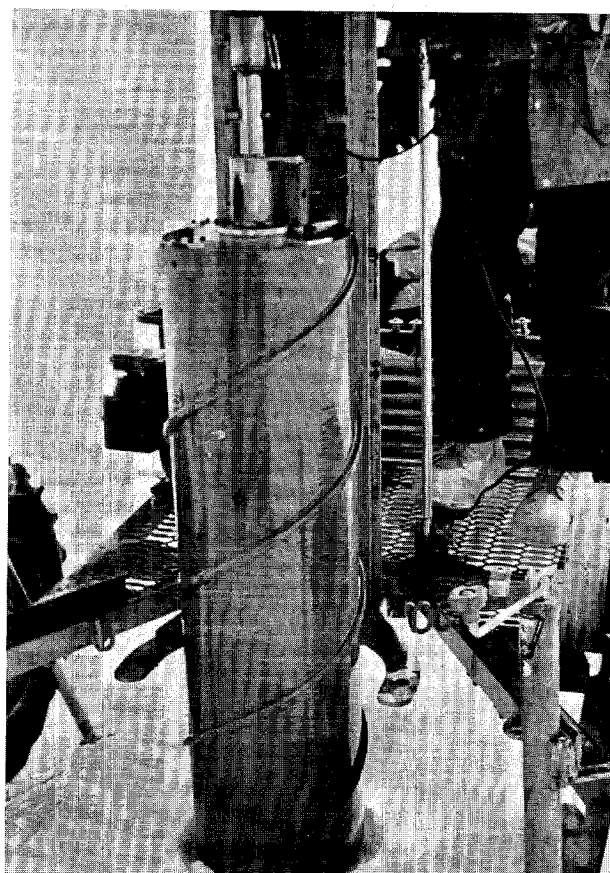
Figure 13. Core barrel with 30.5-cm (12-in.) diameter.
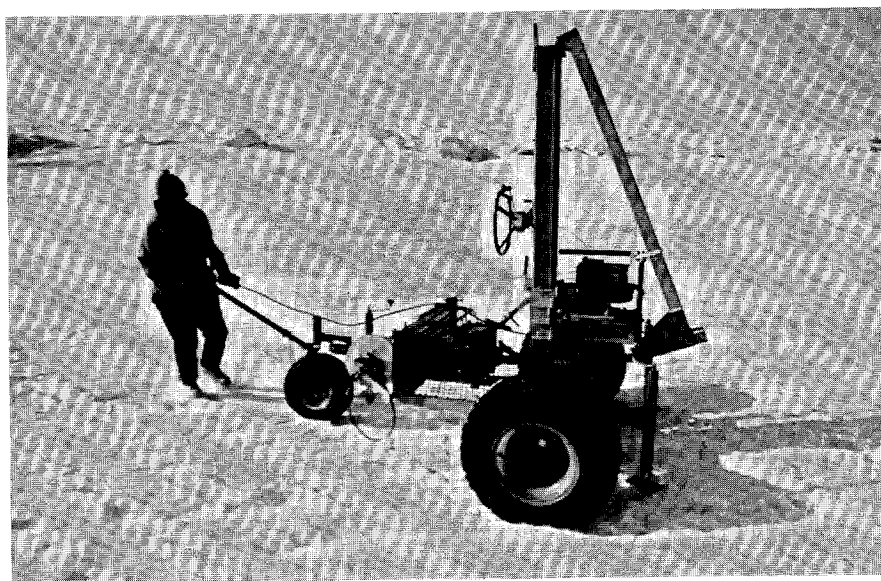
Figure 14. Mobile drilling rig used to support and drive the 30.5-cm (12-in.) diameter core barrel.
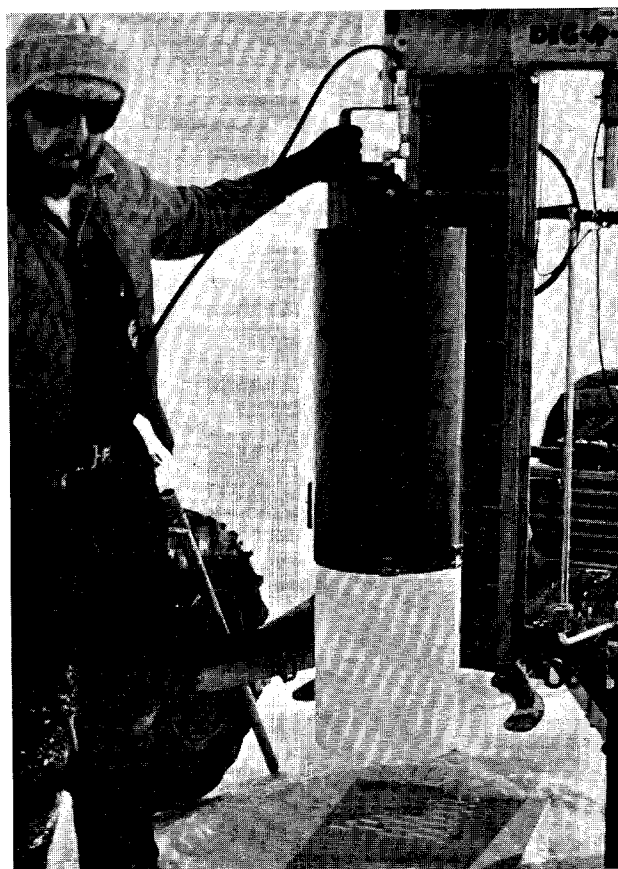
Figure 15. Core catcher used to break and retrieve 30.5-cm (12-in.) diameter core.

12
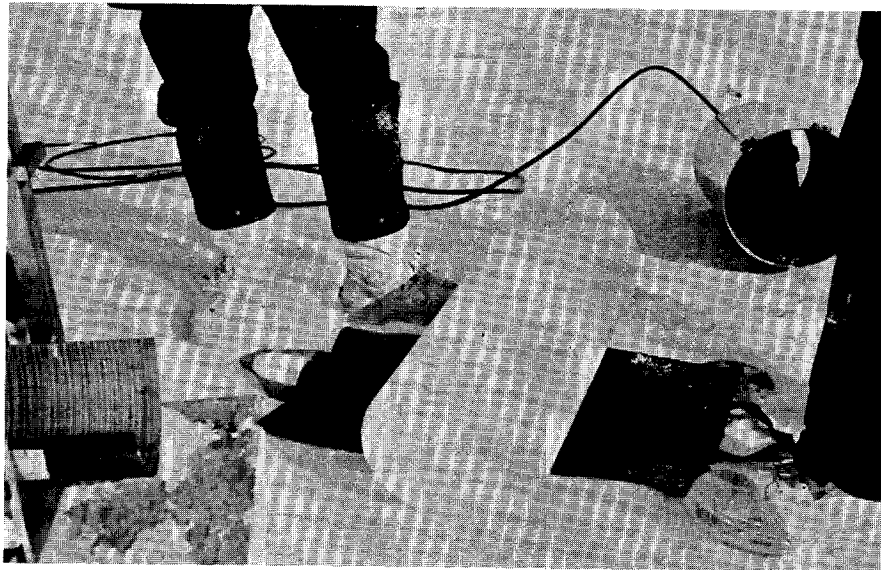
Figure 16. Log carrier used to handle large diameter core.

Figure 17. Drill press used to obtain horizontal samples from the 30.5-cm (12-in.) diameter core.

13

Boston. In Anchorage, Emery transferred the cargo to Flying Tigers. CRREL personnel finally met each of the Flying Tigers flights in Boston with a refrigerated truck and transported the ice to Hanover.

Originally, we had planned to store the ice in Anchorage, and then arrange for one shipment to Hanover, as we had done in Phase I. However, because of the delay of going into the field, we were not able to arrange for refrigerated storage in Anchorage. The majority of the refrigerated space is owned by fishing companies, and the fishing season had already started. This problem actually did us a favor as it forced us to ship directly to Boston, a procedure that was easier, and successful. We plan to ship all ice samples directly from Deadhorse to Boston in the future.

ICE DESCRIPTION

Before presenting the results from the different mechanical property tests of in Phase II, it is appropriate to examine the ice samples. This will facilitate our interpretation of the test results and make any comparisons to the Phase I data more meaningful.

In general, the ice samples collected during Phase II were different from the samples obtained during Phase I. The Phase II samples had a slightly lower density and contained more columnar ice. The average salinities of the samples collected during Phases I and II were similar.

Salinity and density

Ice samples from ridges A, B, and C were used in the Phase II test program. Average salinities and densities of the ice samples from these ridges are given in Table 4. The data are grouped according to whether the samples were obtained from the ridge sails (above level ice) or the ridge keels (below level ice). Average salinities and densities for each ridge and averages for all the samples are also given. Phase I data are included for comparisons.

Samples from ridge A had a much lower average salinity and density than the test samples from ridges B and C. This was particularly true for the samples collected from the pressure ridge sails.

Structure

While the structure of all the test samples will not be analyzed in detail until a later date, it was clearly evident that the ice samples collected during Phase II contained significantly more columnar ice than the samples obtained during Phase I.

Table 4. Average salinity and density (−20°C) of ice samples obtained from ridges A, B and C during Phase II and all ridges from Phase I.

	Salinity (‰)	Density (Mg m⁻³)
Above sea level		
Ridge A	0.08 ± 0.14	0.807 ± 0.032
Ridge B	0.86 ± 0.56	0.850 ± 0.038
Ridge C	1.68 ± 1.06	0.879 ± 0.030
Three ridges	0.77 ± 0.91	0.841 ± 0.045
Phase I	0.71 ± 0.57	0.875 ± 0.032
Below level ice		
Ridge A	0.89 ± 0.46	0.877 ± 0.024
Ridge B	1.66 ± 0.91	0.888 ± 0.018
Ridge C	2.68 ± 1.11	0.894 ± 0.018
Three ridges	1.89 ± 1.16	0.888 ± 0.020
Phase I	1.56 ± 0.77	0.899 ± 0.018
Above and below level ice		
Ridge A	0.38 ± 0.49	0.834 ± 0.046
Ridge B	1.29 ± 0.87	0.870 ± 0.035
Ridge C	2.29 ± 1.19	0.888 ± 0.024
Three ridges	1.34 ± 1.18	0.865 ± 0.042
Phase I	1.26 ± 0.82	0.891 ± 0.026

It is conceivable that in Phase I we mostly sampled highly granulated shear ridges, whereas in Phase II, we sampled compression ridges that contained large blocks of columnar sea ice.

Of the three ridges tested in Phase II, we have, at this time, systematically examined the structure of ice samples from ridge C only. A continuous core was specifically obtained from ridge C for petrographic work. In addition, horizontal and vertical sample pairs were obtained from ridge C for uniaxial compression tests. The structure of these samples was subsequently analyzed to explain the variation of ice strength between the sample pairs.

A detailed structural profile of the continuous core obtained from ridge C is presented in Appendix A. The profile was prepared by splicing together photographs of vertical ice thin sections, which were taken between crossed polaroids. A few photographs of horizontal thin sections are also presented. The salinity profile and a schematic structural profile of the core are given in Figure 18. It should be noted that the core was obtained through the full thickness of the ridge, 9.53 m.

The upper 40 cm of the core consists primarily of very porous, coarse columnar grains. Some

fine-grained granular material is mixed throughout this section. From 40 to 85 cm, the ice structure is mixed, made up of large pieces of columnar ice separated by fine granular crystals. At 85 cm, the core becomes 100% columnar with the direction of elongation of the crystals oriented vertically. The columnar crystals are medium grained and unaligned at 85 cm. At 100 cm, the c-axes become aligned and the grain size of the crystals increases with depth to about 180 cm where a 3-cm-thick band of fragmented ice is encountered. Below this band, the direction of elongation of the coarse columnar crystals changes to 10° from the vertical. Conceivably, this is another block of sea ice that was incorporated into the ridge. This block of columnar ice contains well defined, fine-grained bands.

From 245 to 330 cm the ice is fragmented, consisting of large pieces of columnar ice in a fine-grained granular ice matrix. The columnar fragments are up to 10 cm in diameter. At 330 cm, the ice structure alternates between 50-cm-thick bands of fine- to coarse-grained columnar ice and 20- to 50-cm-thick bands of fine granular, mixed granular and columnar material. This sequence continues to about 650 cm.

At 650 cm, a 2-m-thick layer of fragmented ice is found, containing both large and small columnar fragments. The remainder of the core is mostly columnar, with some fine-grained granular material mixed throughout the section.

About 50% of this multi-year pressure ridge core consists of columnar ice. The rest of the core is a combination of granular ice and mixed granular and columnar crystals. The mixed ice is predominantly fragmented. Only about one-third of the multi-year ridge core petrographically studied in Phase I contained well-defined columnar zones. In general, more columnar ice was encountered in the Phase II ice sampling program. As in Phase I, samples containing a variety of ice types were obtained and large, structure-dependent variations in the ice mechanical properties were anticipated.

CONSTANT-STRAIN-RATE COMPRESSION TESTS

Test variables

We did 62 constant-strain-rate, uniaxial compression tests in Phase II. The tests were conducted at two strain rates, 10^{-4} s^{-1} and 10^{-2} s^{-1}, and two temperatures, $-20°C$ ($-4°F$) and $-5°C$ ($23°F$), to supplement the tests done in Phase I. In Phase I the compression tests were conducted at strain rates of 10^{-5} s^{-1} and 10^{-3} s^{-1} and at temperatures of $-20°$ and $-5°C$. Unlike Phase I, in Phase II both horizontal and vertical samples were tested to assess the effect of sample orientation on ice strength. The number of tests at each test condition is summarized in Table 5. Details on the sam-
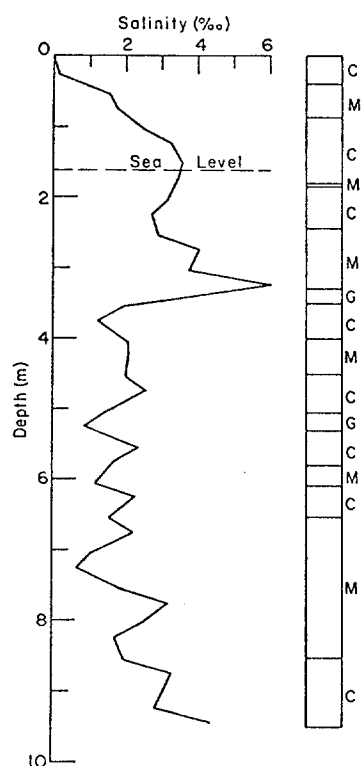
Figure 18. Salinity profile and schematic structural profile of continuous core from ridge C. C–columnar ice, G–granular ice, and M–mixed ice, C and G.

Table 5. Number of uniaxial compression tests at different temperatures and strain rates.

Temp	$\dot{\epsilon}$		
	10^{-4} s^{-1}	10^{-2} s^{-1}	Total
–5°C (23°F)	9V*	9V	18V
	10H	—	10H
–20°C (–4°F)	13V	9V	22V
	12H	—	12H
Total	22V	18V	40V
	22H	—	22H

* V—vertical; H—horizontal.

15

ple preparation and testing techniques are given by Mellor et al. (1984). The procedures used in Phase II were identical to those used in Phase I.

Uniaxial compressive strength

A detailed tabulation of the results from the constant-strain-rate, uniaxial compression tests is given in Appendix B. The average compressive strength of the ice is plotted against strain rate in Figure 19. The test results from Phase I at 10^{-5} and 10^{-3} s^{-1} are also included for comparison. Average strength values from Phases I and II are listed in Table 6.

At a given temperature and strain rate, the Phase II strength data show considerable scatter. These large variations in strength can be explained by large variations in the ice structure and porosity (Richter and Cox 1984). The strength of each spec-

imen not only depends on the type of ice present in it, which is highly variable from sample to sample, but also on the ice grain size and crystal orientation. Strength variations are further increased by variations in the ice porosity.

Based on our understanding of the variation of ice strength with strain rate, we would expect a power law relationship between ice strength and strain rate in the ductile range (Mellor 1983). On log-log paper, strength versus strain rate would plot as a straight line. The combined average test results of Phases I and II at -5°C do not show this tendency. The average strength of the 10^{-4} s^{-1} tests is lower than anticipated. However, at -20°C the 10^{-4} s^{-1} Phase II test average is in reasonable agreement with the 10^{-5} and 10^{-3} s^{-1} averages obtained in Phase I.
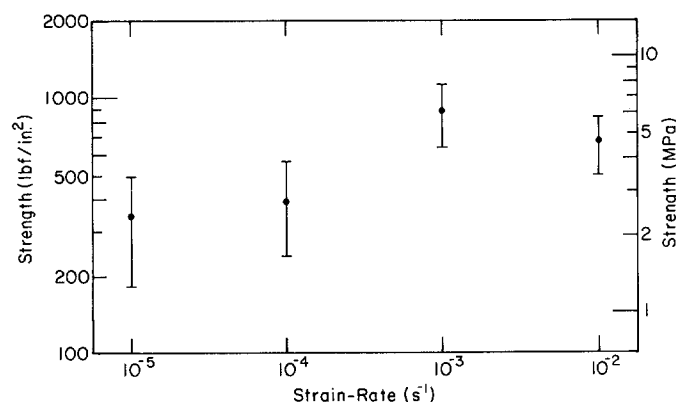
a. Samples tested at -5°C (23°F).
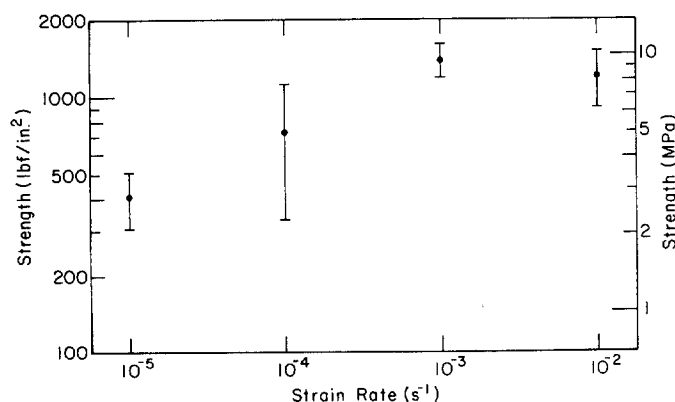
b. Samples tested at -20°C (-4°F).

Figure 19. Uniaxial compressive strength vs strain rate. The bars denote one standard deviation.

16

Table 6. Summary of uniaxial compressive strength data for Phases I and II.

	Maximum (MPa)	Maximum (lbf in.$^{-2}$)	Minimum (MPa)	Minimum (lbf in.$^{-2}$)	Mean (MPa)	Mean (lbf in.$^{-2}$)	Mean porosity (°/oo)	No. of samples
				-5°C (23°F)				
10^{-5} s^{-1} V*	7.52	1090	0.47	68	2.34 ± 1.08	340 ± 157	44	71
10^{-4} s^{-1} V	5.52	800	1.87	271	3.07 ± 1.23	445 ± 179	69	9
10^{-4} s^{-1} H	3.87	561	1.21	175	2.35 ± 0.74	341 ± 108	78	10
10^{-4} s^{-1} all	5.52	800	1.21	175	2.69 ± 1.04	390 ± 151	73	19
10^{-3} s^{-1} V	10.90	1580	2.39	346	6.06 ± 1.63	879 ± 237	46	69
10^{-2} s^{-1} V	6.42	931	2.69	390	4.67 ± 1.17	677 ± 169	68	9
				-20°C (-4°F)				
10^{-5} s^{-1} V	4.26	617	1.17	170	2.79 ± 0.69	404 ± 100	36	41
10^{-4} s^{-1} V	12.73	1846	3.34	485	6.17 ± 3.10	894 ± 450	50	13
10^{-4} s^{-1} H	7.02	1018	1.68	243	3.74 ± 1.67	543 ± 242	33	12
10^{-4} s^{-1} all	12.73	1846	1.68	243	5.00 ± 2.70	725 ± 392	42	25
10^{-3} s^{-1} V	12.68	1838	7.03	1020	9.63 ± 1.39	1396 ± 202	39	41
10^{-2} s^{-1} V	10.48	1520	4.12	597	8.24 ± 2.05	1195 ± 297	74	9

* H—horizontal; V—vertical.

Since the strength of sea ice decreases with increasing porosity, it appears that the above observations can be explained in terms of the average ice porosity of the samples tested at each strain rate and temperature. In Table 6 mean porosities are given for the samples tested at each test condition. At -5°C, the 10^{-4} s^{-1} tests have a much higher porosity than the tests conducted at 10^{-5} and 10^{-3} s^{-1}. At -20°C, the mean porosities of the 10^{-5}, 10^{-4}, and 10^{-3} s^{-1} tests are similar and the average strength values do show a power law relationship.

In both of the -5° and -20°C tests conducted at a strain rate of 10^{-2} s^{-1}, there is an apparent decrease in ice strength relative to the tests conducted at 10^{-3} s^{-1}. We attribute this decrease in strength to the much larger porosity of the 10^{-2} s^{-1} samples.

Strength and structure

In Phase II, the effect of structure on the compressive strength of multi-year ridge ice samples was further investigated in an effort to explain the difference in ice strength between horizontal and vertical samples. The horizontal and vertical samples were obtained near to one another and grouped in pairs according to sampling depth. Each pair was tested at the same strain rate and temperature. We examined a total of 44 tests conducted at a strain rate of 10^{-4} s^{-1}. Of these 44 tests, 19 tests were performed at -5°C and 25 tests at -20°C. The structural analysis was similar to that described in Phase I. Thin sections were prepared

of both the tested sample and the end pieces adjacent to the test specimen. We determined ice type, grain size and crystal orientation by studying photographs of the thin sections taken between crossed polaroids. Additional photographs of the test specimen taken before and after the test were used to document the failure characteristics of the ice.

The strength, structure and porosity of these samples are given in Table 7. The σ:z angle for the columnar samples is defined as the angle between the load and the direction of elongation of the columnar crystals. The σ:c angle is defined as the angle between the load and the preferred c-axis alignment direction of the crystals. The angle measurements provided were made on a universal stage. Thin section photographs taken of each sample were used to confirm these crystallographic measurements and to define the average grain size. The ice type classification is in accordance with the structural classification scheme established in Phase I (Table 8). Porosity values were calculated using the relationship given by Cox and Weeks (1983), which related sample salinity, density and temperature to sample porosity.

The results of the Phase II structural analysis were similar to the results of Phase I. However, the different nature of the Phase II ice and the horizontal and vertical pairs provided an opportunity to observe additional trends in the structure-to-strength relationship. In general, the Phase II ice was more porous and consisted of more well

Table 7. Strength, structure and porosity of horizontal and vertical sample pairs.

Sample no.	Strength (MPa)	Strength (lbf in.$^{-2}$)	Ice type	Average grain size (mm)	Porosity ($^0/_{00}$)
			a. Tested at 10^{-4} s^{-1} and $-20°C$ ($-4°F$)		
RC32-231/258V*	6.64	963	IIA aligned, Columnar $\sigma{:}z = 15°$, $\sigma{:}c = 76°$	30×15	46.2
RC43-245H	3.77	546	IIA aligned, $\sigma{:}z = 86°$, $\sigma{:}c = 12°$	30×7	29.9
RC32-267/294V	4.56	661	IIA aligned, $\sigma{:}z = 15°$, $\sigma{:}c = 80°$	42×20	42.1
RC33-268/295V	6.20	899	IIA aligned, $\sigma{:}z = 15°$, $\sigma{:}c = 78°$	25×12	24.0
RC43-280H	4.88	708	IIA aligned, $\sigma{:}z = 90°$, $\sigma{:}c = 5°$	30×10	38.5
RC32-303/328V	3.95	573	IIIB 60% granular 40% columnar	Granular <1	64.1
RC43-316H	2.36	342	IIA aligned, $\sigma{:}z = 85°$, $\sigma{:}c = 25°$	60×20	29.8
RC32-343/396V	3.34	485	III		88.5
RC43-357H	4.12	597	IIIB 60% granular, 40% columnar	<1	58.7
RC33-242/268V	6.53	947	IIA aligned, $\sigma{:}z = 10°$, $\sigma{:}c = 82°$	45×15	30.1
RC43-257H	3.73	541	IIA aligned, $\sigma{:}z = 85°$, $\sigma{:}c = 0°$	30×15	24.4
RC33-368/395V	6.47	939	III		40.6
RC43-381H	5.98	867	III		31.0
RC46-121/147V	3.57	517	IIIB 50% granular	<1	72.1
RC44-128H	1.76	225	IIA aligned, $\sigma{:}z = 65°$, $\sigma{:}c = 24°$	48×22	28.4
RC46-173/199V	3.40	493	IIIB 60% granular	<1	70.4
RC44-186H	7.02	1018	IIA aligned, $\sigma{:}z = 0°$, $\sigma{:}c = 90°$	50×18	31.6
RC46-276/303V	4.34	629	IIIB 60% granular	<1	68.7
RC44-299H	4.20	609	IIIB 70% granular	<1	48.9
RC47-090/116V	12.40	1798	IIA aligned, $\sigma{:}z = 0°$, $\sigma{:}c = 90°$	35×10	41.0
RC44-103H	3.48	505	IIA aligned, $\sigma{:}z = 90°$, $\sigma{:}c = 20°$	40×12	34.8
RC44-116H	1.68	243	IIA aligned, $\sigma{:}z = 90°$, $\sigma{:}c = 25°$	40×12	25.3
RC47-127/153V	12.73	1846	IIA aligned, $\sigma{:}z = 3°$, $\sigma{:}c = 87°$	45×10	36.0
RC44-141H	1.98	287	IIA aligned, $\sigma{:}z = 90°$, $\sigma{:}c = 35°$	45×12	16.6
RC47-302/329V	6.03	875	III: top III, middle-bottom IIA aligned, $\sigma{:}z = 10°$, $\sigma{:}c = 80°$	65×20	23.5

* V—vertical; H—horizontal (see Appendix B for explanation of sample number scheme).

18

Table 7 (cont'd).

Sample no.	Strength (MPa)	Strength (lbf in.$^{-2}$)	Ice type	Average grain size (mm)	Porosity ($^o/_{oo}$)
b. Tested at 10^{-4} s^{-1} and −5°C (23°F)					
RC32-133/160V	2.28	330	IIIB 50% granular, 50% columnar	Granular < 1	78.8
RC43-150H	2.66	386	IIIB 80% granular	≤ 1	104.0
RC33-205/232V	3.30	478	IIIB: Top II aligned, σ:z = 0°, σ:c = 90° middle I bottom IIA, σ:z = 20°	Columnar 50×10 ≤ 1 20×6	70.6
RC43-222H	2.77	402	III 70% granular, 30% columnar	≤ 1	60.4
RC46-047/073V	2.50	362	IIIB: top-middle IIIB, 70% granular, bottom IIA aligned, σ:z = 8°, σ:c = 82°	30×10	63.3 63.3
RC44-073H	2.25	326	IIIA 20% granular 80% IIA aligned σ:z = 86°, σ:c = 82°	≤ 1 25×10	86.2
RC44-060H	1.57	227	III 60% IIA aligned, σ:z = 90°, σ:c = 64°, 40%IIIB	28×7	127.7
RC46-083/110V	5.52	800	IIIA 90% IIA aligned, σ:z = 4°, σ:c = 86°, 10% granular	35×12 Granular < 1	66.7
RC44-086H	2.69	390	IIA aligned, σ:z = 85°, σ:c = 90°	30×10	25.8
RC46-147/173V	1.87	271	IIB 85% IIA aligned, σ:z = 15°, σ:c = 80°	30×8	69.7
RC44-156H	1.21	175	IIIA 90% IIA aligned, σ:z = 78°, σ:c = 30°	45×12	54.0
RC46-246/272V	3.08	446	IIIA 90% IIA aligned, σ:z = 8°, σ:c = 82°	30×10	76.5
RC44-256H	1.87	271	IIIB 30% granular	< 1	56.4
RC47-025/053V	2.22	322	IIIB: Top IIA aligned, σ:z = 0°, σ:c = 90° middle I bottom II aligned, σ:z = 0°, σ:c = 90°	50×15 < 1 25×8	81.8
RC45-040H	2.11	306	IIIA vertical crack, 90% IIA aligned, σ:z = 80°, σ:c = 45°	22×10	42.2
RC47-191/217V	4.61	669	IIIA 90% IIA aligned, σ:z = 5°, σ:c = 83°	35×10	50.2

19

Table 7 (cont'd). Strength, structure and porosity of horizontal and vertical sample pairs.

Sample no.	Strength (MPa)	(lbf in.$^{-2}$)	Ice type	Average grain size (mm)	Porosity (°/oo)
RC44-204H	3.87	561	IIIA 90% IIA aligned $\sigma{:}z$ = 85°; $\sigma{:}c$ = 10°		46.7
RC47-275/302V	2.25	326	IIA, $\sigma{:}z$ = 20°	Top-middle 20 × 15 Bottom 18 × 8	59.9
RC44-288H	2.52	366	IIIB, 50% granular	< 1	73.5

* V—vertical; H—horizontal (see Appendix B for explanation of sample number scheme).

Table 8. Structural classification scheme for multi-year pressure ridge ice samples.

Ice type	Code	Structural characteristics
Granular	I	Isotropic, equiaxed crystals
Columnar	II	Elongated, columnar grains
	IIA	Columnar sea ice with c-axes normal to growth direction; axes may not be aligned
	IIB	Columnar sea ice having random c-axis orientation (Transition ice)
	IIC	Columnar freshwater ice; may be either anisotropic or isotropic
Mixed	III	Combination of Types I and II
	IIIA	Largely Type II with granular veins
	IIIB	Largely Type I with inclusions of Type I or II ice (Brecciated ice).

defined columnar blocks than the Phase I ice. Furthermore, the 10^{-4} s^{-1} samples, although randomly selected, were dominated by one ice type at each test temperature. The majority of the samples tested at 10^{-4} s^{-1} and $-5°C$ consisted of mixed or brecciated (fragmented) ice (Type III). The specimens at $-20°C$ were mostly columnar (Type IIA).

Our observations on the structural variation of ice strength for columnar samples tested at $-20°C$ are in agreement with the findings of Peyton (1966) and Wang (1979). Columnar samples loaded parallel to the direction of crystal elongation and normal to the c-axes ($\sigma{:}z$ = 0°; $\sigma{:}c$ = 90°) were extremely strong. Specimens loaded perpendicular to the direction of crystal elongation ($\sigma{:}z$ = 90°) and parallel or normal to the direction of preferred c-axis alignment ($\sigma{:}c$ = 0 or 90°) had a significantly lower strength value. As the angle between the c-axis and the applied load approached

45° in these columnar samples, the strength decreased further. The compressive strength of the mixed and granular ice samples tested at these conditions was comparable to the strength of columnar samples loaded with $\sigma{:}z$ = 90° and $\sigma{:}c$ = 0° or $\sigma{:}c$ = 90°. The mixed and granular specimens also tended to decrease in strength as the ice porosity increased.

Many of the mixed ice samples tested at $-5°C$ contained large, columnar ice fragments. It became apparent that the orientation of columnar fragments within the sample had an influence on the strength value. If the columnar ice in the sample was oriented with the direction of crystal elongation parallel to the load ($\sigma{:}z$ = 0°), the sample failed at a relatively high load (comparable to the strength of a $\sigma{:}z$ = 90°, $\sigma{:}c$ = 0° loading in a columnar sample). As the angle between the direction of crystal elongation approached 45°, the strength of the mixed brecciated ice decreased.

The difference in strength between horizontal and vertical pairs was also found to depend on the ice structure. In general, the vertical samples had a higher strength value. At $-5°C$ the average strength of the vertical samples was 30% higher. At $-20°C$ the average strength of the vertical and horizontal samples differed by 65%. The most significant differences in strength occurred in sample pairs of columnar ice.

Our petrographic observations show that many of the columnar ice blocks in a multi-year ridge lie horizontally or near horizontally. In this position, large ice blocks in a ridge are the most stable. Consequently, a significant number of the vertically cored columnar ridge samples are loaded parallel to the direction of crystal elongation and have a high strength. Horizontal columnar samples tend to have an angle of 90° between the long columns and the applied load and a much lower strength.

20

Peyton (1966) has also shown that strength values can differ between these two loading orientations by as much as a factor of three. Should additional field studies of block orientation in first-year and multi-year pressure ridges show a preference for horizontal block orientation, it may be justifiable to use lower ice force values for in-plane ridge loading on structures. Use of strength data from vertically oriented specimens would be conservative.

In general, sample pairs of mixed and granular ice had comparable strength values. Some vertical samples tended to have slightly higher strength. This may reflect the influence of internal columnar fragment orientations as discussed earlier.

Strength and porosity

The compressive strength of the samples is plotted against the total porosity of the ice in Figure 20. The air and brine volume equations given by Cox and Weeks (1983) were used to calculate the ice porosity from the ice salinity, temperature and density. As in Phase I, there is a tendency for the ice strength to decrease with increasing porosity. This trend is again most pronounced at high strain rates, 10^{-2} s^{-1}, where flaws and cavities play a more important role in brittle ice behavior.

Residual compressive strength

The uniaxial compression tests on the testing machine were programmed to continue to 5% full-sample axial strain to examine the residual strength and post-yield behavior of the ice. The residual strength is defined as the stress on the sample at 5% strain, assuming a constant 10.16-cm (4.000-in.) diameter specimen. Average values of the residual-strength-to-maximum-strength ratio of the ice samples under different loading conditions are given in Table 9. Data from Phase I are included for comparison. The results show that the residual-strength-to-maximum-strength ratio decreases with increasing strain rate and is relatively insensitive to the ice temperature and porosity. As the strain rate increases, fewer samples go to 5% strain and at 10^{-2} s^{-1} all the tests terminated at the peak or maximum stress.
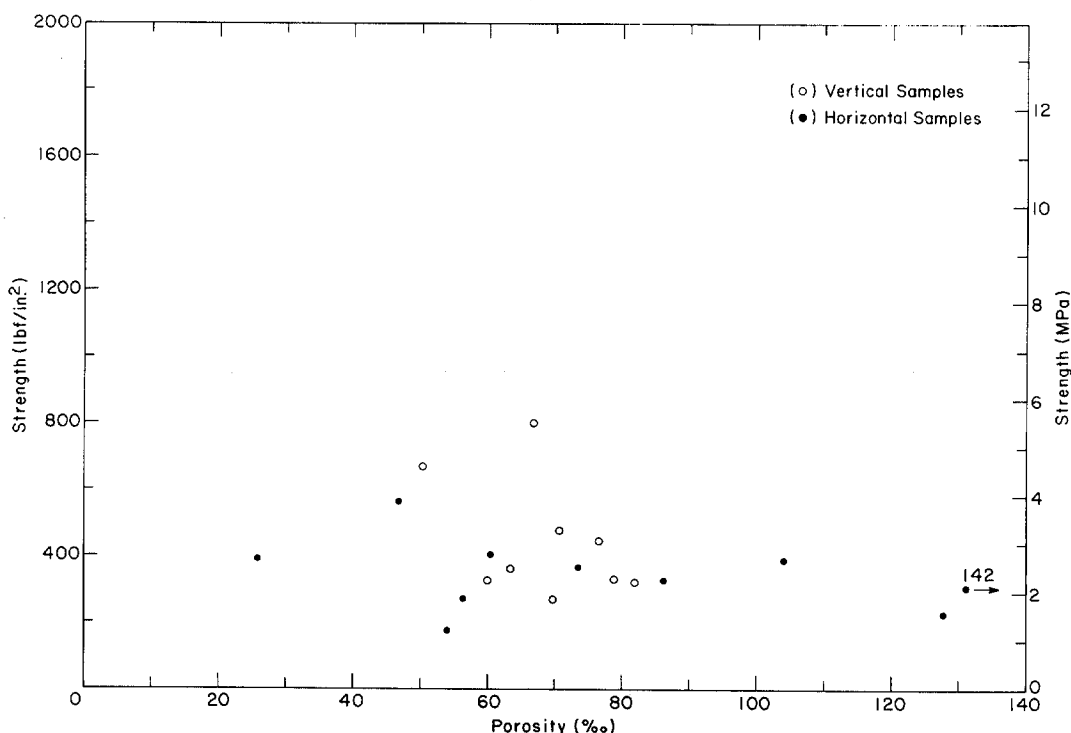
a. Horizontal and vertical samples tested at $-5\,°C$ ($23\,°F$) and 10^{-4} s^{-1}.

Figure 20. Uniaxial compressive strength versus porosity.

21
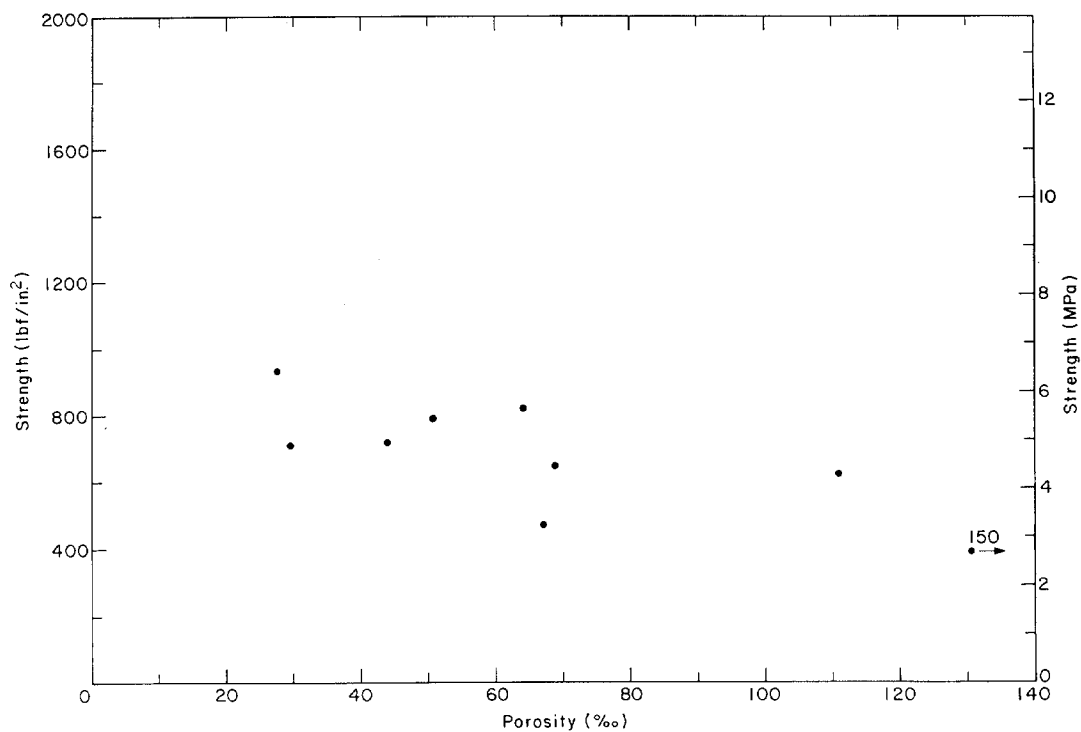
b. *Tests conducted at –5 °C (23 °F) and 10^{-2} s^{-1}.*
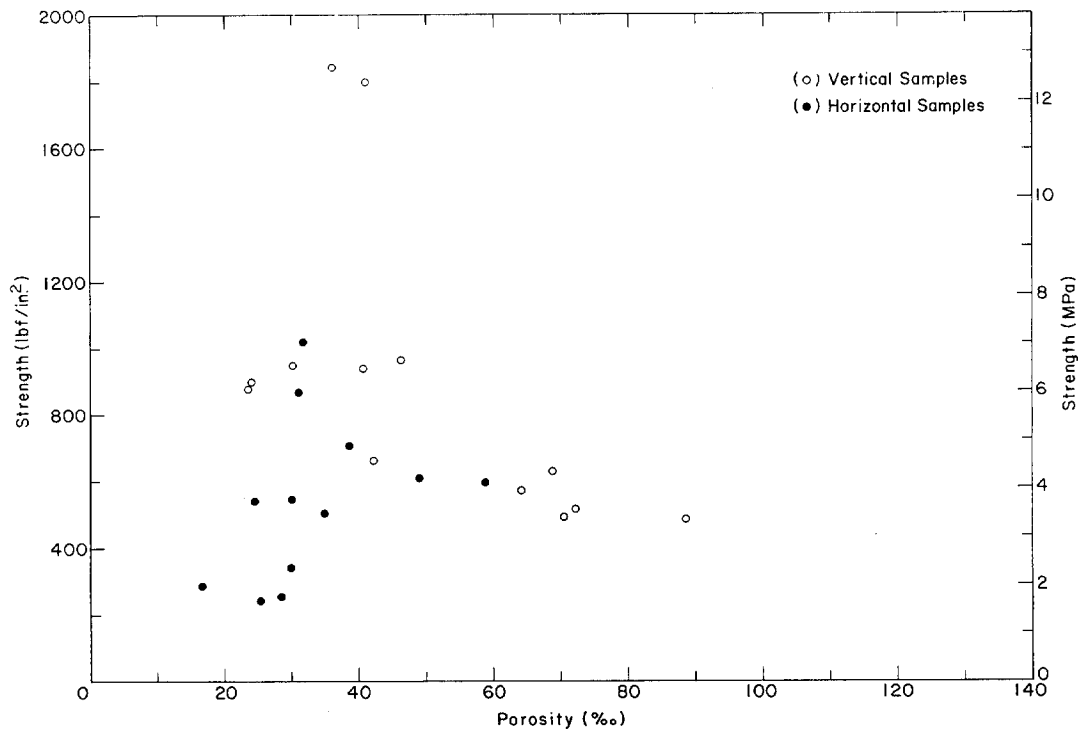
c. *Horizontal and vertical samples tested at –20 °C (–4 °F) and 10^{-4} s^{-1}.*

Figure 20 (cont'd). Uniaxial compressive strength versus porosity.

22
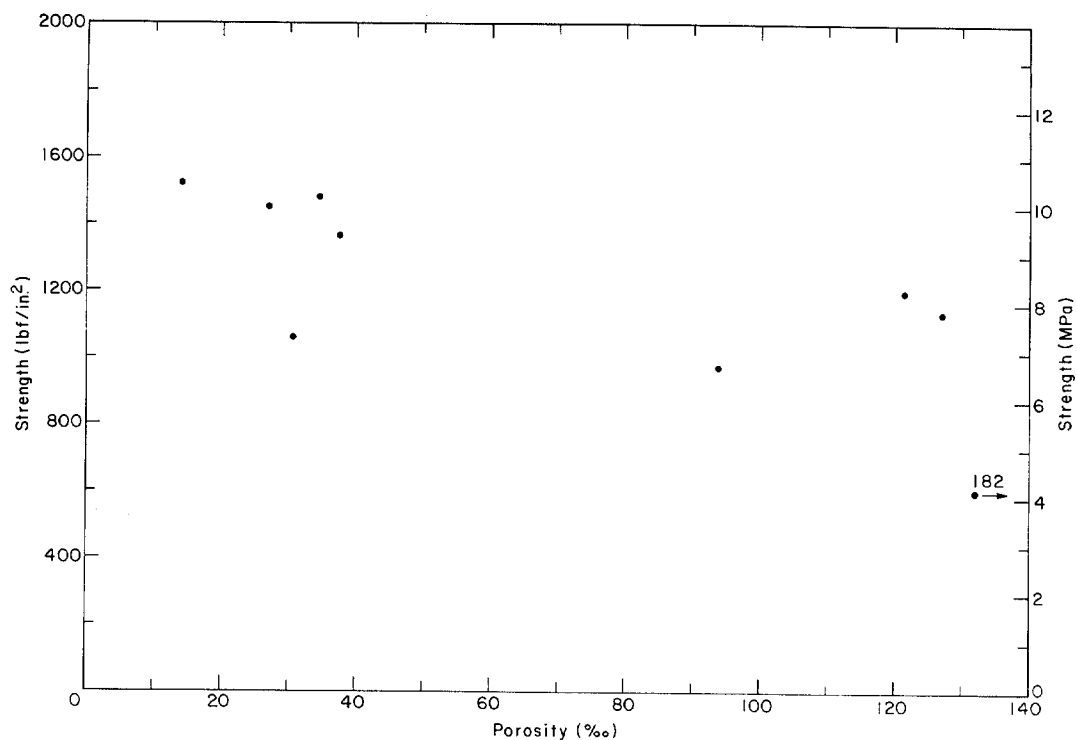
d. Tests conducted at -20°C (-4°F) and 10^{-2} s^{-1}.

Figure 20 (cont'd).

Table 9. Summary of residual-to-maximum-compressive-strength ratio data for Phases I and II.

	Maximum	Minimum	Mean	No. of samples	Percent to 5% strain
-5°C (23°F)					
10^{-5} s^{-1} V*	1.000	0.173	0.688 ± 0.166	68	96
10^{-4} s^{-1} V	0.591	0.244	0.396 ± 0.096	9	100
10^{-4} s^{-1} H	0.794	0.245	0.439 ± 0.159	10	100
10^{-4} s^{-1} all	0.794	0.244	0.418 ± 0.131	19	100
10^{-3} s^{-1} V	0.421	0.074	0.198 ± 0.078	43	62
10^{-2} s^{-1} V	—	—	—	—	0
-20°C (-4°C)					
10^{-5} s^{-1} V	0.970	0.315	0.642 ± 0.162	36	88
10^{-4} s^{-1} V	0.504	0.253	0.342 ± 0.077	9	69
10^{-4} s^{-1} H	0.675	0.202	0.405 ± 0.137	12	100
10^{-4} s^{-1} all	0.675	0.202	0.378 ± 0.114	21	84
10^{-3} s^{-1} V	0.746	0.047	0.194 ± 0.148	18	44
10^{-2} s^{-1} V	—	—	—	—	0

* H—horizontal; V—vertical.

23

Failure strain

Average sample failure strains at the peak or maximum stress for the different test conditions in Phases I and II are given in Table 10. The strains were calculated from the average of the DCDT measurements on the sample. In general, there is a strong tendency for the sample failure strain to decrease with increasing strain rate. At low strain rates of 10^{-5} and 10^{-4} s^{-1}, the failure strain also decreases as the ice gets colder. However, at high strain rates of 10^{-3} and 10^{-2} s^{-1}, the failure strain increases as the ice gets colder. Examination of the standard deviation of the mean strains indicates that the observed temperature trends are not statistically significant.

Strength versus strain-to-failure plots are given in Figure 21. At $-5\,°C$ there is a positive correlation between the strength and failure strain for the 10^{-2} s^{-1} tests, whereas at 10^{-4} s^{-1}, there is no apparent correlation. At $-20\,°C$, both the 10^{-4} and 10^{-2} s^{-1} tests show a positive correlation between the strength and failure strain.

Table 10. Summary of failure strain (%) for compression tests in Phases I and II.

	Maximum	Minimum	Mean	No. of samples
−5°C (23°F)				
10^{-5} s^{-1} V	0.83	0.06	0.38 ± 0.17	71
10^{-4} s^{-1} V	0.62	0.09	0.18 ± 0.17	9
10^{-4} s^{-1} H	0.26	0.06	0.12 ± 0.07	10
10^{-4} s^{-1} all	0.62	0.06	0.14 ± 0.12	19
10^{-3} s^{-1} V	0.20	0.05	0.13 ± 0.03	69
10^{-2} s^{-1} V	0.10	0.02	0.07 ± 0.02	9
−20°C (−4°C)				
10^{-5} s^{-1} V	0.73	0.10	0.31 ± 0.14	41
10^{-4} s^{-1} V	0.21	0.10	0.15 ± 0.04	13
10^{-4} s^{-1} H	0.14	0.07	0.10 ± 0.03	12
10^{-4} s^{-1} all	0.21	0.07	0.13 ± 0.04	25
10^{-3} s^{-1} V	0.25	0.05	0.19 ± 0.04	41
10^{-2} s^{-1} V	0.16	0.08	0.12 ± 0.03	9

* H—horizontal; V—vertical.
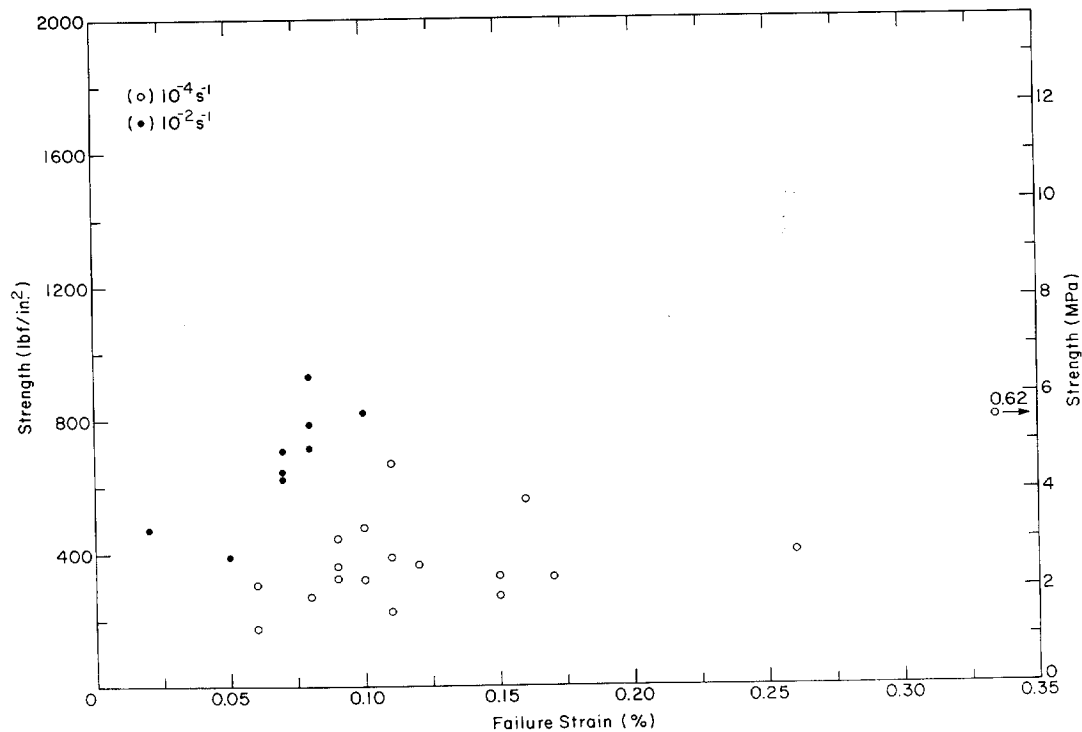
a. Tests conducted at −5 °C (23 °F).

Figure 21. Uniaxial compressive strength vs failure strain.

24
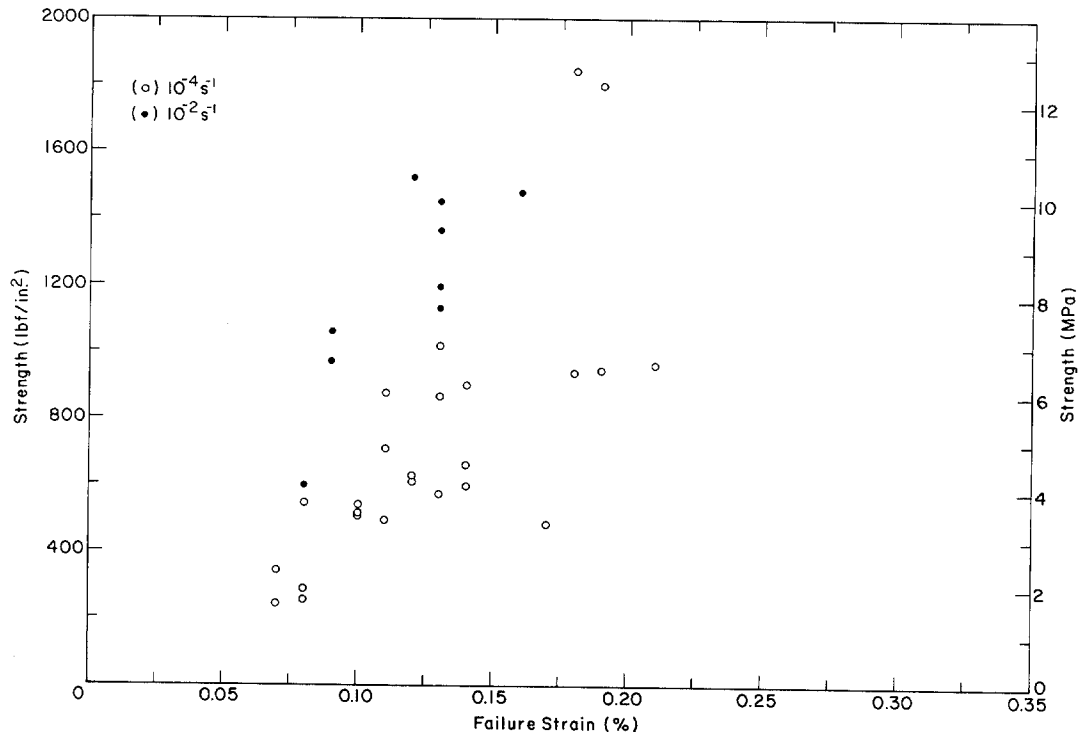
b. Tests conducted at -20°C (-4°F).

Fig. 21 (cont'd).
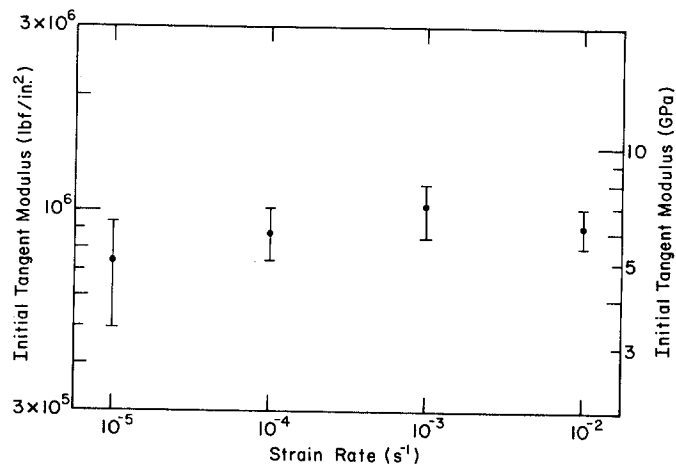
a. Tests conducted at -5°C (23°F).

Figure 22. Initial tangent modulus vs strain rate for compression tests. The bars denote one standard deviation.

25
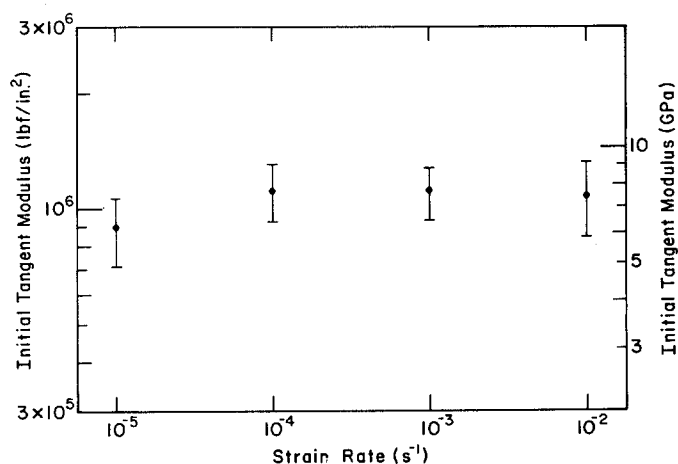
b. Tests conducted at -20°C (-4°F).

Figure 22 (cont'd). Initial tangent modulus vs strain rate for compression tests. The bars denote one standard deviation.

Initial tangent modulus

We obtained estimates of the initial tangent modulus from the initial slope of the force–displacement curves using the same procedures as in Phase I. The results are plotted against strain rate in Figure 22 and listed in Table 11. Modulus values from Phase I are included in both the figure and table for comparison. The initial tangent modulus is plotted against the ice porosity for ice temperatures of -5°C and -20°C in Figure 23.

It is interesting to note that the initial tangent modulus approaches the "dynamic" Young's modulus of the ice at a lower strain rate in the colder, -20°C tests. Furthermore, at a given strain rate and temperature there is a tendency for the modulus to decrease with increasing porosity.

Table 11. Summary of initial tangent modulus data for compression tests in Phases I and II.

	Maximum		Minimum		Mean		Mean porosity (⁰/₀₀)	No. of samples
	(GPa)	(lbf in.⁻²)	(GPa)	(lbf in.⁻²)	(GPa)	(lbf in.⁻²)		
			-5°C (23°F)					
10^{-5} s⁻¹ V*	10.34	1.500×10^6	2.41	0.350×10^6	5.02 ± 1.57	$0.728 \pm 0.228 \times 10^6$	44	70
10^{-4} s⁻¹ V	7.89	1.144	5.32	0.771	6.30 ± 0.96	0.914 ± 0.139	69	9
10^{-4} s⁻¹ H	7.41	1.074	4.41	0.639	5.81 ± 0.94	0.842 ± 0.136	78	10
10^{-3} s⁻¹ all	7.89	1.144	4.41	0.639	6.04 ± 0.95	0.876 ± 0.138	73	19
10^{-2} s⁻¹ V	9.86	1.430	4.95	0.718	6.99 ± 1.12	1.104 ± 0.162	46	70
10^{-2} s⁻¹ V	6.90	1.000	4.89	0.709	6.21 ± 0.73	0.901 ± 0.106	68	9
			-20°C (-4°C)					
10^{-5} s⁻¹ V	10.48	1.520	3.45	0.500	5.95 ± 1.19	0.863 ± 0.172	36	40
10^{-4} s⁻¹ V	9.70	1.406	5.35	0.776	7.74 ± 1.42	1.122 ± 0.206	50	13
10^{-4} s⁻¹ H	10.28	1.490	6.18	0.896	7.58 ± 1.26	1.099 ± 0.182	33	12
10^{-4} s⁻¹ all	10.28	1.490	5.35	0.776	7.66 ± 1.29	1.111 ± 0.187	42	25
10^{-3} s⁻¹ V	10.38	1.570	4.89	0.709	7.62 ± 1.19	1.105 ± 0.173	39	40
10^{-2} s⁻¹ V	10.50	1.522	5.28	0.765	7.50 ± 1.61	1.088 ± 0.223	74	9

* H—horizontal; V—vertical.

26
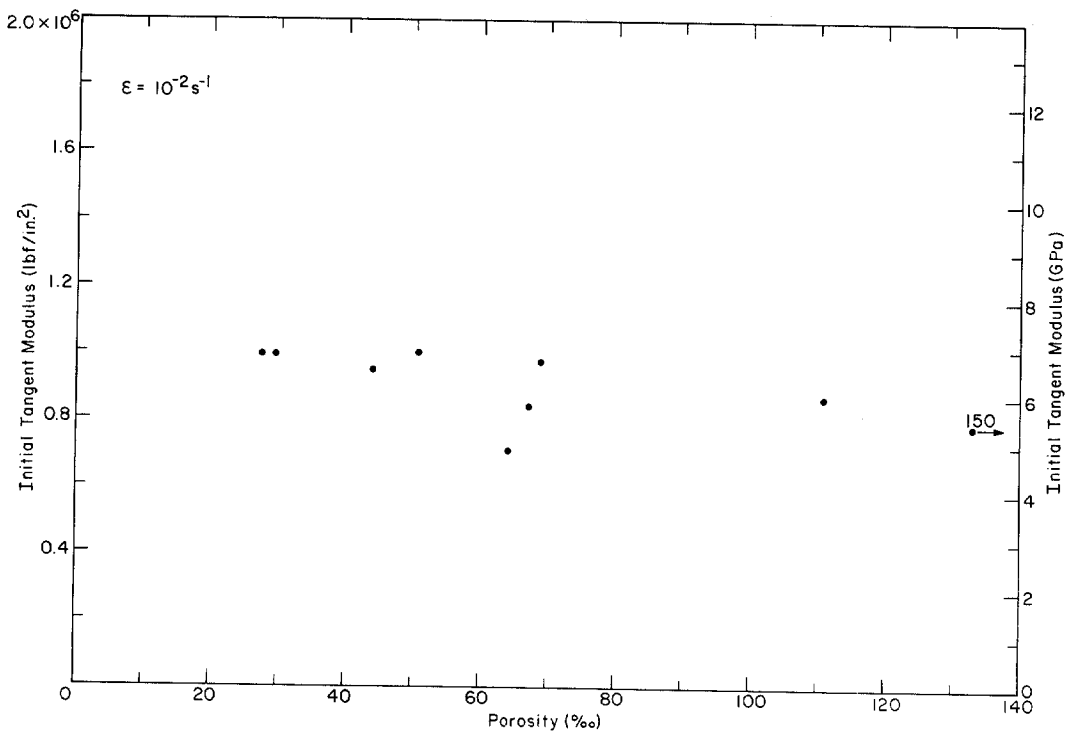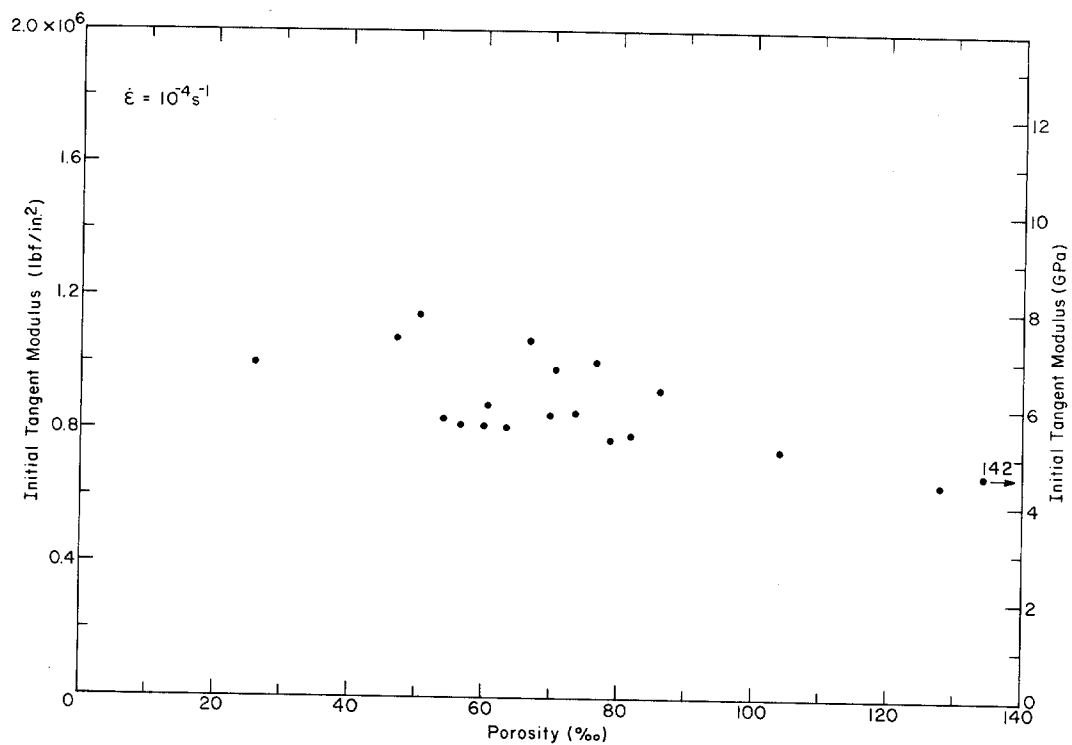
a. Tests conducted at -5°C (23°F).

Figure 23. Initial tangent modulus vs porosity for compression tests.
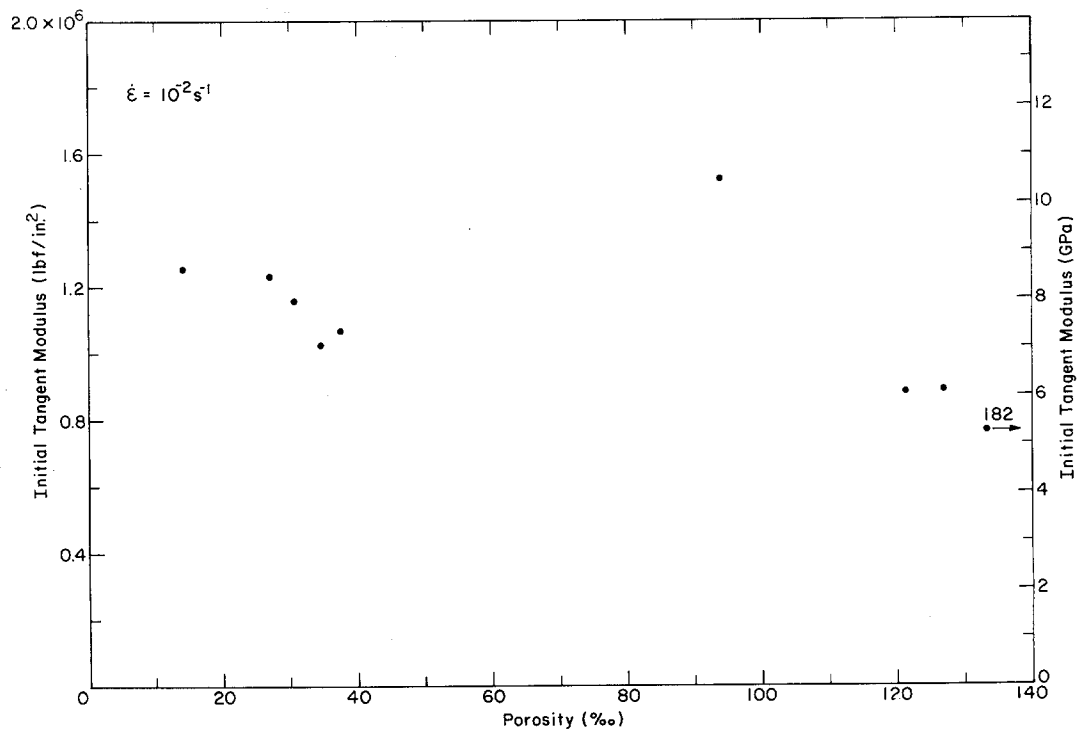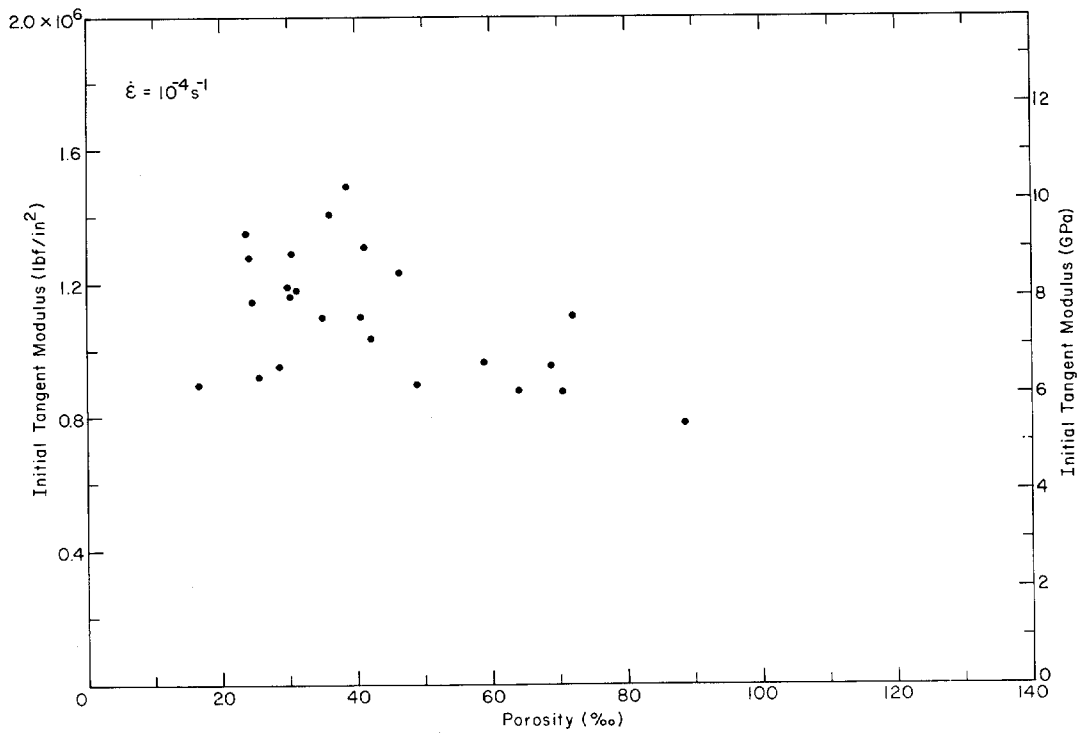
b. Tests conducted at -20°C (-4°F).

Figure 23 (cont'd). Initial tangent modulus vs porosity for compression tests.

28

CONSTANT-STRAIN-RATE UNIAXIAL TENSION TESTS

Test variables

In Phase II, we did 36 constant-strain-rate, uni-axial tension tests on multi-year pressure ridge samples that were vertically oriented. The tests were conducted at two strain rates, 10^{-5} and 10^{-3} s^{-1}, and at two temperatures, $-20°C$ ($-4°F$) and $-5°C$ ($23°F$). The number of tests at each test condition is summarized in Table 12. Details on the sample preparing and testing techniques are given by Mellor et al. (1984). The procedures used in Phase II were identical to those in Phase I, with the exception that, for the ice axial strains, the DCDT gauge length was increased from 10.2 cm (4.0 in.) to 11.4 cm (4.5 in.). In Phase I, tension tests were performed on ice samples from a multi-year floe and these data cannot be grouped with the Phase II ridge data.

Uniaxial tensile strength

A detailed tabulation of the results from the constant-strain-rate, uniaxial tension tests is given in Appendix B. The average tensile strength of the ice is plotted against strain rate in Figure 24. Average tensile strength values are also listed in Table 13.

In general, the tensile strength shows very little variation with strain rate or temperature. The lower mean strength obtained at 10^{-3} s^{-1} and $-5°C$ is probably attributable to the higher porosity of the samples.

The tensile strength is plotted against the ice porosity in Figure 25. Disregarding variations in

Table 12. Number of uniaxial tension tests at different temperatures and strain rates.

	$\dot{\epsilon}$		
	10^{-5} s^{-1}	10^{-3} s^{-1}	Total
$-5°C$ (23°F)	9V*	9V	18V
$-20°C$ ($-4°F$)	9V	9V	18V
Total	18V	18V	36V

* V—vertical.

the ice structure, we see a tendency for the ice strength to decrease with increasing porosity.

Failure strains

Average tensile failure strains at the peak or maximum stress for each test condition are given in Table 14. In general, the samples failed at 0.01 to 0.02% strain.

Initial tangent modulus

Estimates of the initial tangent modulus were obtained from the initial slope of the force-displacement curves. The results are plotted against strain rate in Figure 26 and listed in Table 15. The modulus is also plotted against the ice porosity in Figure 27.

The initial tangent modulus data show a slight increase with increasing strain rate, and a slight decrease with increasing temperature and porosity. Relative to the compressive initial tangent modulus data, variations are small.
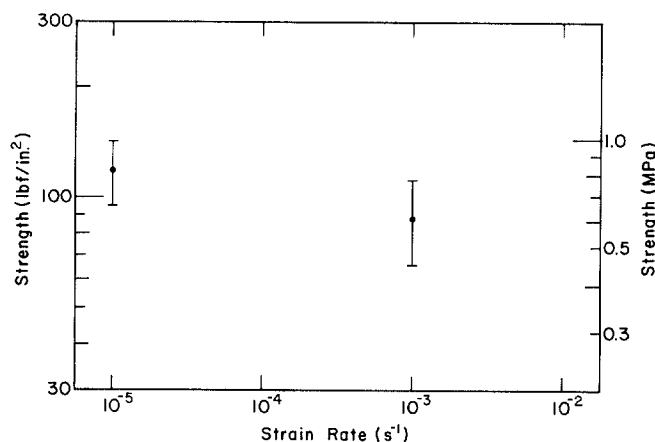
a. Tests conducted at -5°C (23°F).
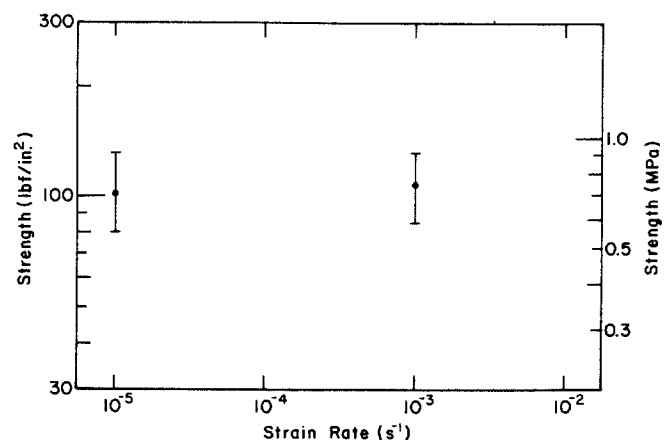
b. Tests conducted at -20°C (-4°F).

Figure 24. Uniaxial tensile strength vs strain rate. The bars denote one standard deviation.

Table 13. Summary of uniaxial tensile strength data for Phase II.

| | Maximum | | Minimum | | Mean | | Mean porosity | No. of |
	(MPa)	(lbf in.$^{-2}$)	(MPa)	(lbf in.$^{-2}$)	(MPa)	(lbf in.$^{-2}$)	($^o/_{oo}$)	samples
				-5°C (23°F)				
10^{-5} s^{-1} V*	1.03	149	0.57	82	0.82 ± 0.17	119 ± 24	78	9
10^{-3} s^{-1} V	0.83	120	0.41	60	0.61 ± 0.16	89 ± 23	108	9
				-20°C (-4°F)				
10^{-5} s^{-1} V	0.92	134	0.49	71	0.71 ± 0.16	103 ± 23	82	9
10^{-3} s^{-1} V	0.92	134	0.48	69	0.75 ± 0.16	109 ± 23	77	9

* V—vertical.
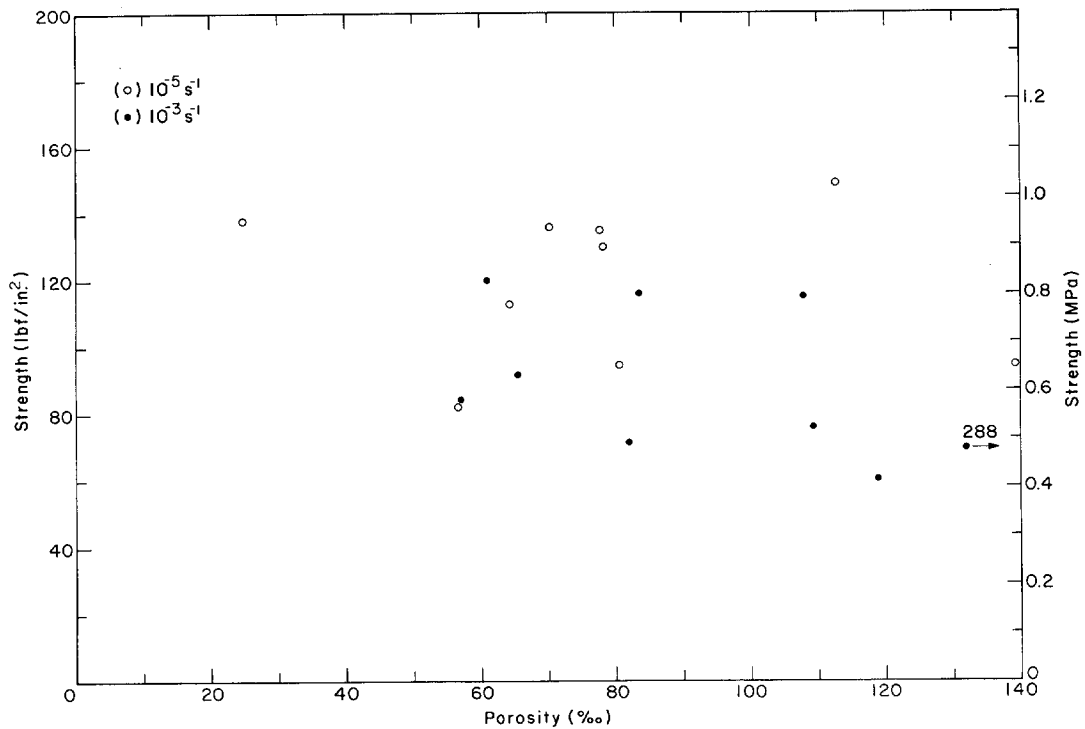
a. *Tests conducted at -5°C (23°F).*

Figure 25. Uniaxial tensile strength vs ice porosity.
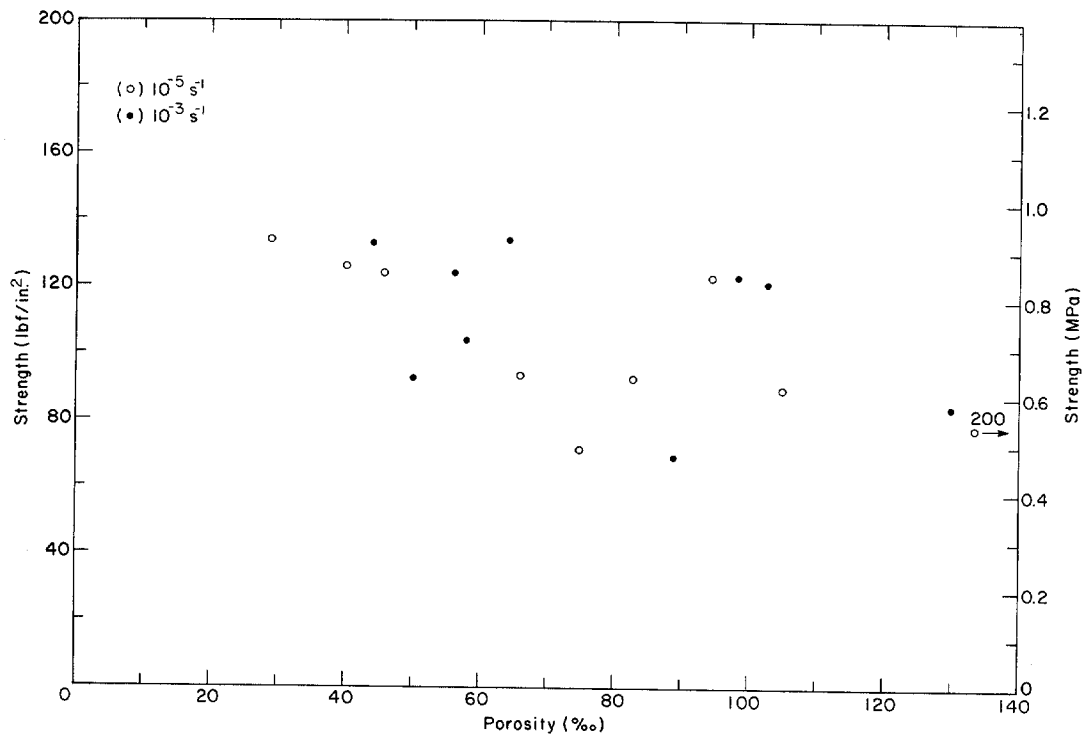
b. Tests conducted at -20°C (-4°F).

Figure 25 (cont'd).

**Table 14. Summary of tensile failure strain data (%) for
Phase II.**

	Maximum	Minimum	Mean	No. of samples
-5°C (23°F)				
10^{-5} s^{-1} V*	0.022	0.014	0.019 ± 0.002	9
10^{-3} s^{-1} V	0.013	0.007	0.010 ± 0.002	9
-20°C (-4°C)				
10^{-5} s^{-1} V	0.022	0.009	0.013 ± 0.004	9
10^{-3} s^{-1} V	0.012	0.009	0.011 ± 0.001	9

* V—vertical.

31
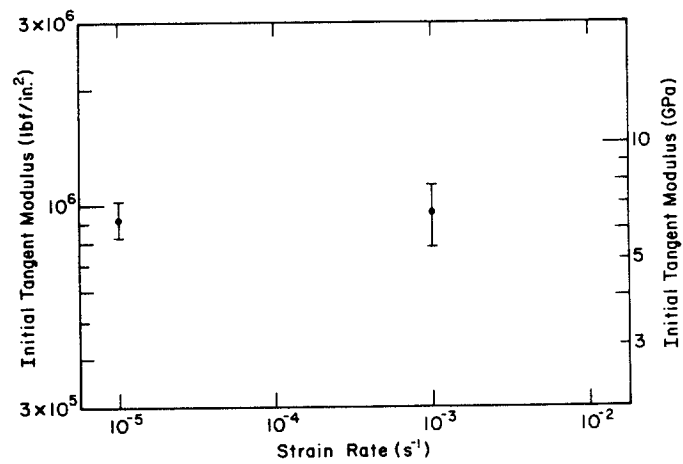
a. Tests conducted at –5°C (23°F).
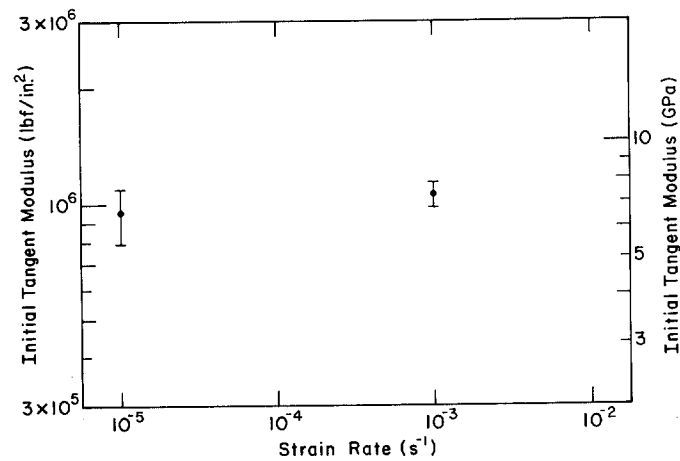
b. Tests conducted at –20°C (–4°F).

Figure 26. Initial tangent modulus in tension vs strain rate.

Table 15. Summary of initial tangent modulus data for Phase II tension tests.

	Maximum		Minimum		Mean		Mean porosity ($^o/_{oo}$)	No. of samples
	(GPa)	*(lbf in.$^{-2}$)*	*(GPa)*	*(lbf in.$^{-2}$)*	*(GPa)*	*(lbf in.$^{-2}$)*		
–5°C (23°F)								
10^{-5} s^{-1} V*	7.59	1.100×10^6	5.42	0.786×10^6	6.39 ± 0.68	$0.927 \pm 0.099 \times 10^6$	78	9
10^{-3} s^{-1} V	8.32	1.207	4.25	0.616	6.60 ± 1.19	0.957 ± 0.173	108	9
–20°C (–4°C)								
10^{-5} s^{-1} V	7.82	1.134	4.17	0.604	6.54 ± 1.12	0.949 ± 0.162	82	9
10^{-3} s^{-1} V	8.12	1.177	6.59	0.955	7.31 ± 0.54	1.060 ± 0.079	77	9

* V—vertical.

32
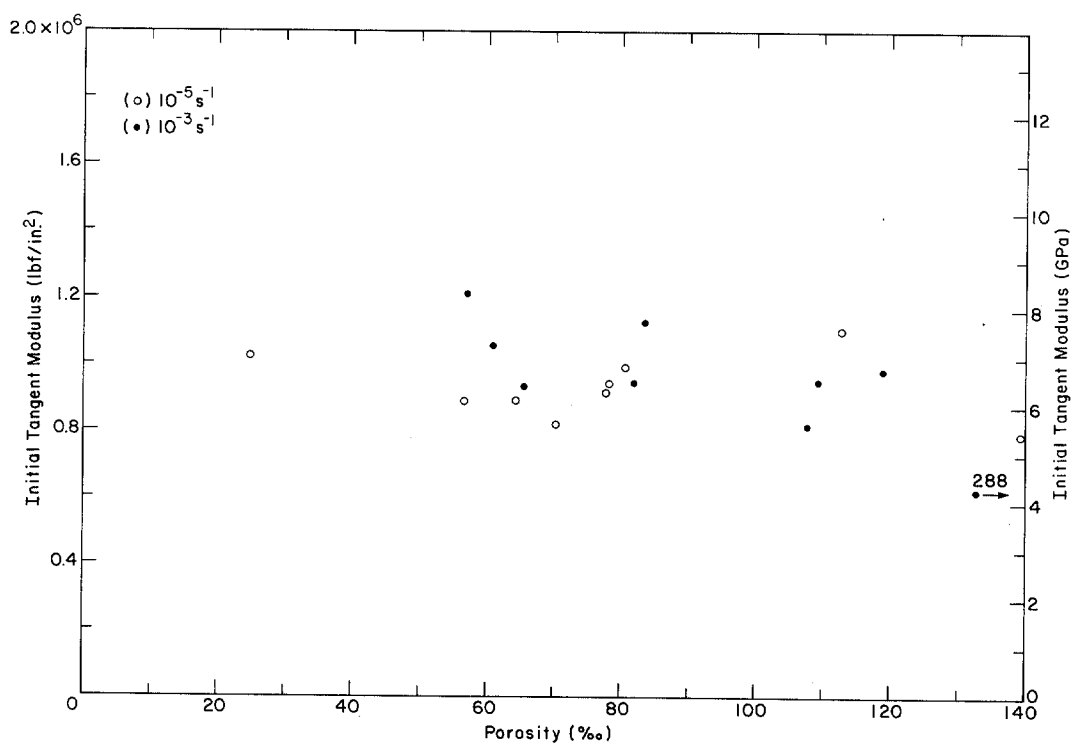
a. Tests conducted at -5 °C (23 °F).
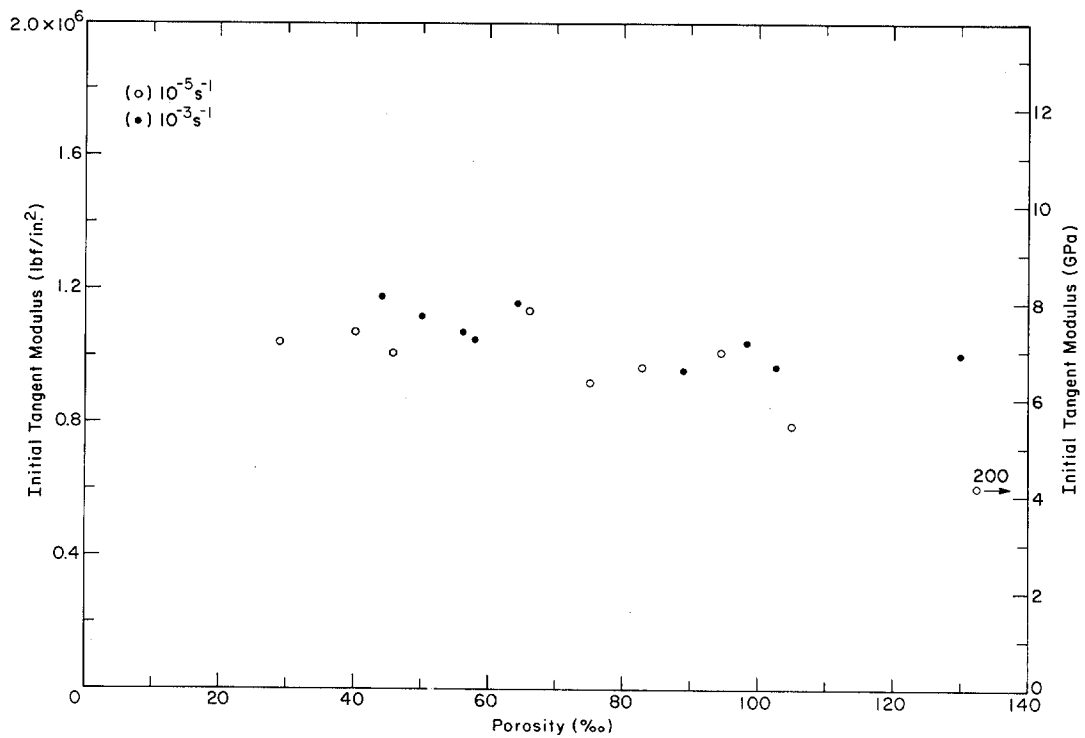
b. Tests conducted at -20 °C (-4 °F).

Figure 27. Initial tangent modulus vs porosity for tension tests.

33

CONSTANT-STRAIN-RATE
TRIAXIAL TESTS

Equipment

Conventional triaxial tests were carried out on the closed-loop testing machine using sample preparing and testing techniques similar to those employed in Phase I. As a result of our experience in Phase I, the triaxial cell was modified to increase its load bearing capacity to 350 kN (80,000 lbf) and confining pressure capacity to 24 MPa (3500 lbf/in.²). Heavier latex membranes were also placed around the sample to prevent penetration of hydraulic fluid into the sample. A 22-kN (100,000-lbf) load cell was provided by Shell to measure axial forces in excess of 11 kN (50,000 lbf). The upper cylinder of the triaxial cell was also modified such that samples could be tested at confining-pressure-to-axial-stress ratios of 0.25 and 0.50.

Test variables

We executed a total of 55 triaxial tests on multi-year pressure ridge samples at different test temperatures, nominal strain rates and confining pressures. The number of tests at each test condition is summarized in Table 16. In Phase I, triaxial tests were carried out on multi-year floe samples at confining-pressure-to-axial-stress ratios of 0.46 and 0.64 at the same temperatures and strain rates.

Synthane end caps

During the analysis of the Phase II triaxial test data, we found that the confined initial tangent modulus data of the ice were consistently lower than the initial tangent modulus data of the uniaxial or unconfined specimens. This caused some concern in that, intuitively, we would expect the confined modulus to be greater. Any confinement should reduce the axial displacement for a given load and thereby increase the measured modulus.

After checking our testing techniques and data reduction procedures, we concluded that the lower confined modulus values were caused by the use of the synthane end caps in the triaxial cell with externally mounted displacement transducers (Fig. 28). In effect, because sample displacements were measured outside the triaxial cell, the synthane end caps became a compliant element in the otherwise stiff loading system. If displacements were measured on the sample as in the uniaxial tests, the synthane end caps would not have presented any problems.

In addition to providing low confined modulus values, the synthane end caps and externally mounted displacement transducers also resulted in slightly lower ice strain rates.

Despite the problems of using synthane end caps in the triaxial cell, we hoped that the true ice modulus and strain rate could be determined given the mechanical properties of the synthane. Uniaxial and triaxial tests were done on a synthane specimen to determine the synthane properties, and equations were derived to calculate the actual ice modulus and strain rate from the test results.

The uniaxial and triaxial compression tests were performed on a 4.2-in. (10.8-cm) diameter, 14-in. (35.6-cm) long synthane sample at 20° and -10°C. The sample was tested at two strain rates, 10^{-3} and 10^{-5} s^{-1}. Confining-pressure-to-axial-stress ratios of 0, 0.25, and 0.50 were used in the triaxial tests.

Based on our experience with the triaxial cell, means for measuring axial displacements on the triaxial cell were improved as shown in Figure 29. The test strain rate in the new setup was controlled with the averaged output from two extensometers. The mounting positions of the extensometers were also moved from the upper cylinder to the shaft

Table 16. Number of triaxial tests at different temperatures, nominal strain rates and confining-pressure-to-axial-stress ratios (σ_r/σ_a).

| | $\dot{\epsilon}$ | | | | |
| | $\sigma_r/\sigma_a = 0.25$ | | $\sigma_r/\sigma_a = 0.50$ | | |
	10^{-5} s^{-1}	10^{-3} s^{-1}	10^{-5} s^{-1}	10^{-3} s^{-1}	Total
-5°C (23°F)	10V*	—	9V	9V	28V
-20°C (-4°F)	—	9V	9V	9V	27V
Total	10V	9V	18V	18V	55V

* V—vertical.

34
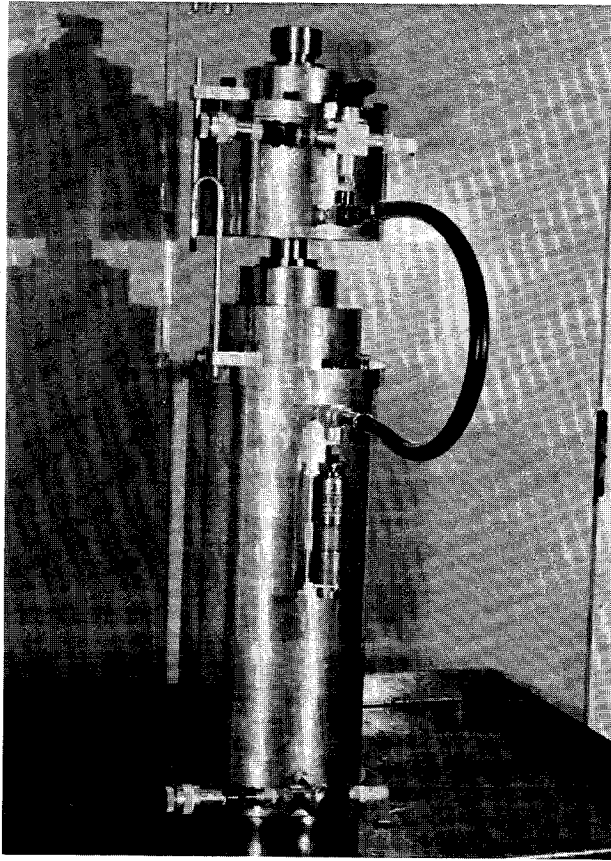
Figure 28. Triaxial cell with external mounts for extensometer.
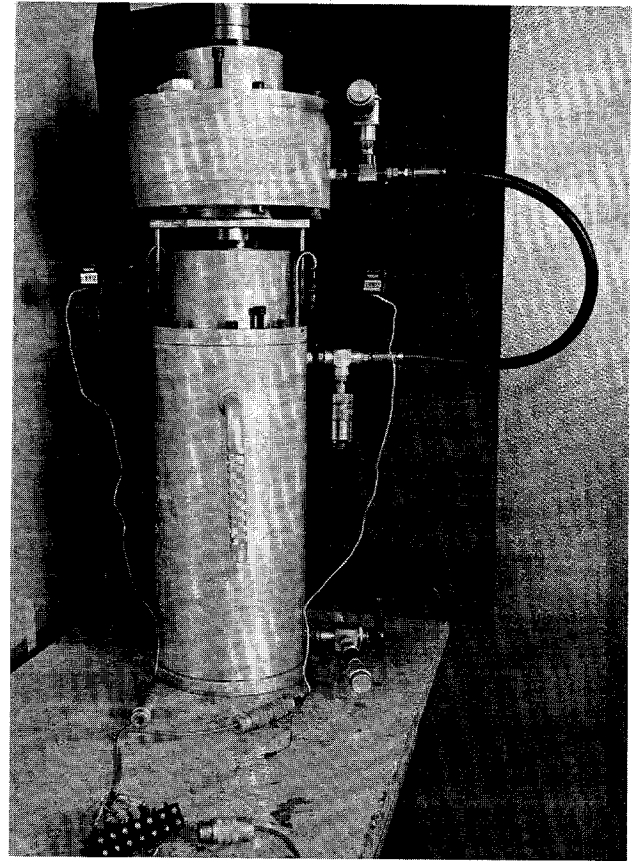
Figure 29. Triaxial cell with two external extensometers.

going into the triaxial cell. Previous test results indicated that the upper cylinder rotated slightly at the beginning of a test.

From the uniaxial and triaxial tests the synthane was found to have a modulus of 7.77×10^5 lbf/in.^{2} (5.36 GPa) and a Poisson's ratio of 0.21. The modulus and Poisson's ratio varied little with either strain rate or temperature. The tests also provided a measure of the loading train deflection, 1.4×10^{-7} in./lbf (8.0×10^{-10} m/N), which showed little variation with strain rate, confining pressure and temperature.

Given the synthane properties and loading train deflection, it is possible to calculate the actual test strain rate and ice modulus. The total measured displacement $\Delta \ell$ is equal to the sum of the displacements from the ice sample $\Delta \ell_s$, the synthane end caps $\Delta \ell_c$, and the loading train $\Delta \ell_\ell$:

$$\Delta \ell_t = \Delta \ell_s + \Delta \ell_c + \Delta \ell_\ell \tag{1}$$

or

$$\frac{\Delta \ell_t}{F} = \frac{\Delta \ell_s}{F} + \frac{\Delta \ell_c}{F} + \frac{\Delta \ell_\ell}{F} \tag{2}$$

where F is the applied load. From the synthane property tests, we have

$$\frac{\Delta \ell_\ell}{F} = C \tag{3}$$

where $C = 8.0 \times 10^{-10}$ m/N (1.40×10^{-7} in./lbf) and for the two end caps

$$\frac{\Delta \ell_c}{F} = \frac{2 \ell_c}{A_c E_c} (1 - 2 v_c k) \tag{4}$$

35

where ℓ_c = end cap thickness (5.08 cm) (2 in.)
A_c = end cap area (89.7 cm²) (13.9 in.²)
E_c = end cap modulus (5.36 GPa) (7.77 × 10⁵ lbf/in.²)
v_c = end cap Poisson's ratio (0.21)
k = confining-pressure-to-axial-stress ratio (0, 0.25, 0.50)

or

$$\frac{\Delta \ell_c}{F} = 2.11 \times 10^{-9} \,(1-0.42\,k)\, \text{m/N}. \qquad (5)$$

To put eq 3 and 5 into perspective, a 25.4-cm (10-in.) long, 10.2-cm (4-in.) diameter ice sample with a modulus of 5.17 GPa (7.5 × 10⁵ lbf/in.²) would deflect

$$\frac{\Delta \ell}{F} = 6.01 \times 10^{-9} \,(1-2\,v_s k)\, \text{m/N}.$$

Under uniaxial or low confining pressure, deformation of the load train and end caps would account for about 33% of the total displacement.

By combining eq 1, 3 and 4 and dividing by ℓ_s, the sample length, we obtain

$$\frac{\Delta \ell_t}{\ell_s} = \frac{\Delta \ell_s}{\ell_s} + \frac{2\ell_c F}{\ell_s A_c E_c}\,(1-2\,v_c k)+ \frac{CF}{\ell_s} \qquad (6)$$

where $\Delta \ell_t/\ell_s$ is the nominal strain ϵ_n, and $\Delta \ell_s/\ell_s$ is the true sample strain ϵ_s. Solving for the true sample strain in terms of the nominal strain, we get

$$\epsilon_s = \epsilon_n - \frac{2\ell_c F}{\ell_s A_c E_c}\,(1-2\,v_c k) - C\frac{F}{\ell_s} \qquad (7)$$

and dividing by Δt

$$\dot{\epsilon}_s = \dot{\epsilon}_n - \frac{2\ell_c \dot{F}}{\ell_s A_c E_c}\,(1-2\,v_c k) - C\frac{\dot{F}}{\ell_s} \qquad (8)$$

From eq 7 we can also obtain a relationship between the measured (E_m) and actual (E_s) confined ice modulus by multiplying by A_s/F where A_s is the cross-sectional area of the sample:

$$\frac{\epsilon_s A_s}{F} = \frac{\epsilon_n A_s}{F} - \left(\frac{A_s}{\ell_c}\,\frac{2\ell_c}{A_c E_c}(1-2\,v_c k)+ C\right)$$

or $\qquad\qquad\qquad\qquad\qquad\qquad (9)$

$$\frac{1}{E_s} = \frac{1}{E_m} - \frac{A_s}{\ell_s}\left(\frac{2\ell_c}{A_c E_c}\,(1-2\,v_c k)+ C\right).$$

The actual sample strain rate during a test can be found from eq 8 where by substitution we have

$$\dot{\epsilon}_s = \dot{\epsilon}_n - [8.32 \times 10^{-9}\,(1-0.42\,k)$$
$$+ 3.15 \times 10^{-9}]\,\dot{F} \qquad (10)$$

where $\dot{F}$ is the load rate in N/s. At the beginning of the test $\dot{F}$ is at its maximum and the actual strain rate is at its lowest value for the entire test:

$$\dot{F} = \dot{F}_o = A_s E_m \dot{\epsilon}_n.$$

At the peak stress

$$\dot{F} = \dot{F}_p = 0$$

and

$$\dot{\epsilon}_s = \dot{\epsilon}_n.$$

The average strain rate up to the peak stress can be found by using

$$\dot{F}_{avg} = \frac{\sigma_m A_s}{t_m}$$

where σ_m is the peak stress and t_m is the time to failure.

The actual initial tangent modulus E_s can be directly determined from eq 9. Equation 7 can be used to correct sample failure strains.

Triaxial strength

A detailed tabulation of the measured results from the triaxial tests is given in Appendix B. The average confined compressive strength of the ice σ_1 for each test condition is plotted against the confining pressure ($\sigma_2 = \sigma_3$) at failure in Figure 30. Average uniaxial compressive strength data from Phase I are included for comparison. The uniaxial strength falls on the ordinate or zero confining pressure. In making comparisons between the unconfined and confined compressive strength data, it should be noted that the Phase I ridge samples had a much lower porosity. Table 17 summarizes the Phase II triaxial strength data.

As observed in Phase I, the confined compressive strength increases with decreasing temperature, increasing strain rate and increasing confining pressure. Because of variability of the ice structure among samples, the data show considerable scatter. The data at 10^{-5} s^{-1} suggest that fail-

36
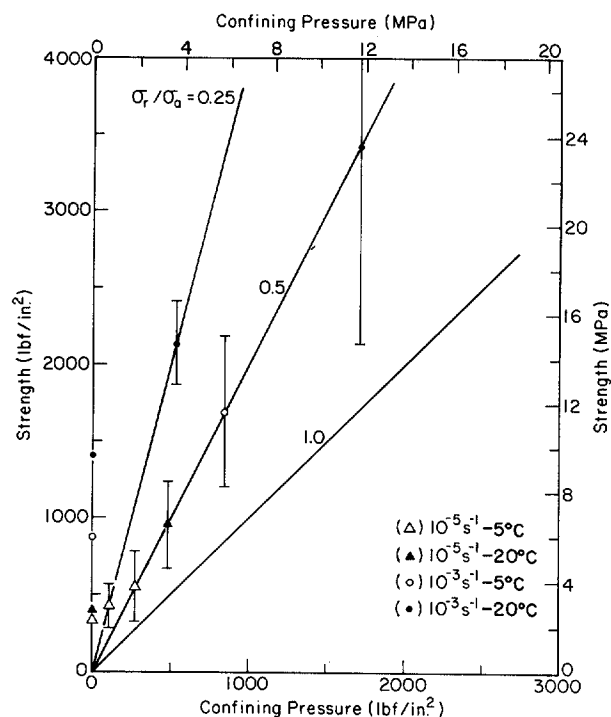
Figure 30. Compressive strength versus confining pressure for multi-year pressure ridge samples at different temperatures and nominal strain rates. The bars denote one standard deviation from the mean strength at a given load ratio.

Table 17. Summary of confined strength data for different nominal strain rates, temperatures and confining-pressure-to-axial-stress ratios (σ_r/σ_a).

	σ_r/σ_a	Maximum (MPa)	Maximum (lbf in.$^{-2}$)	Minimum (MPa)	Minimum (lbf in.$^{-2}$)	Mean (MPa)	Mean (lbf in.$^{-2}$)	Mean porosity ($^o/_{oo}$)	No. of samples
				-5°C (23°F)					
10^{-5} s^{-1} V*	0.25	3.95	573	1.14	166	2.86 ± 0.98	415 ± 142	79	10
10^{-5} s^{-1} V	0.50	6.61	959	2.28	330	3.81 ± 1.59	552 ± 231	86	9
10^{-3} s^{-1} V	0.50	17.94	2602	5.43	788	11.70 ± 3.41	1697 ± 495	78	9
				-20°C (-4°F)					
10^{-3} s^{-1} V	0.25	17.07	2475	11.58	1679	14.77 ± 1.90	2141 ± 275	77	9
10^{-5} s^{-1} V	0.50	11.03	1600	3.95	573	6.59 ± 1.97	956 ± 286	82	9
10^{-3} s^{-1} V	0.50	38.63	5602	8.34	1210	23.50 ± 8.73	3408 ± 1266	57	9

* V—vertical.

ure of the ridge ice samples at low strain rates may be described by a Tresca or Von Mises yield criteria. The yield surface parallels the hydrostat (confined-pressure-to-axial-stress ratio $[\sigma_r/\sigma_a]$ = 1). This supports the observations made by Jones (1982) who investigated the confined compressive strength of freshwater polycrystalline ice at low strain rates.

Failure strains

Average failure strains at the peak or maximum stress for each confined test condition are given in Table 18. The strain data have been corrected for deformation of the end caps and loading train. As expected, confinement reduces cracking and causes the ice to be more ductile, resulting in a larger strain at failure. As the confining pressure increases, the failure strain is observed to increase in our range of test conditions.

37

Table 18. Summary of confined failure strain data (%) for different nominal strain rates, temperatures and confining-pressure-to-axial-stress ratios (σ_r/σ_a).

σ_r/σ_a	Maximum	Minimum	Mean	Mean porosity (%/oo)	No. of samples
		–5°C (23°F)			
10^{-5} s^{-1} V* 0.25	0.97	0.35	0.70 ± 0.25	79	10
10^{-5} s^{-1} V 0.50	4.98	0.47	1.50 ± 1.47	86	9
10^{-3} s^{-1} V 0.50	0.87	0.24	0.42 ± 0.19	78	9
		–20°C (–4°C)			
10^{-3} s^{-1} V 0.25	0.55	0.36	0.47 ± 0.07	77	9
10^{-5} s^{-1} V 0.50	4.97	0.59	1.86 ± 1.79	82	9
10^{-3} s^{-1} V 0.50	0.89	0.14	0.57 ± 0.23	57	9

* V—vertical.

Table 19. Summary of confined initial tangent modulus data for different nominal strain rates, temperatures and confining-pressure-to-axial-stress ratios (σ_r/σ_a). Modulus data have been corrected for deformation of synthane end caps.

σ_r/σ_a	Maximum (GPa)	Maximum (lbf in.$^{-2}$)	Minimum (GPa)	Minimum (lbf in.$^{-2}$)	Mean (GPa)	Mean (lbf in.$^{-2}$)	Mean porosity (%/oo)	No. of samples
				–5°C (23°F)				
10^{-5} s^{-1} V* 0.25	8.41	1.219×10^6	1.38	0.200×10^6	2.78 ± 2.24	$0.403 \pm 0.325 \times 10^6$	79	9
10^{-5} s^{-1} V 0.50	3.95	0.573	1.31	0.190	2.39 ± 0.83	0.346 ± 0.121	86	9
10^{-3} s^{-1} V 0.50	8.10	1.175	3.75	0.544	5.87 ± 1.47	0.851 ± 0.213	78	9
				–20°C (–4°F)				
10^{-3} s^{-1} V 0.25	6.25	0.906	2.49	0.361	4.60 ± 1.30	0.667 ± 0.188	77	9
10^{-5} s^{-1} V 0.50	4.48	0.649	2.30	0.334	3.09 ± 0.81	0.448 ± 0.117	82	9
10^{-3} s^{-1} V 0.50	15.98	2.317	6.78	0.983	11.50 ± 3.10	1.668 ± 0.449	57	9

* V—vertical.

Initial tangent modulus

Estimates of the initial tangent modulus were obtained from the force–displacement curves. The results are summarized in Table 19 for each test condition. As in the uniaxial compression tests, the initial tangent modulus increases with increasing strain rate and decreasing temperature. Confinement also appears to increase the ice modulus; however, there are contradictory trends in the data.

Effect of synthane end caps on results

The mean measured modulus, mean strength and mean time to failure for each of the six triaxial test conditions are given in Table 20. These values were used to calculate a representative initial strain rate, average strain rate and corrected mean modulus for each test condition. The results are presented in Table 21.

Use of synthane end caps in the triaxial cell appears to have only a slight effect on the actual strain rate during the test. The greatest error is introduced under test conditions where the ice is the stiffest, that is, at high pressure ($k = 0.50$), high strain rate (10^{-3} s^{-1}) and low temperature (–20°C). Even under these conditions, the actual and nominal strain rates only differ by 25%.

The calculated actual modulus values still appear to be too low when they are compared to the modulus values obtained from the uniaxial test

38

Table 20. Mean measured modulus, strength and time to failure values for each test condition.

	P/σ = 0.25		P/σ = 0.50	
	$\dot{\epsilon}_n = 10^{-5}\ s^{-1}$	$\dot{\epsilon}_n = 10^{-3}\ s^{-1}$	$\dot{\epsilon}_n = 10^{-5}\ s^{-1}$	$\dot{\epsilon}_n = 10^{-3}\ s^{-1}$
$T = -5°C$ $\quad E_m$	= 2.08 Gpa		= 1.98 GPa	= 3.96 GPa
σ_m	= 2.86 MPa		= 3.81 MPa	= 11.70 MPa
t_m	= 720 s		= 1540 s	= 4.97 s
$T = -20°C$ $\quad E_m$		= 3.25 GPa	= 2.46 GPa	= 5.91 GPa
σ_m		= 14.77 MPa	= 6.59 MPa	= 23.5 MPa
t_m		= 6.00 s	= 1909 s	= 7.24 s

Table 21. Corrected strain rate and modulus for mean test data at each test condition.

	P/σ = 0.25		P/σ = 0.50	
	$\dot{\epsilon}_n = 10^{-5}\ s^{-1}$	$\dot{\epsilon}_n = 10^{-3}\ s^{-1}$	$\dot{\epsilon}_n = 10^{-5}\ s^{-1}$	$\dot{\epsilon}_n = 10^{-3}\ s^{-1}$
$T = -5°C$ $\quad \dot{\epsilon}_o$	= 8.21×10^{-6} s^{-1}		= 8.44×10^{-6} s^{-1}	= 6.87×10^{-4} s^{-1}
$\dot{\epsilon}_{avg}$	= 9.66×10^{-6} s^{-1}		= 9.80×10^{-6} s^{-1}	= 8.14×10^{-4} s^{-1}
E_s	= 2.54 GPa		= 2.34 GPa	= 5.76 GPa
$T = -20°C$ $\quad \dot{\epsilon}_o$		= 7.20×10^{-4} s^{-1}	= 8.06×10^{-6} s^{-1}	= 5.33×10^{-4} s^{-1}
$\dot{\epsilon}_{avg}$		= 7.88×10^{-4} s^{-1}	= 9.73×10^{-6} s^{-1}	= 7.43×10^{-4} s^{-1}
E_s		= 4.51 GPa	= 3.05 GPa	= 11.10 GPa

specimens. This suggests that there are other displacement errors not properly accounted for, such as closure across the end cap/upper actuator interface. Appendix C demonstrates that closure errors less than 0.002 in. (0.051 mm) can significantly reduce the initial tangent modulus at the beginning of the test when displacement transducers are not placed directly on the ice.

Future confined compression tests will be carried out in an enlarged triaxial cell that can accommodate a pair of LVDTs (linear variable differential transducers) mounted on the sample end caps. The LVDTs will be used to measure sample strains and control the test strain rate.

CONSTANT-LOAD COMPRESSION TESTS

Test variables

In Phase II, we executed 35 constant-load compression tests on multi-year pressure ridge samples that were vertically oriented. The tests were conducted at three loads and at two test temperatures. The number of tests at each test condition is summarized in Table 22. The small load tests at a stress of 0.69 MPa (100 lbf/in.²) were performed on a specially designed pneumatic loading jig, and the larger 2.07 and 4.14 MPa (300 and 600 lbf/in.²) tests were conducted on the materials testing machine. Sample preparing and testing techniques were identical to those used in Phase I (Mellor et al. 1984).

Test results

A detailed tabulation of the results from the constant load compression tests is given in Appendix B. The results are summarized in Table 23 and plotted in Figures 31 through 33. The strain-rate minimum for each curve was determined by differentiating each strain–time curve. The failure strain ϵ_f was defined as the strain at the strain-rate minimum, marking the onset of tertiary creep.

The strain-rate minimum of each test is plotted against the applied stress in Figure 31. In general,

39

Table 22. Number of constant-load compression tests performed at different loads and temperatues.

| | Temperature | | |
	-5°C (23°F)	-20°C (-4°F)	Total
σ			
0.69 MPa (100 lbf in.$^{-2}$)	9		9
2.07 MPa (300 lbf in.$^{-1}$)	8	9	17
4.14 MPa (600 lbf in.$^{-1}$)		9	9
Total	17	18	35

Table 23. Summary of constant-load compression test data for Phase II.

Stress: 0.69 MPa (100 lbf in.$^{-2}$)
Temperature: -5°C (23°F)

Samples: 9
Porosity: 76.6 ±43.8%$_{00}$

	Max	Min	Mean
$\dot{\epsilon}_{min}$, s^{-1}	9.12×10^{-7}	1.47×10^{-8}	1.62×10^{-7} ±2.85×10^{-7}
$\epsilon_f(FS)$, %	1.28	0.18	0.67 ±0.29
t_f, s	1.01×10^{5}	6.59×10^{3}	8.05×10^{4} ±5.25×10^{4}

Stress: 2.07 MPa (300 lbf in.$^{-2}$)
Temperature: -5°C (23°F)

Samples: 8
Porosity: 53.1 ±19.1%$_{00}$

	Max	Min	Mean
$\dot{\epsilon}_{min}$, s^{-1}	1.66×10^{-4}	3.29×10^{-6}	4.87×10^{-5} ±6.34×10^{-5}
$\epsilon_f(FS)$, %	0.80	0.20	0.49 ±0.20
t_f, s	1.68×10^{3}	8.29	4.61×10^{2} ±5.75×10^{2}

Stress: 2.07 MPa (300 lbf in.$^{-2}$)
Temperature: -20°C (-4°F)

Samples: 9
Porosity: 52.1 ±40.2%$_{00}$

	Max	Min	Mean
$\dot{\epsilon}_{min}$, s^{-1}	3.03×10^{-5}	3.98×10^{-7}	7.27×10^{-6} ±1.08×10^{-5}
$\epsilon_f(FS)$, %	1.03	0.07	0.46 ±0.35
t_f, s	4.79×10^{3}	7.94	2.33×10^{3} ±2.05×10^{3}

Stress: 4.14 MPa (600 lbf in.$^{-2}$)
Temperature: -20°C (-4°F)

Samples: 9
Porosity: 60.9 ±40.5%$_{00}$

	Max	Min	Mean
$\dot{\epsilon}_{min}$, s^{-1}	1.74×10^{-4}	2.00×10^{-5}	8.26×10^{-5} ±4.43×10^{-5}
$\epsilon_f(FS)$, %	0.18	0.10	0.13 ±0.03
t_f, s	1.74×10^{1}	6.75	1.11×10^{1} ±3.2×10^{0}
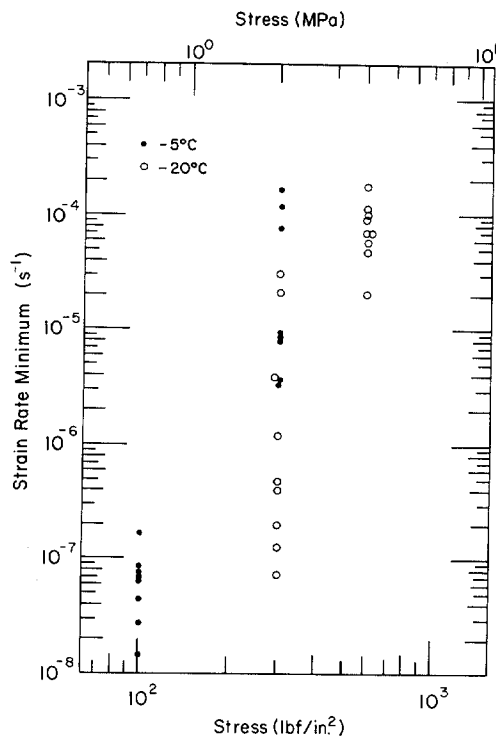
Figure 31. Strain-rate minimum vs applied stress for constant-load compression test specimens at -5°C (23°F) and -20°C (-4°F).
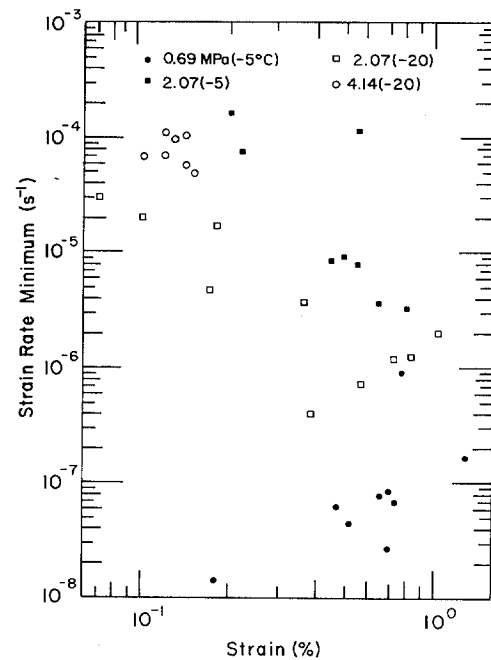
Figure 32. Strain-rate minimum vs strain at failure for constant-load compression test specimens at different applied stresses and temperatures.
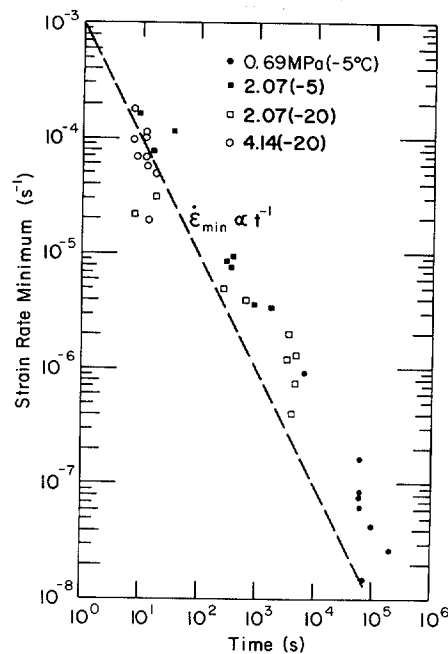
Figure 33. Strain-rate minimum vs time to failure for constant-load compression test specimens at different applied stresses and temperatures.

41

$\dot{\epsilon}_{min}$ increases as the applied stress increases and as the test temperature increases. These trends are consistent with those found in constant-strain-rate tests, supporting the correspondence between these two types of tests as suggested by Mellor (1979). The large scatter in the data is attributed to the large variation in ice structure between the different samples.

The strain-rate minimum is plotted against the failure strain for each sample in Figure 32. In general, $\dot{\epsilon}_{min}$ decreases with increasing ϵ_f, again supporting the correspondence between constant-load and constant-strain-rate tests. The strain-rate minimum is also observed to vary inversely with the time to failure as shown in Figure 33. This indicates that prior to the onset of tertiary creep, the ice can be described by a Burgers rheological model (Mellor 1979). A Burgers model consists of a series combination of the Kelvin–Voigt and Maxwell models. It is also interesting to note that the $\dot{\epsilon}_{min}$ decreases with decreasing temperature.

CONCLUSIONS

In Phase I a large number of uniaxial, constant-strain-rate compression tests were conducted on ice samples from 10 multi-year pressure ridges. These tests were done to investigate the magnitude and variations of ice strength within and between pressure ridges. The crystallographic structure of multi-year pressure ridges was also studied for the first time. In addition, techniques and procedures were developed to perform uniaxial, constant-strain-rate tension tests, constant-load compression tests and conventional triaxial tests. In Phase II we used these testing techniques to provide data for developing constitutive laws and failure criteria for multi-year pressure ridges. We again did a limited amount of ice structure work to help us further characterize the structure of multi-year pressure ridges and to explain the variation of ice strength between horizontal and vertical ice samples.

The combined test results of Phases I and II provide a foundation for developing constitutive laws and failure criteria for multi-year pressure ridges. However, before such analyses can be made in a meaningful manner, we need to examine the ice structure of all the test specimens. Preliminary structure analyses have shown that the ice structure of multi-year pressure ridge samples is highly variable and that the structure has a profound effect on the mechanical properties of the ice. Without characterizing the structure of each

specimen, we would be mixing numerous ice types in our analyses and we would have to contend with a large, unexplained variance in the input data and results. Plans are therefore being made to analyze the structure of all the Phase I and Phase II samples. Ice structure classification will also become a standard procedure in future phases of the project.

It appears that, in multi-year pressure ridges containing a large proportion of columnar sheet ice blocks, the horizontal ice strength may be significantly less than the vertical ice strength. This is because there may be preference for ice blocks to lie in a near horizontal position during ridge formation. The results of this study and those of earlier investigators (Peyton 1966) have shown that horizontal sheet ice samples are significantly weaker than vertical sheet ice samples. More field studies of the internal structure of first-year and multi-year pressure ridges are needed to capitalize on this finding. Using ice strength data from vertically oriented ridge specimens may be conservative in horizontal ridge loading problems.

In some respects it is difficult to combine the uniaxial compression test results from Phases I and II. This is because the Phase II samples contained significantly more columnar ice and were more porous. These difficulties can be remedied by characterizing the ice structure and porosity of each sample and, in a subsequent phase of the test program, test Phase I ice under Phase II test conditions and vice versa.

Before closing, it should also be mentioned that high temperature tests are still needed to define the mechanical properties of pressure ridge keels.

LITERATURE CITED

Cox, G.F.N. and W.F. Weeks (1983) Equations for determining the gas and brine volumes in sea ice samples. *Journal of Glaciology,* **29**(102): 306–316.
Cox, G.F.N., J.A. Richter-Menge, W.F. Weeks, M. Mellor and H.W. Bosworth (1984) The mechanical properties of multi-year sea ice. Phase I: Test results. USA Cold Regions Research and Engineering Laboratory, CRREL Report 84-9.
Jones, S.J. (1982) The confined compressive strength of polycrystalline ice. *Journal of Glaciology,* **28**(98): 171–178.
Mellor, M. (1979) Mechanical properties of polycrystalline ice. In *Physics and Mechanics of Ice* (P. Tryde, Ed.). Berlin: Springer-Verlag, pp. 217–245.

Mellor, M. (1983) Mechanical behavior of sea ice. USA Cold Regions Research and Engineering Laboratory, Monograph 83-1.

Mellor, M., G.F.N. Cox and H.W. Bosworth (1984) The mechanical properties of multi-year sea ice: Testing techniques. USA Cold Regions Research and Engineering Laboratory, CRREL Report 84-8.

Peyton, H.R. (1966) Sea ice strength. Geophysical Institute, University of Alaska, Report UAG R-182.

Rand, J.H. and M. Mellor (In prep.) Ice coring augers for shallow depth sampling. USA Cold Regions Research and Engineering Laboratory, CRREL Report.

Richter, J.A. and G.F.N. Cox (1984) A preliminary examination of the effect of structure on the strength of ice samples from multi-year pressure ridges. In *Proceedings of the ASME Third International Offshore Mechanics and Arctic Engineering Symposium, February, New Orleans*. Vol. 3, pp. 140–144.

Wang, Y.S. (1979) Crystallographic studies and strength tests of field ice in the Alaskan Beaufort Sea. In *Proceedings of the 5th International Conference on Port and Ocean Engineering under Arctic Conditions (POAC '79), August, Trondheim, Norway*. Vol. 1, pp. 346–355.

cm

320

330

340

350

360

cm

55

cm

520

530

540

550

560

cm

cm

600

610

620

630

640

cm

cm
640

650

660

670

680

cm

cm

880

890

900

910

920

cm

67
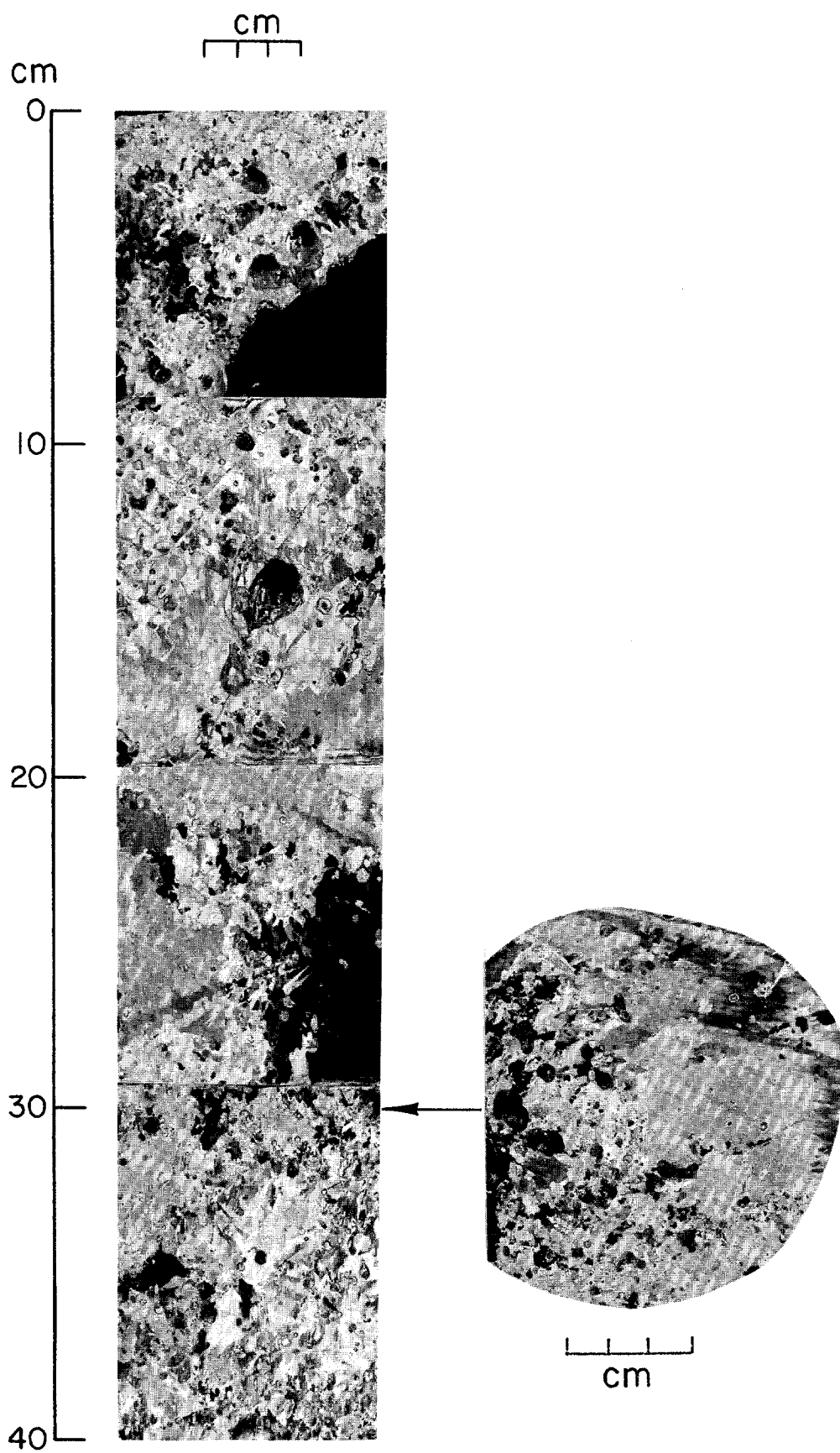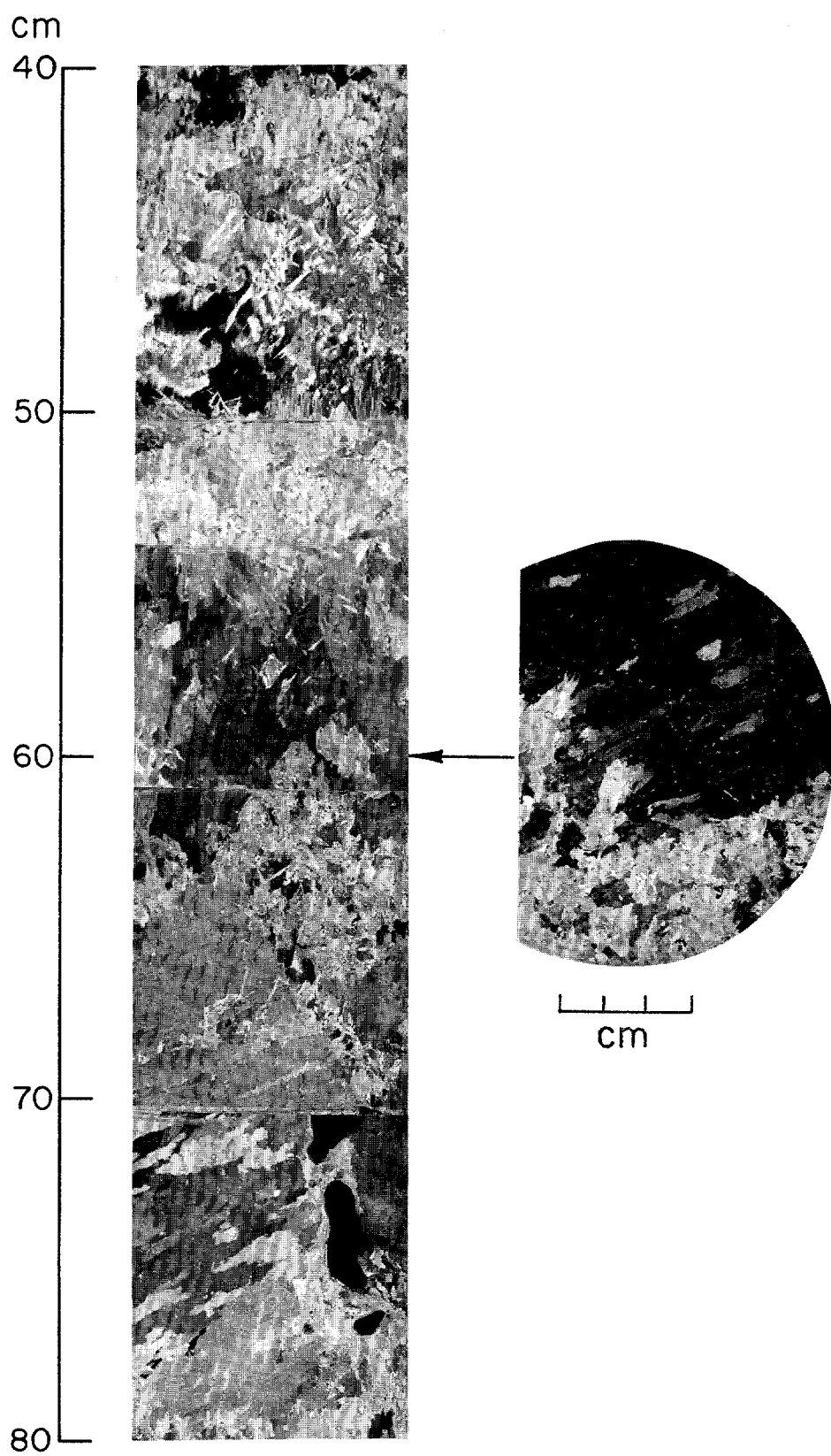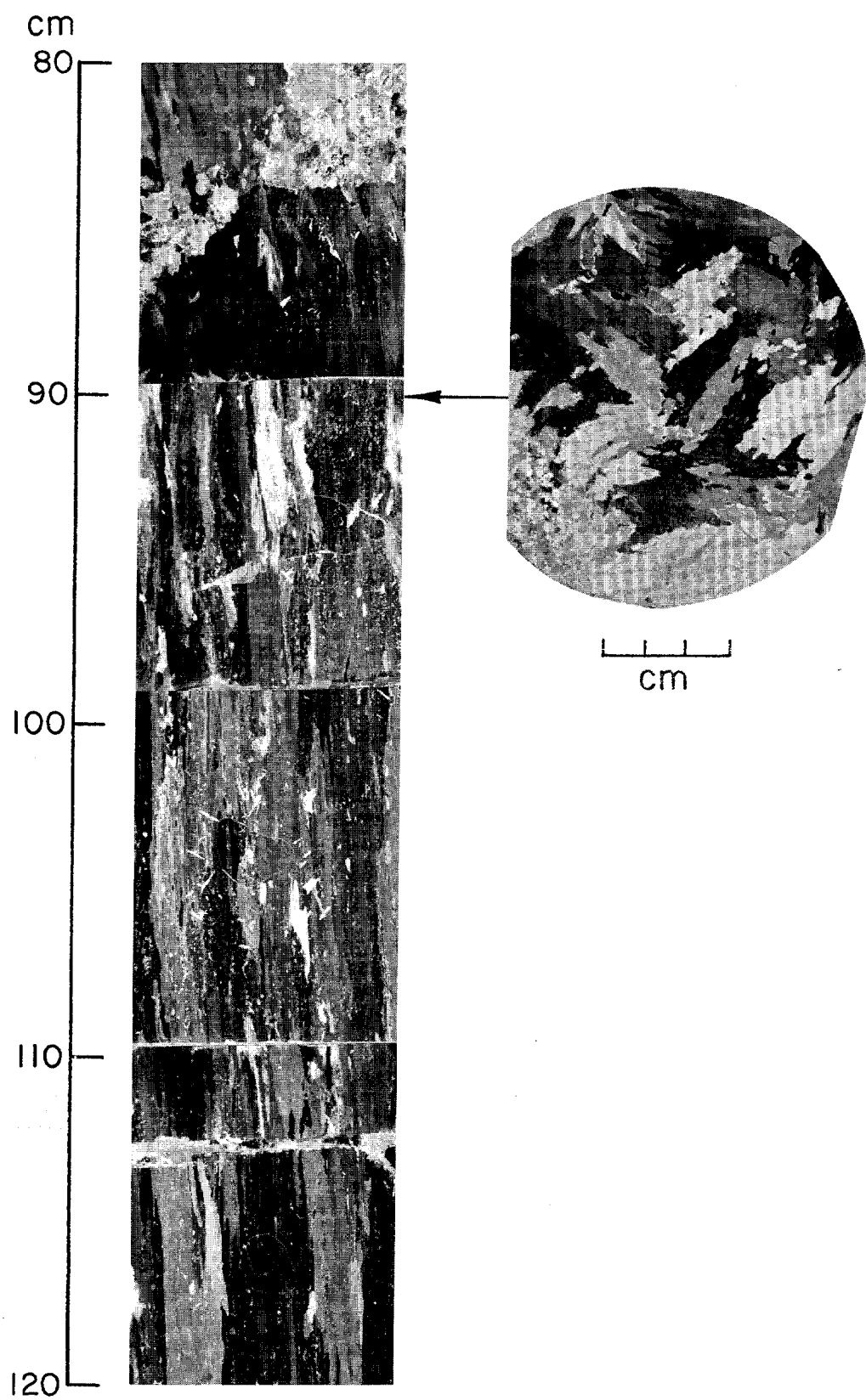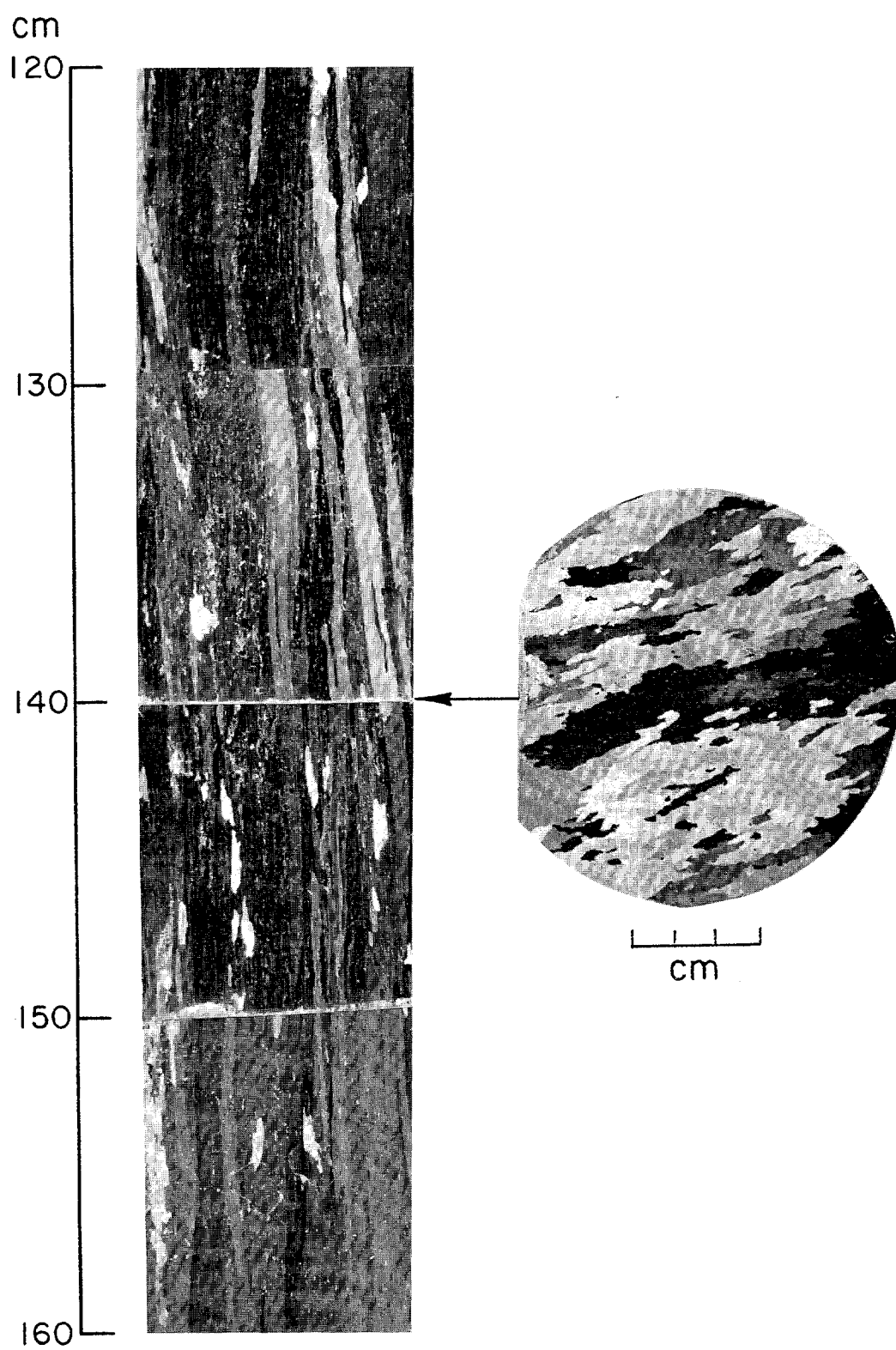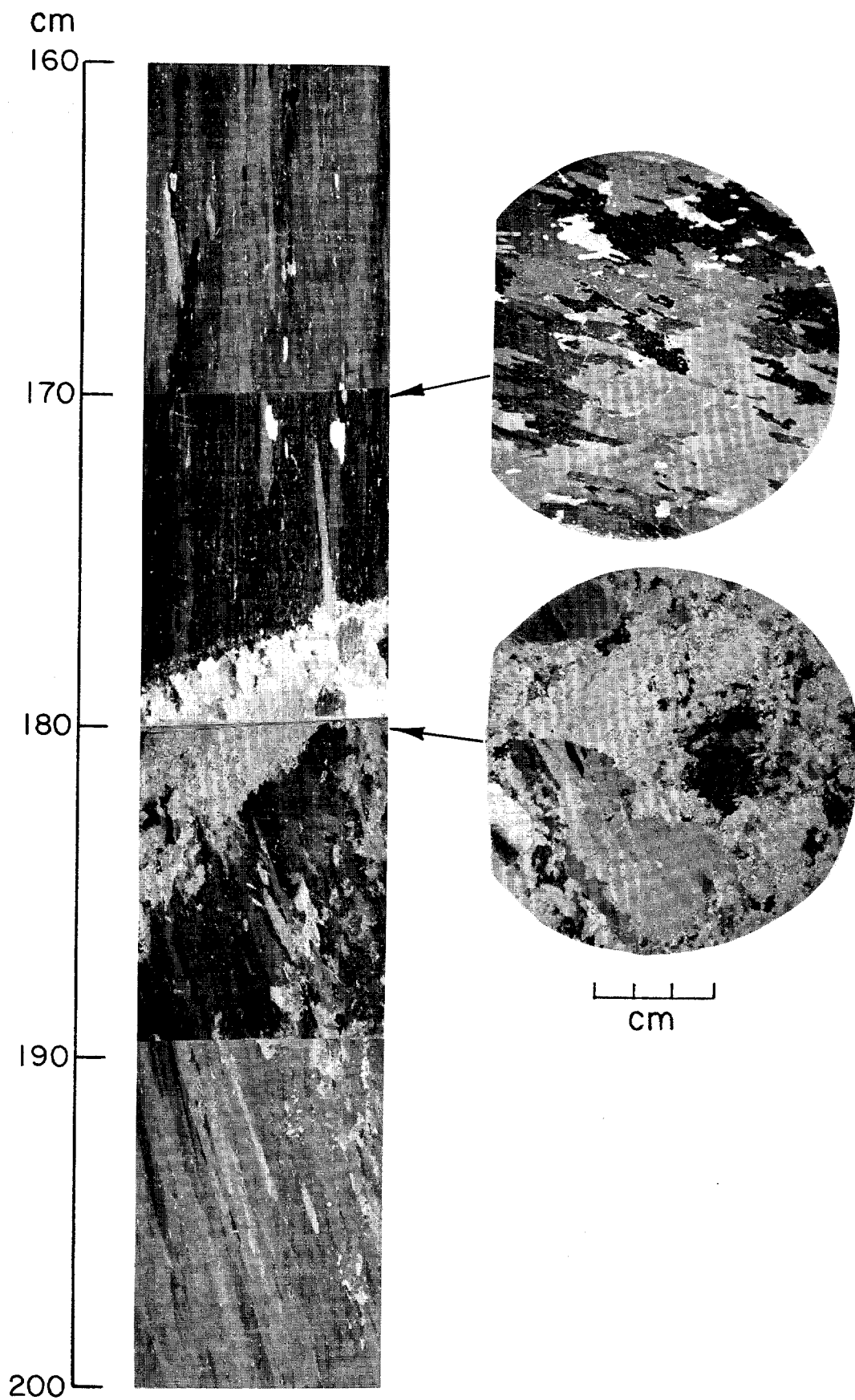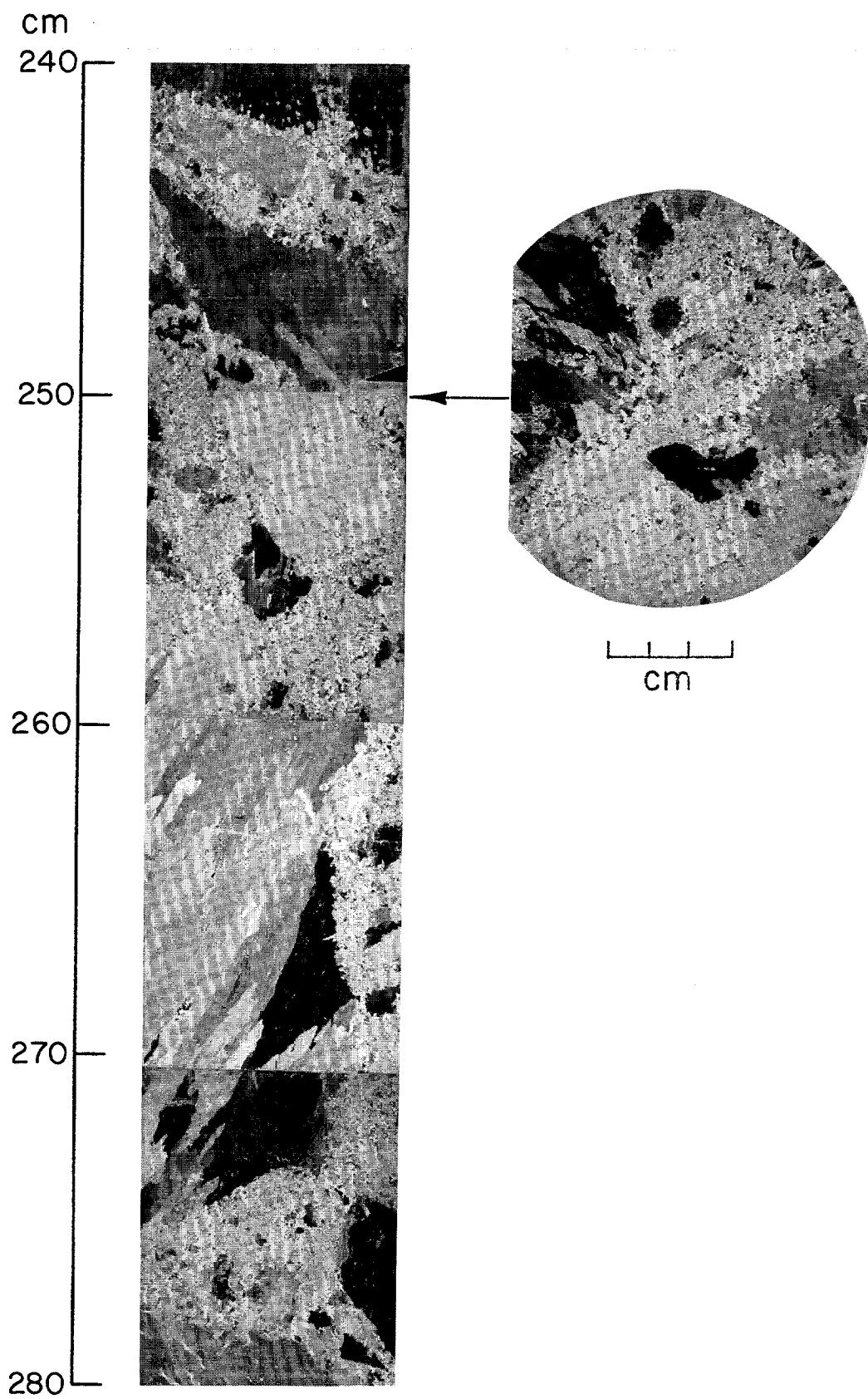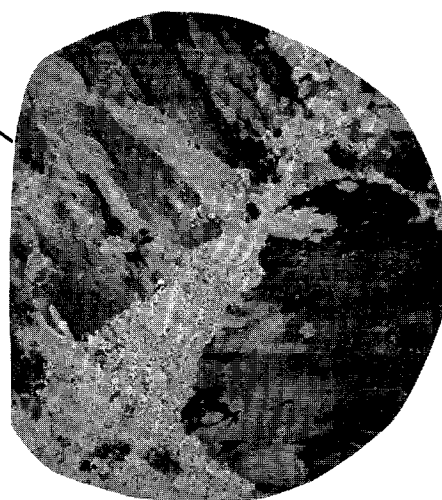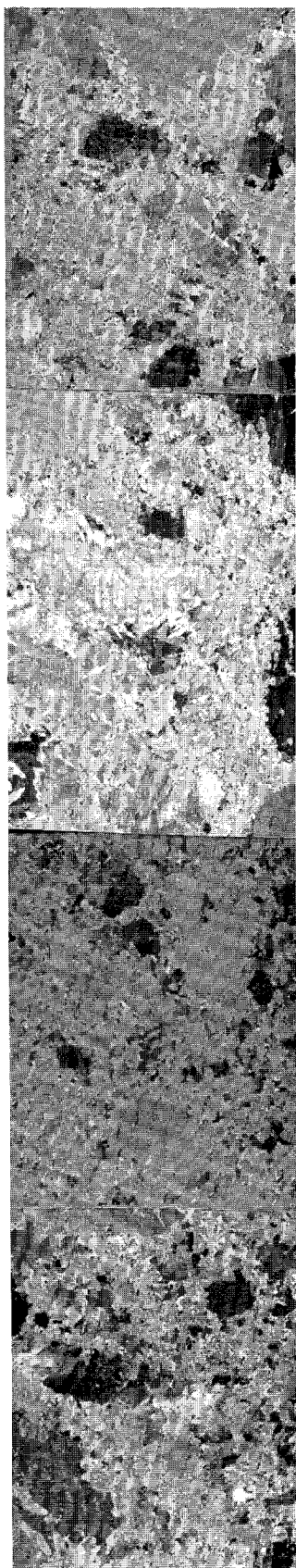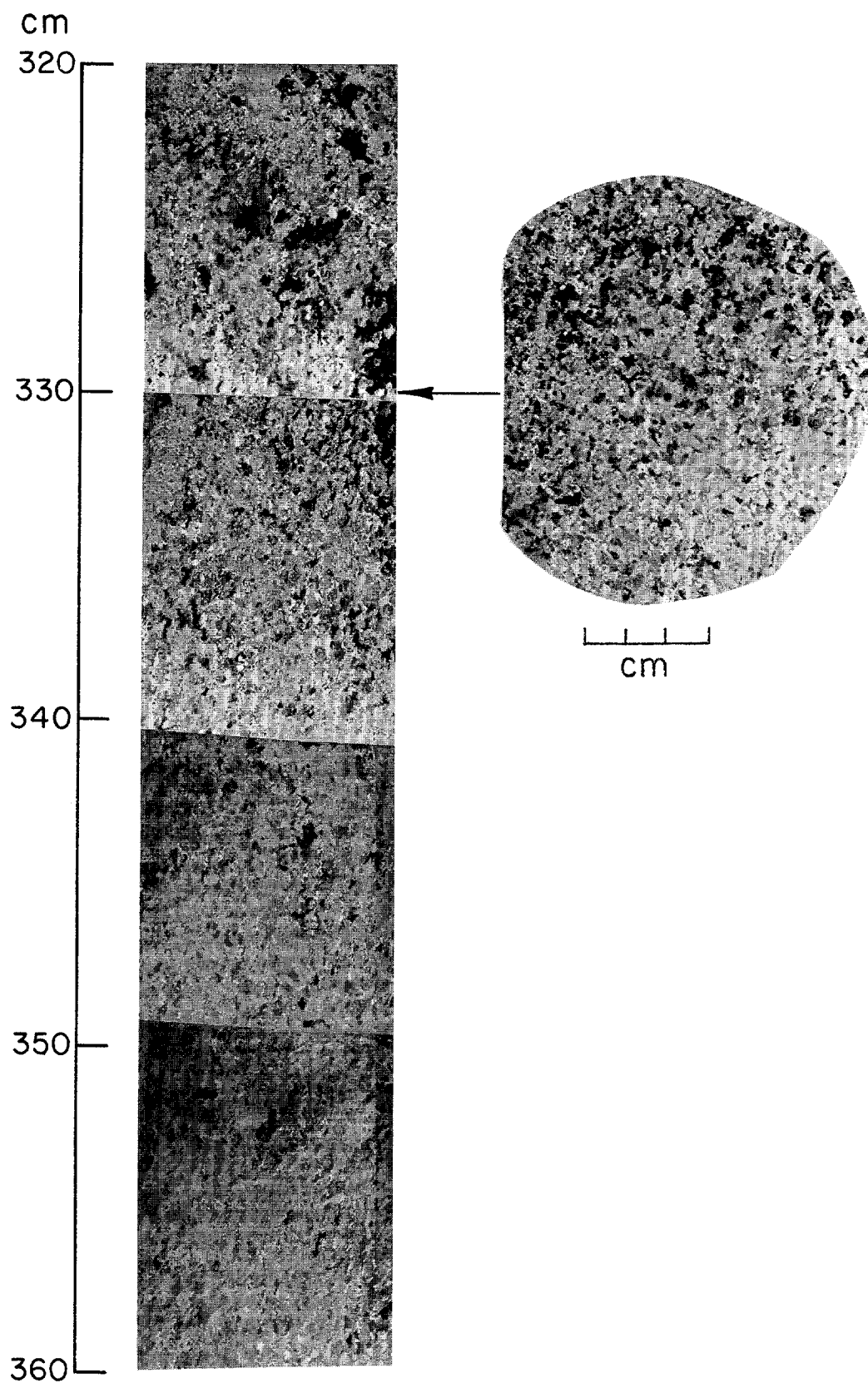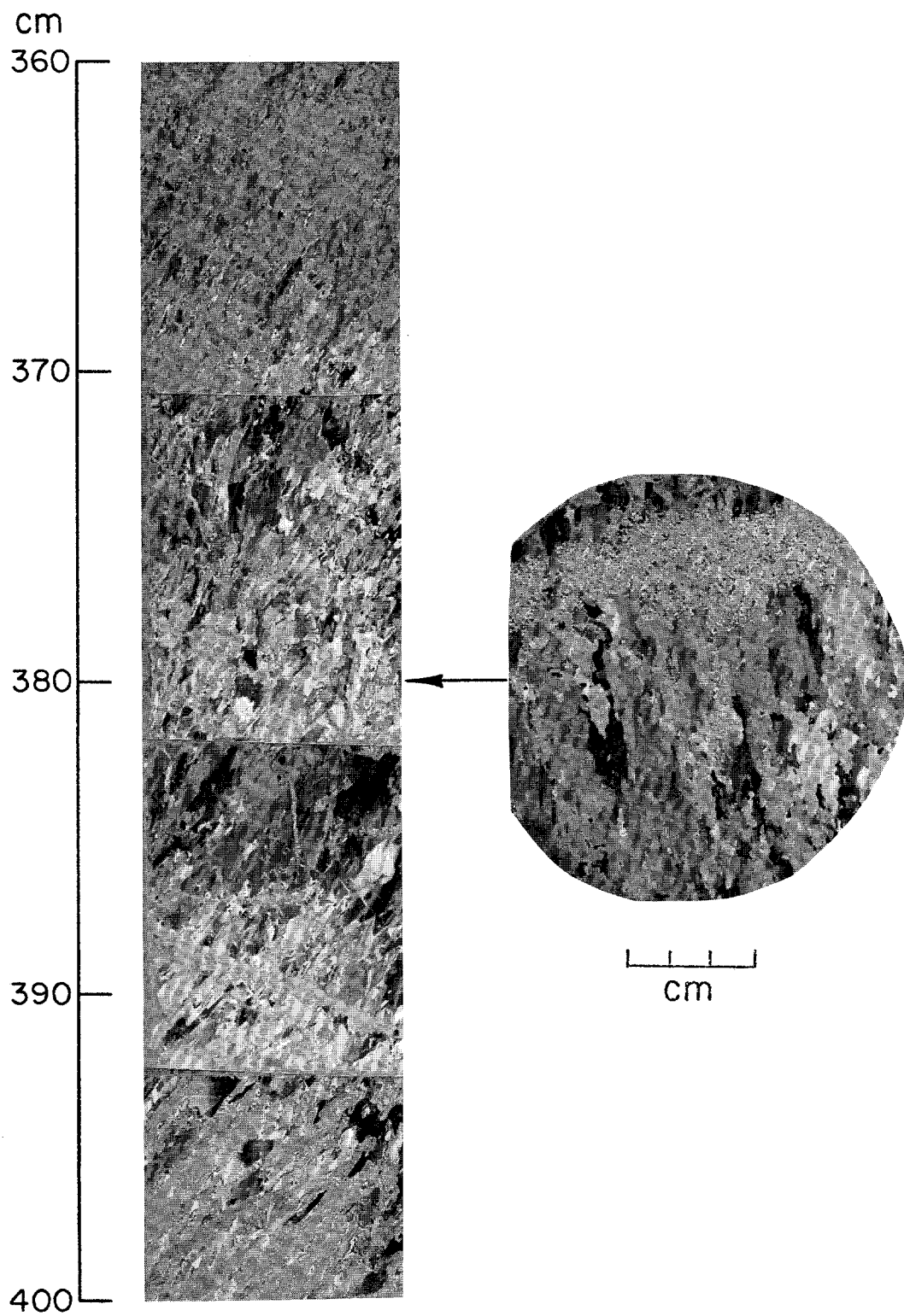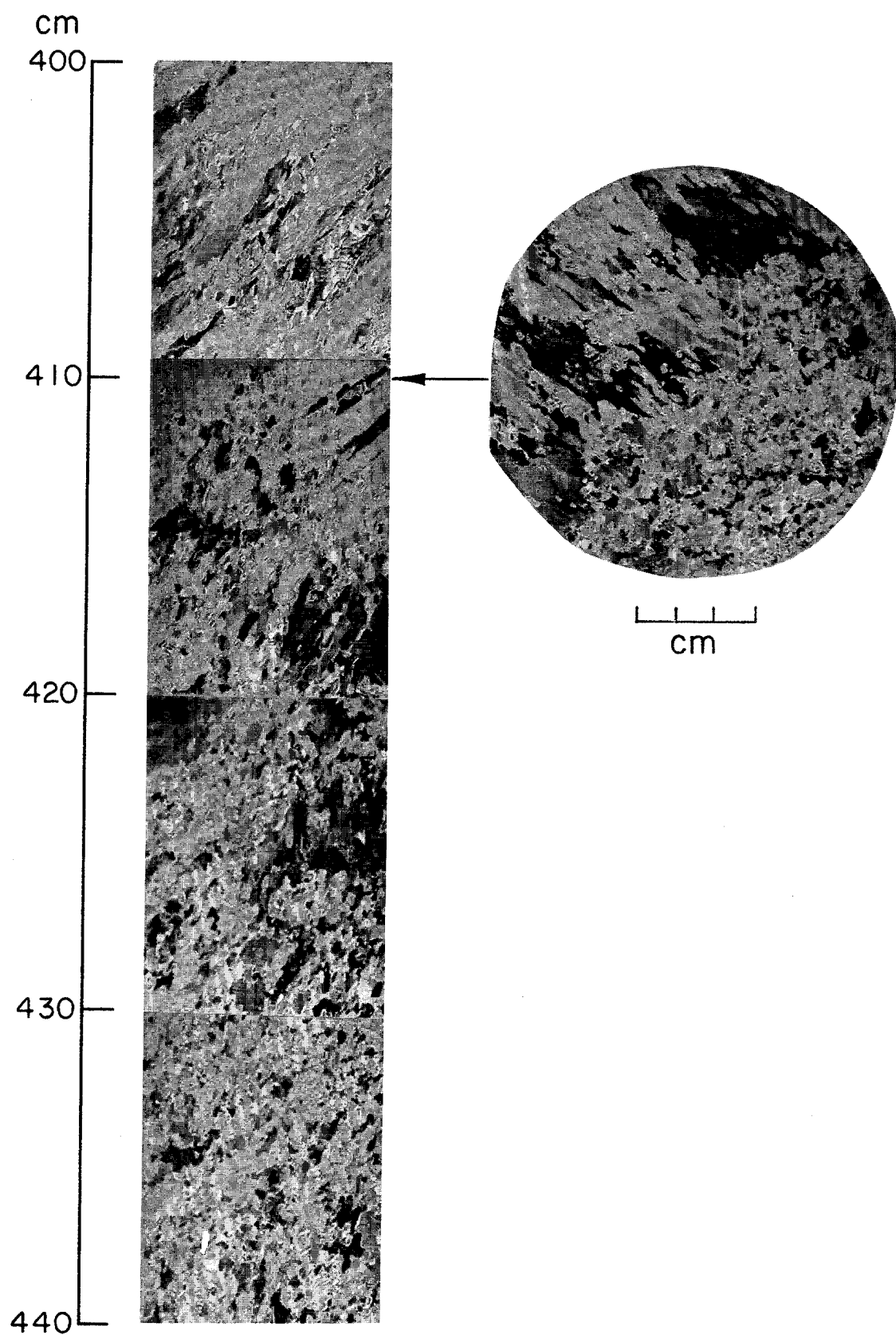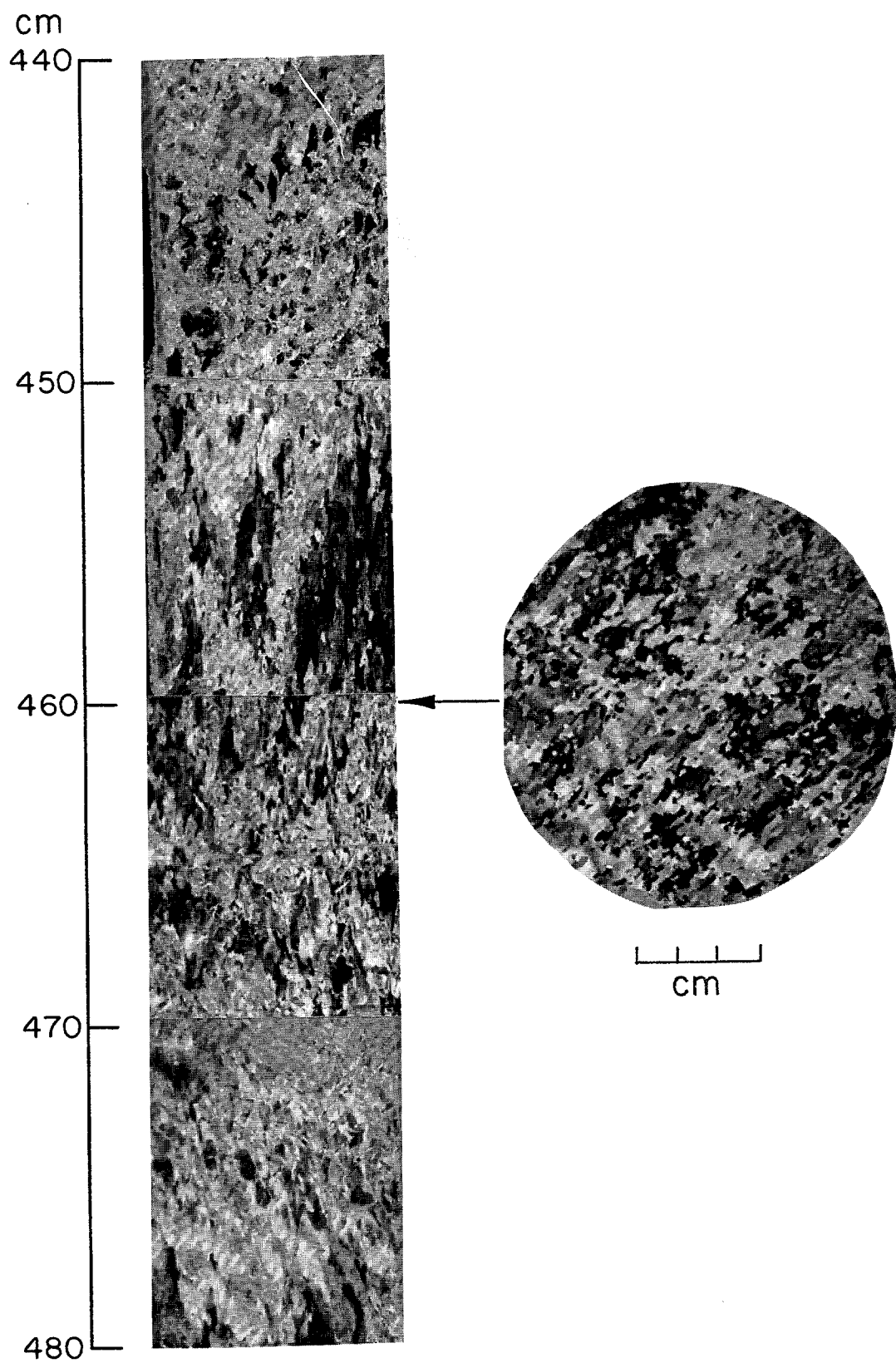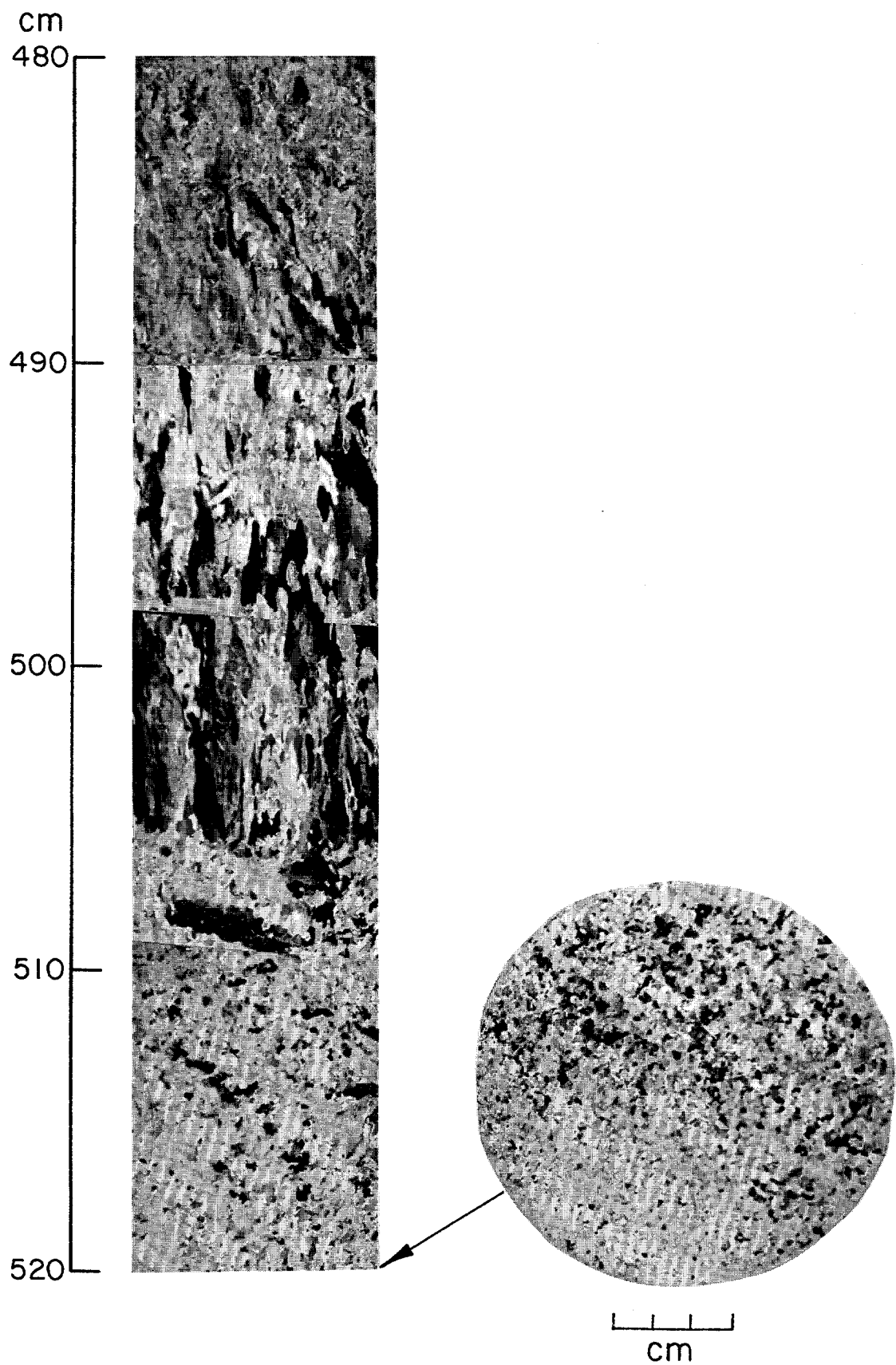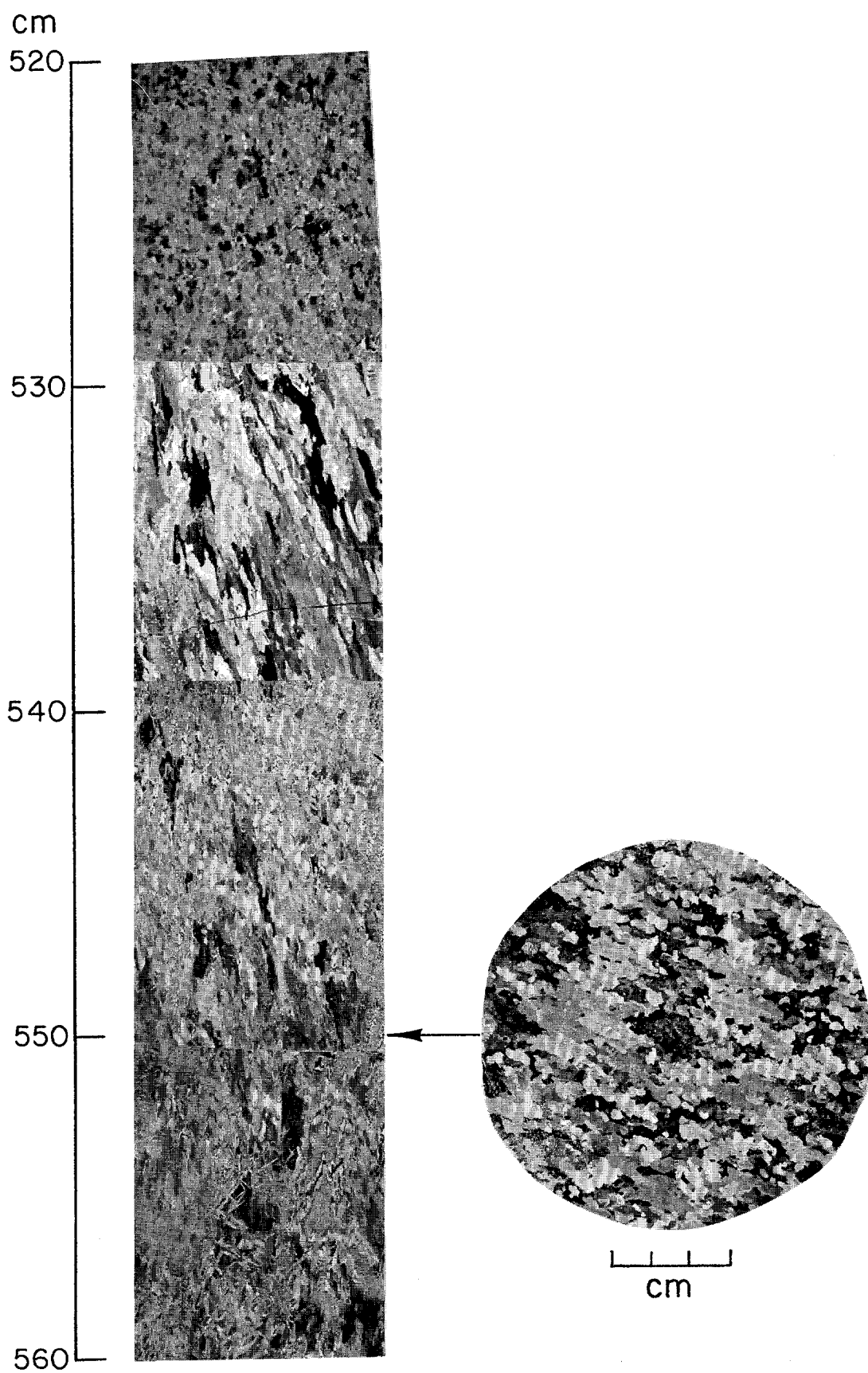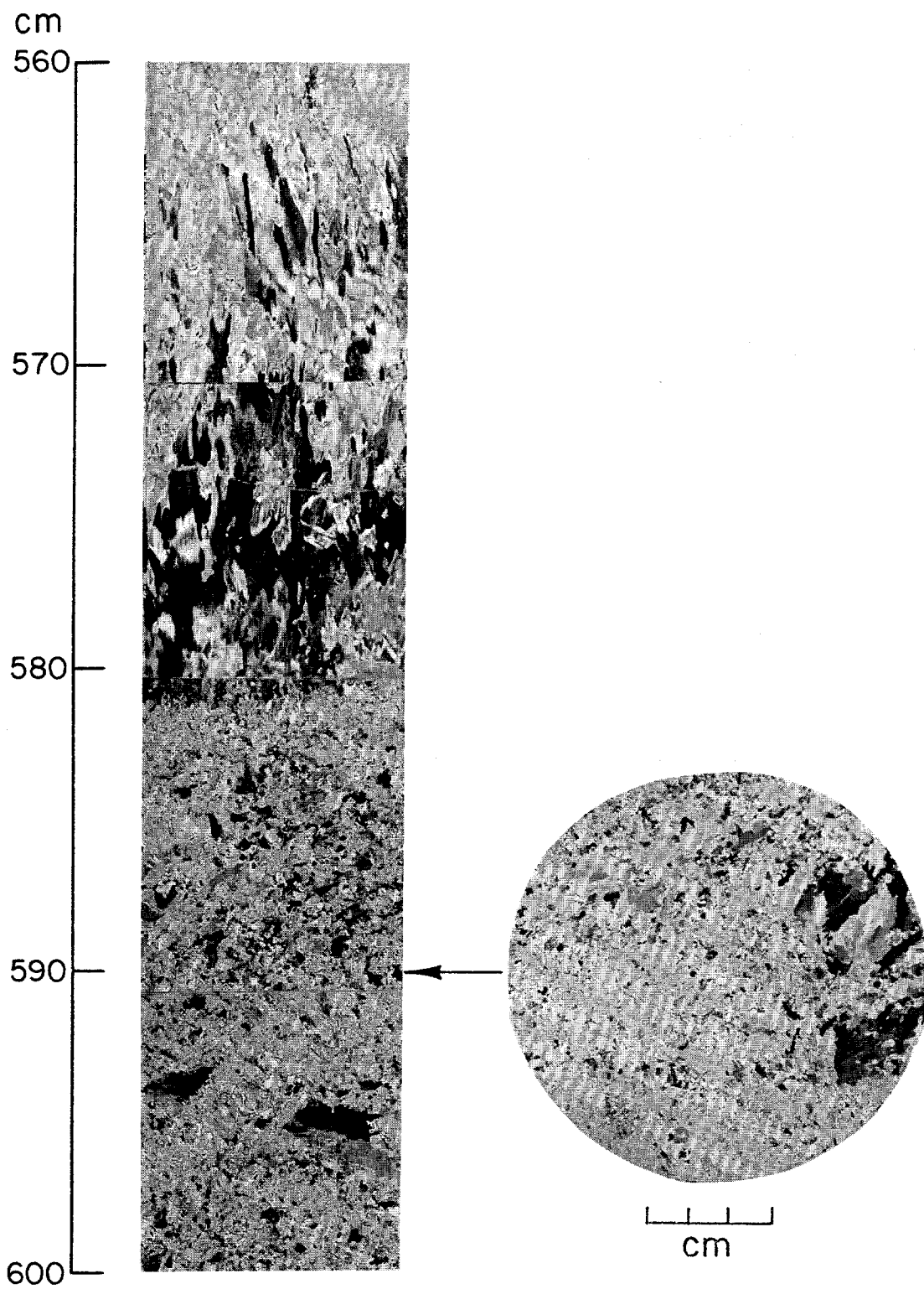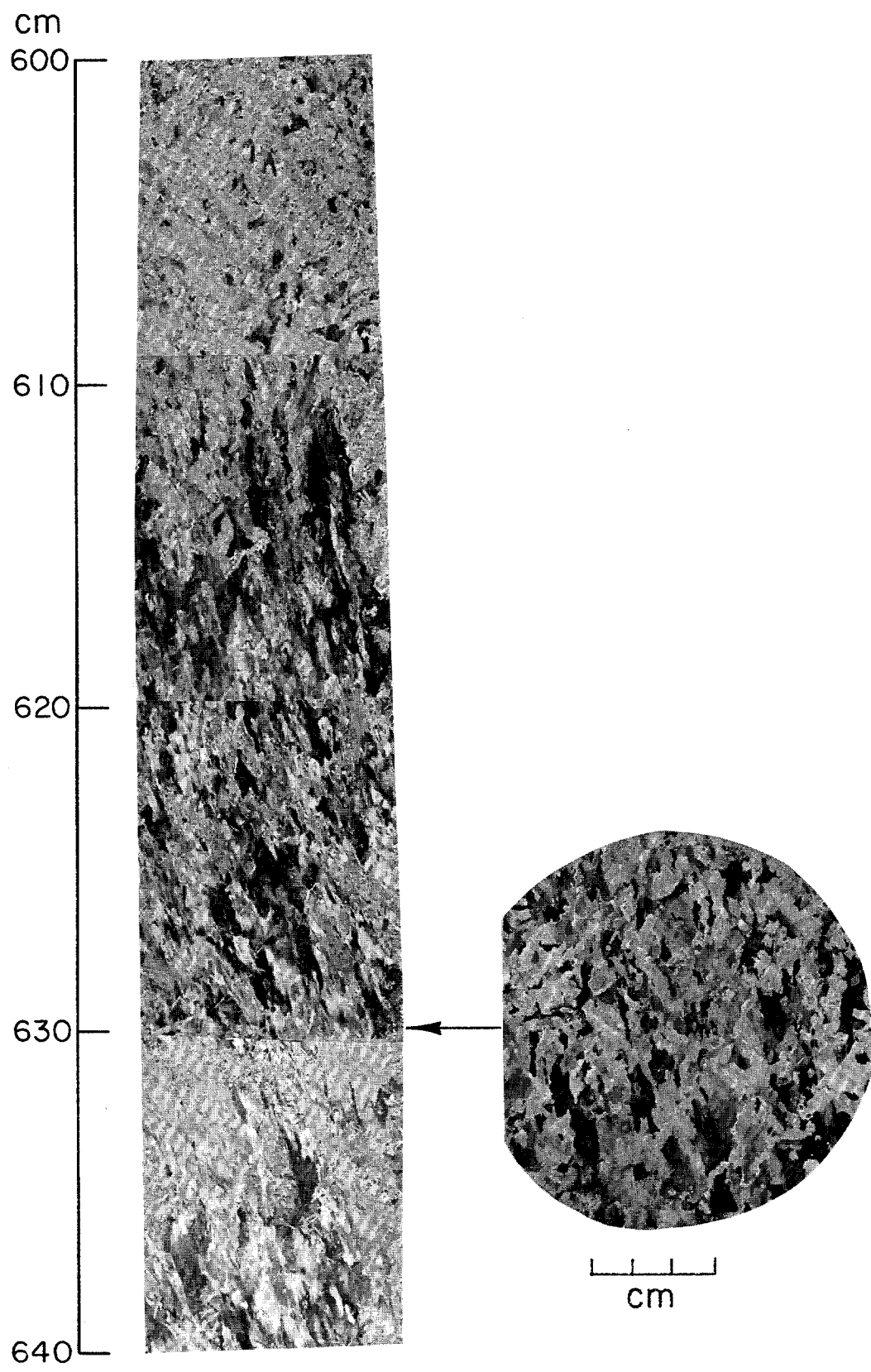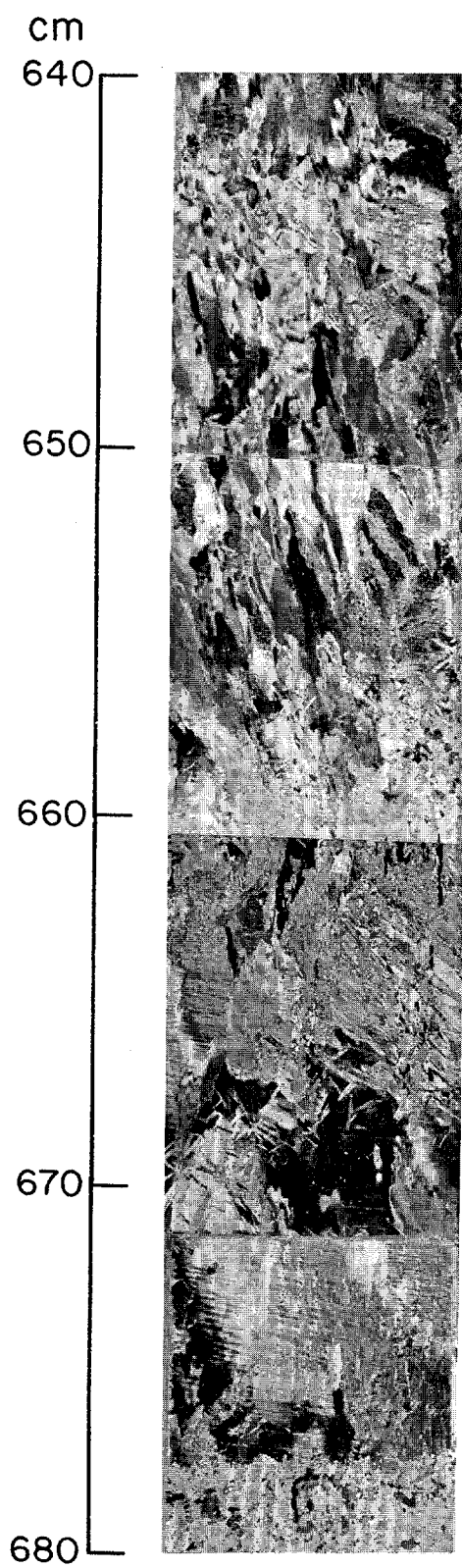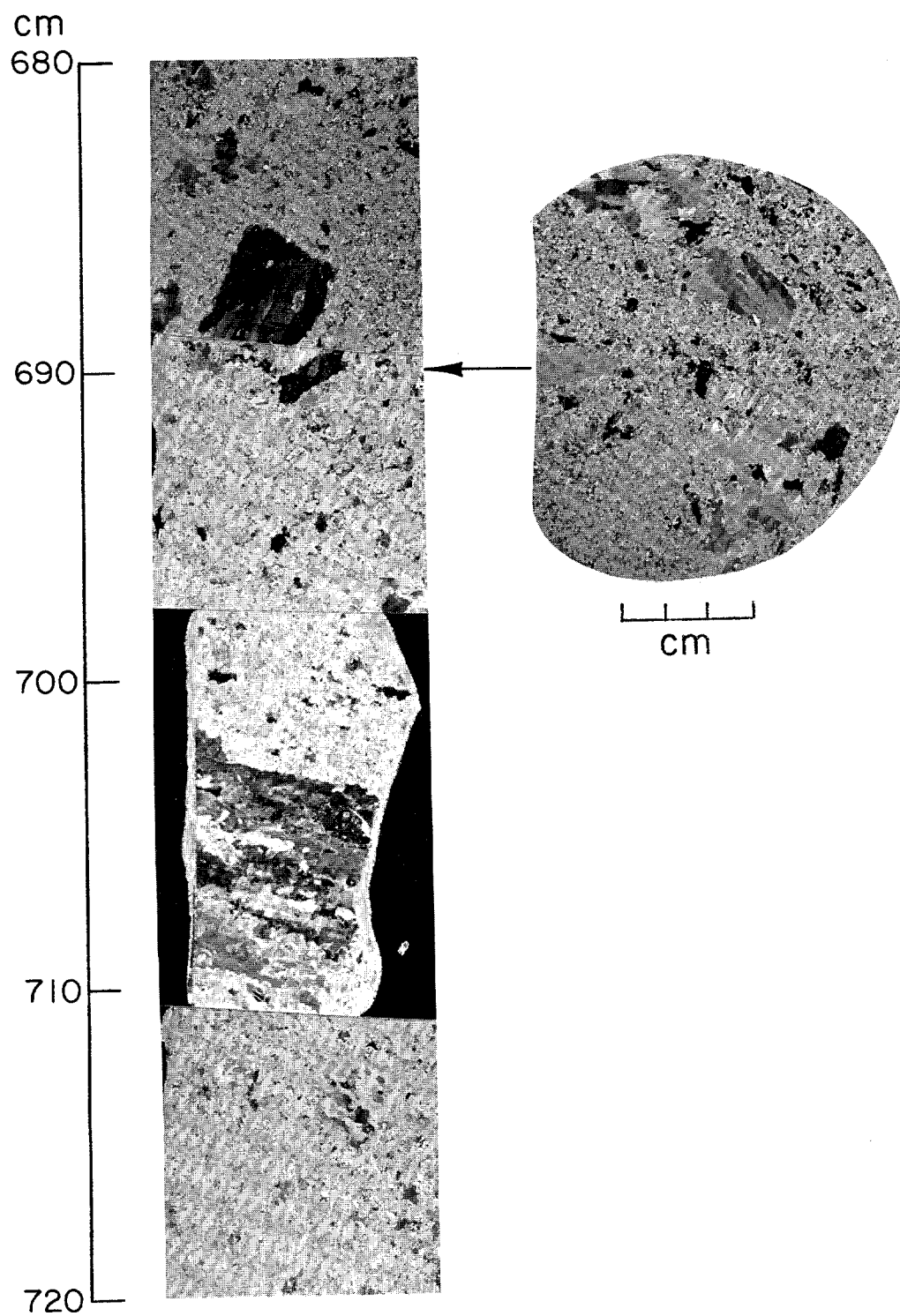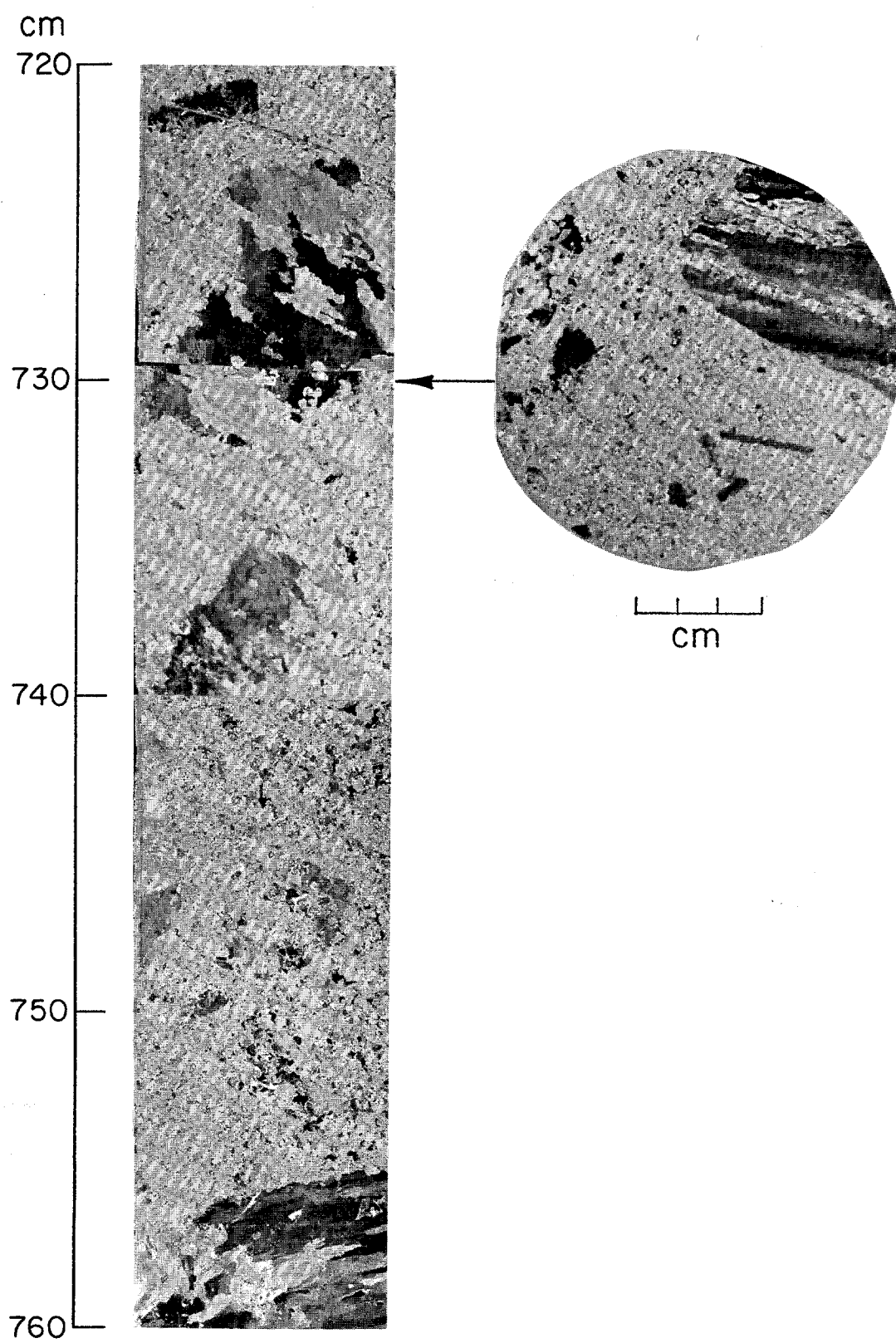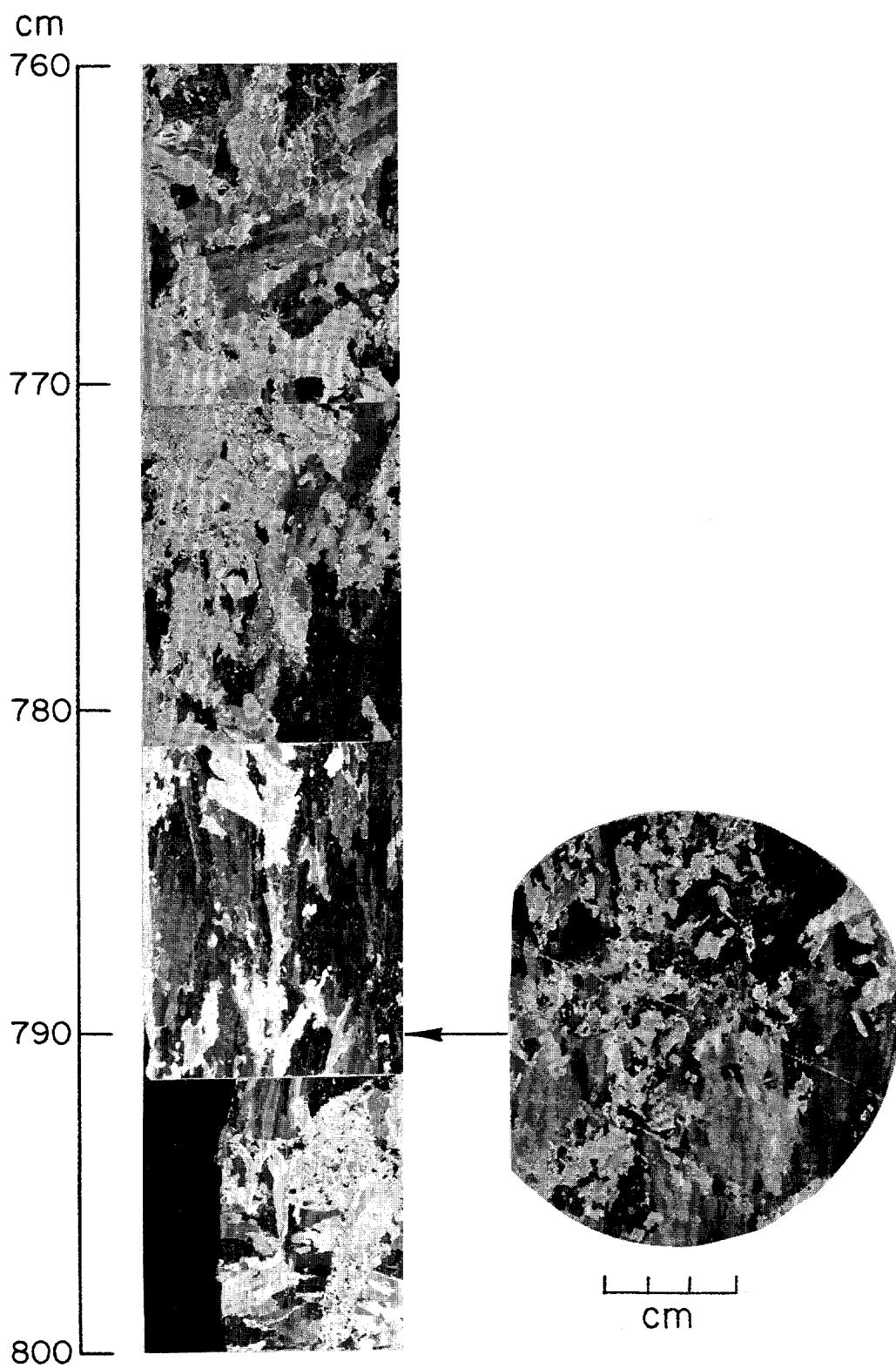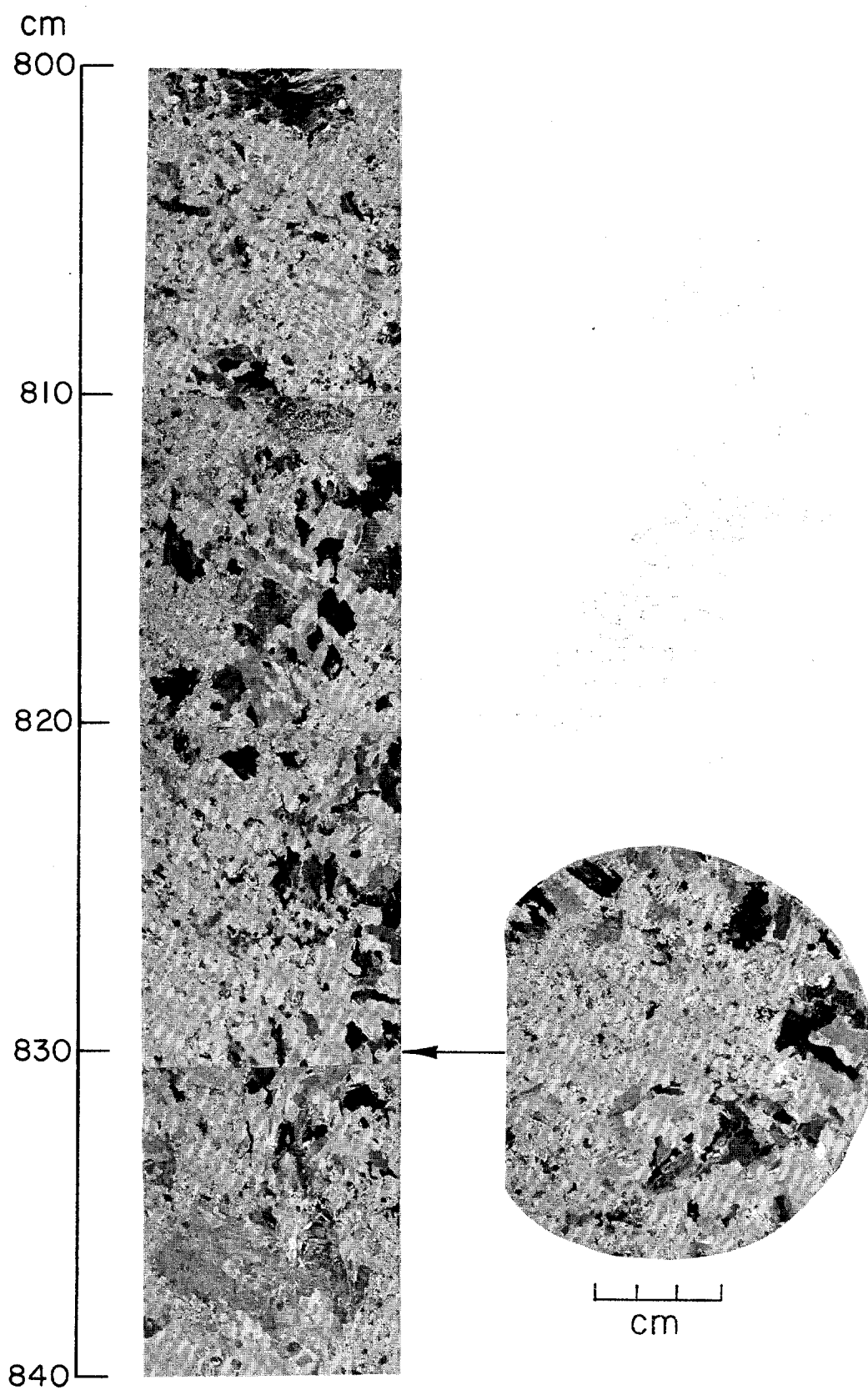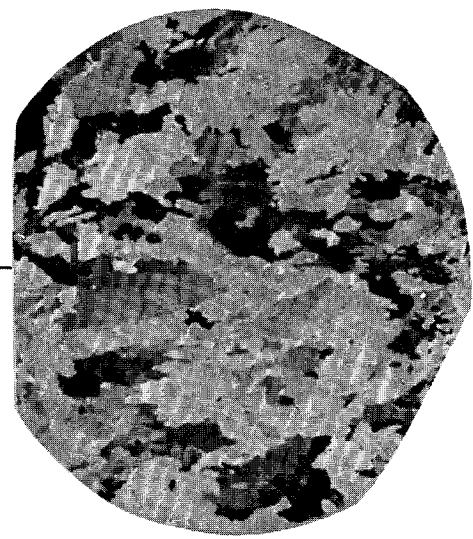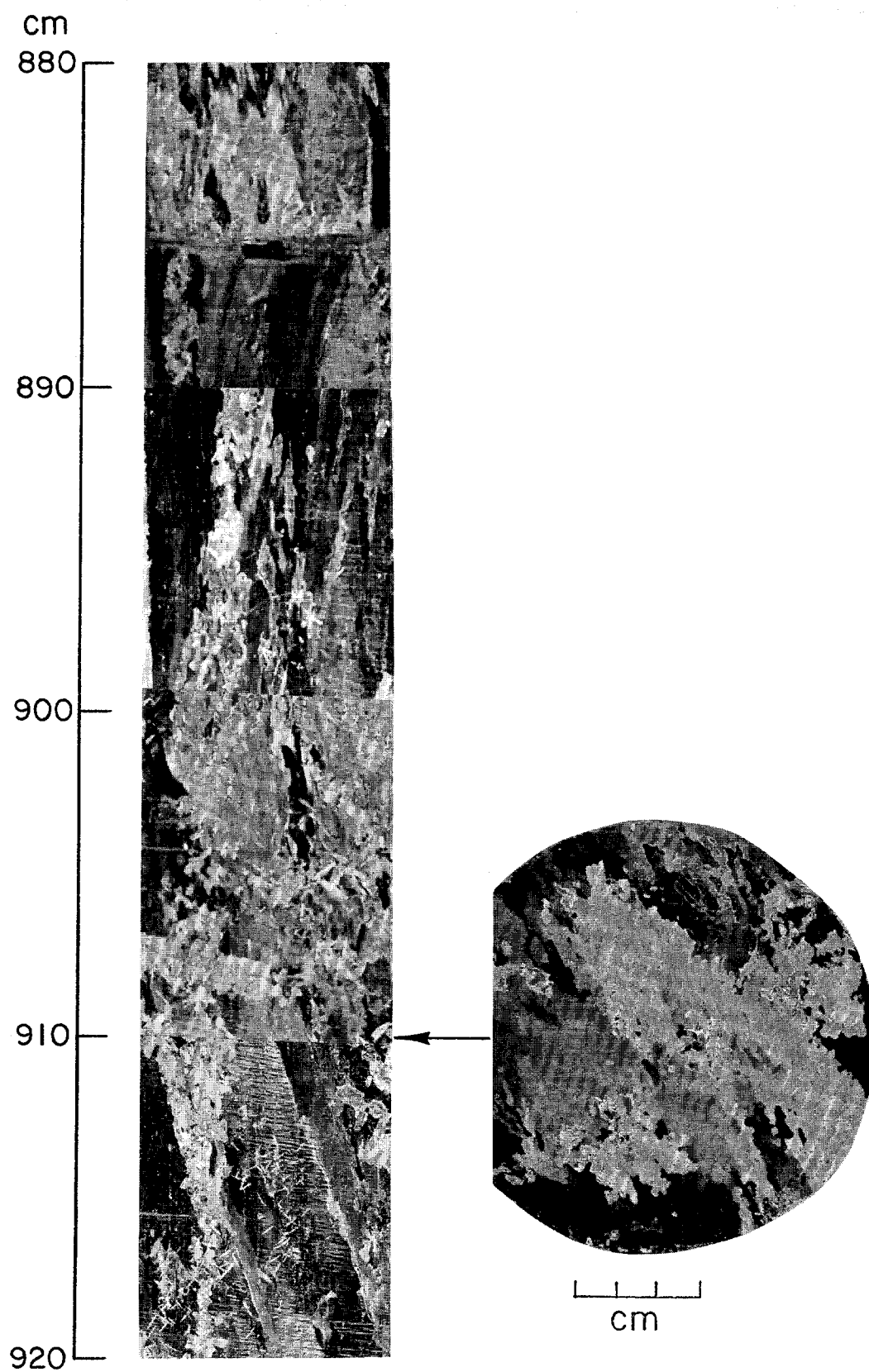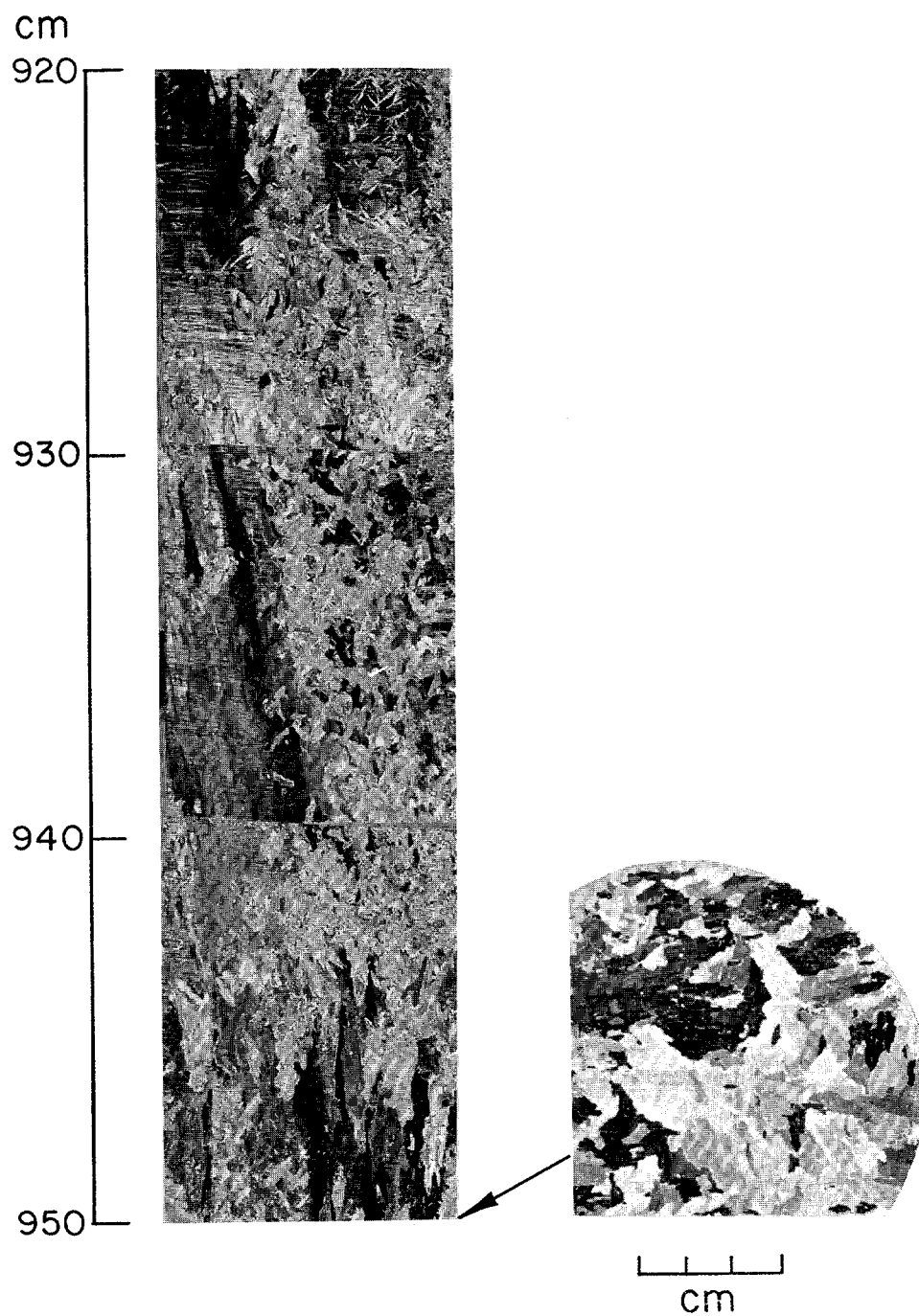
APPENDIX B: TEST DATA

INDEX

Column No.	Symbol	Description
1	σ_m (lb/in.^{2})	Peak stress, or strength
2	ε_m(GL)(%)	Strain at σ_m determined by the DCDTs over a gauge length of 5.5 in. (4.5 in. for tension tests)
3	e_m(FS)(%)	Strain at σ_m determined by the extensometer over the full sample length of 10 in.
4	t_m(S)	Time to peak stress
5	σ_e(psi)	Stress at end of test
6	ε_e(FS)(%)	Full sample strain at end of test
7	t_e(s)	Time to end of test
8	E_i(GL)(10^6 lb/in.^{2})	Initial tangent modulus determined using strains found over the gauge length
9	E_0(GL)(10^6 lb/in.^{2})	Secant modulus determined using gauge length strains
10	E_0(FS)(10^6 lb/in.^{2})	Secant modulus determined using full sample strains
11	S_i(°/oo)	Sample salinity at test temperature
12	ρ(lb/ft^3)	Sample weight density at test temperature
13	V_b(°/oo)	Brine volume at test temperature
14	V_a(°/oo)	Air volume at test temperature
15	n(°/oo)	Porosity at test temperature
16	σ_e/σ_m	Ratio of end to peak stress at 5% full sample strain
17	Ice squareness (in.)	Sample squareness departure after ends are milled
18	End cap squareness (in.)	Sample squareness departure after end caps are mounted
19	Shim (in.)	Amount of shim stock inserted between low end of sample and actuator before testing

Constant-strain-rate compression data

This section contains the results from the constant-strain-rate, uniaxial compression tests. The parameters listed for each test are defined in the Index. The sample number, RC32-133/160V for example, gives the location and depth of the sample, that is, Ridge C, hole 32, at a depth of 133 to 160 cm. V indicates a vertically oriented sample and H a horizontal sample.

Strain rate = 10^{-4} s^{-1}, Temperature = $-5°C$ (23°F)

	01	02	03	04	05	06	07	08	09	10	11	12	13	14	15	16	17	18	19
RC32-133/160V	330	0.150	0.170	16.50	195	5.00	500.0	0.771	0.220	0.194	1.17	53.50	10.8	68.0	78.8	0.591	0.003	0.006	0.006
RC43-150H	386	0.110	0.110	10.60	223	5.00	500.0	0.739	0.351	0.351	0.48	51.62	4.3	99.7	104.0	0.578	0.048	0.010	0.010
RC33-205/232V	478	0.100	0.090	7.80	207	5.00	500.0	0.983	0.478	0.531	3.05	55.18	29.0	41.6	70.6	0.433	0.007	0.005	0.005
RC43-222H	402	0.260	0.270	25.40	203	5.00	500.0	0.871	0.155	0.149	1.82	54.98	17.3	43.1	60.4	0.505	0.090	0.012	0.012
RC46-047/073V	362	0.090	0.080	7.10	131	5.00	500.0	0.807	0.402	0.453	0.92	54.24	8.6	54.6	63.3	0.362	0.009	0.003	0.003
RC44-073H	326	0.090	0.040	5.90	123	5.00	500.0	0.921	0.362	0.815	1.28	53.13	11.7	74.5	86.2	0.377	0.027	0.016	0.016
RC44-060H	227	0.110	0.110	11.70	91	5.00	500.0	0.639	0.206	0.206	1.23	50.69	10.8	116.9	127.7	0.403	0.033	0.000	0.004
RC46-083/110V	800	0.620	0.400	37.70	247	5.00	500.0	1.068	0.129	0.200	2.62	55.12	24.9	41.8	66.7	0.309	0.006	0.005	0.005
RC44-086H	390	0.110	0.090	9.80	95	5.00	500.0	0.999	0.355	0.433	1.85	57.03	18.2	7.6	25.8	0.245	0.035	0.009	0.009
RC46-147/173V	271	0.150	0.120	14.00	115	5.00	500.0	0.846	0.181	0.226	2.99	55.19	28.5	41.2	69.7	0.424	0.006	0.003	0.003
RC44-156H	175	0.060	0.090	5.50	139	5.00	500.0	0.834	0.292	0.194	2.64	55.89	25.5	28.5	54.0	0.794	0.013	0.004	0.004
RC44-256H	271	0.080	0.080	6.60	111	5.00	500.0	0.818	0.339	0.339	2.62	55.74	25.2	31.2	56.4	0.410	0.033	0.015	0.013
RC47-025/053V	322	0.100	0.090	9.00	127	5.00	500.0	0.782	0.322	0.358	1.05	53.25	9.6	72.2	81.8	0.394	0.005	0.011	0.011
RC45-040H	306	0.060	0.080	6.30	111	5.00	500.0	0.671	0.510	0.383	0.30	49.32	2.6	139.6	142.2	0.363	0.045	0.041	0.041
RC47-191/217V	669	0.110	0.070	6.00	163	5.00	500.0	1.144	0.608	0.956	2.83	56.25	27.5	22.7	50.2	0.244	0.007	0.013	0.013
RC44-204H	561	0.160	0.180	16.60	151	5.00	500.0	1.074	0.351	0.312	3.91	57.19	38.6	8.2	46.7	0.269	0.034	0.001	0.001
RC47-275/302V	326	0.170	0.200	18.50	123	5.00	500.0	0.815	0.192	0.163	4.31	56.67	42.1	17.8	59.9	0.377	0.004	0.008	0.008
RC44-288H	366	0.120	0.130	15.00	163	5.00	500.0	0.854	0.305	0.282	2.16	54.43	20.3	53.3	73.5	0.445	0.034	0.015	0.015

Strain rate = 10^{-2} s^{-1}, Temperature = $-5°C$ (23°F)

	01	02	03	04	05	06	07	08	09	10	11	12	13	14	15	16	17	18	19
RA01-262/289	820	0.100	0.120	0.14	820	0.12	0.14	0.709	0.820	0.586	0.43	53.89	4.0	60.1	64.1		0.003	0.007	0.007
RA06-131/158	390	0.050	0.060	0.07	390	0.06	0.07	0.785	0.780	0.650	0.04	48.69	0.3	150.2	150.6		0.010	0.006	0.006
RA06-337/364	621	0.070	0.110	0.11	621	0.11	0.11	0.869	0.887	0.565	1.35	51.74	12.0	98.9	110.9		0.011	0.003	0.003

RC29-112/139

708 0.070 0.030 0.09   708 0.03 0.09 0.992 1.011 2.360 0.85 56.15 8.2   21.3 29.5   0.004 0.010 0.014

RC29-179/206

716 0.080 0.080 0.11   716 0.08 0.11 0.947 0.895 0.895 1.44 55.70 13.8   30.0 43.9   0.010 0.002 0.002

RC29-342/369

470 0.020 0.060 0.08   470 0.06 0.08 0.840 2.350 0.783 2.46 55.00 23.3   43.8 67.1   0.012 0.005 0.005

RC31-125/152

788 0.080 0.110 0.13   788 0.11 0.13 1.000 0.985 0.716 0.39 54.64 3.7   47.0 50.7   0.008 0.011 0.011

RC31-197/224

645 0.070 0.090 0.12   645 0.09 0.12 0.975 0.921 0.717 2.61 55.00 24.8   44.0 68.8   0.005 0.006 0.006

RC31-278/305

931 0.080 0.100 0.12   931 0.10 0.12 0.995 1.164 0.931 1.84 56.92 18.1   9.5 27.5   0.004 0.003 0.003

Strain rate = 10^{-4} s^{-1}, Temperature = $-20°$C ($-4°$F)

01	02	03	04	05	06	07	08	09	10	11	12	13	14	15	16	17	18	19
RC32-231/258V																		
963	0.210	0.280	22.50	485	5.00	500.0	1.233	0.459	0.344	3.76	55.68	12.2	34.0	46.2	0.504	0.002	0.000	0.000
RC43-245H																		
546	0.080	0.100	9.50	167	5.00	500.0	1.159	0.683	0.546	3.07	56.46	10.1	19.8	29.9	0.306	0.042	0.012	0.009
RC32-267/294V																		
661	0.140	0.220	21.10	167	5.00	500.0	1.036	0.472	0.301	3.76	55.92	12.3	22.9	42.1	0.253	0.012	0.010	0.010
RC33-268/295V																		
899	0.140	0.170	13.50	334	1.40	13.50	1.278	0.642	0.529	4.35	57.13	14.5	9.4	24.0		0.010	0.001	0.001
RC43-280H																		
708	0.110	0.100	9.70	143	5.00	500.0	1.490	0.644	0.708	3.39	56.04	11.1	27.4	38.5	0.202	0.033	0.006	0.006
RC32-303/328V																		
573	0.130	0.110	11.70	223	5.00	500.0	0.878	0.441	0.521	1.48	54.09	4.7	59.4	64.1	0.389	0.010	0.005	0.005
RC43-316H																		
342	0.070	0.090	8.20	231	5.00	500.0	1.191	0.489	0.380	3.71	56.63	12.3	17.5	29.8	0.675	0.025	0.027	0.027
RC32-343/369V																		
485	0.170	0.240	23.90	175	5.00	500.0	0.776	0.285	0.202	2.51	52.92	7.8	80.7	88.5	0.361	0.006	0.015	0.015
RC43-357H																		
597	0.140	0.130	14.40	239	5.00	500.0	0.965	0.426	0.459	1.67	54.45	5.3	53.4	58.7	0.400	0.038	0.006	0.006
RC33-242/268V																		
947	0.190	0.190	19.40	700	0.59	61.00	1.287	0.498	0.498	5.01	56.94	16.7	13.4	30.1		0.005	0.005	0.005
RC43-257H																		
541	0.100	0.100	11.00	215	5.00	500.0	1.144	0.541	0.541	3.61	56.92	12.0	12.4	24.4	0.397			0.008
RC33-368/395V																		
939	0.180	0.160	14.20	247	5.00	500.0	1.101	0.522	0.587	4.52	56.20	14.8	25.7	40.6	0.263	0.006	0.004	0.004
RC43-381H																		
867	0.130	0.150	14.30	207	5.00	500.0	1.179	0.667	0.578	0.44	55.74	1.3	29.7	31.0	0.239	0.025	0.003	0.003
RC46-121/147V																		
517	0.100	0.100	10.50	163	5.00	500.0	1.101	0.517	0.517	2.58	53.89	8.1	64.0	72.1	0.315	0.012	0.006	0.006
RC44-128H																		
255	0.080	0.090	9.50	151	5.00	500.0	0.952	0.319	0.283	3.27	56.60	10.8	17.6	28.4	0.592	0.037	0.009	0.009
RC46-173/199V																		
493	0.110	0.120	12.10	175	5.00	500.0	0.873	0.448	0.411	1.70	53.77	5.3	65.1	70.4	0.355	0.009	0.008	0.008
RC44-186H																		
1018	0.130	0.110	12.40	302	5.00	500.0	1.292	0.783	0.926	3.68	56.51	12.1	19.4	31.6	0.297	0.024	0.006	0.006
RC46-276/303V																		
629	0.120	0.120	13.40	223	5.00	500.0	0.952	0.524	0.524	1.02	53.72	3.2	65.5	68.7	0.355	0.006	0.005	0.005
RC44-299H																		
609	0.120	0.120	13.50	269	5.00	500.0	0.900	0.508	0.508	1.60	54.99	5.1	43.8	48.9	0.442	0.058	0.013	0.013
RC47-090/116V																		
1798	0.190	0.210	20.70	1397	0.27	25.70	1.311	0.946	0.856	3.49	55.92	11.4	29.6	41.0		0.026	0.002	0.002
RC44-103H																		
505	0.100	0.080	7.30	195	5.00	500.0	1.101	0.505	0.631	3.09	56.18	10.1	24.7	34.8	0.386	0.032	0.006	0.005

RC44-116H

01	02	03	04	05	06	07	08	09	10	11	12	13	14	15	16	17	18	19
243	0.070	0.070	6.60	111	5.00	500.0	0.921	0.347	0.347	3.31	56.79	11.0	14.3	25.3	0.457	0.010	0.005	0.005

RC47-127/153V

| 1846 | 0.180 | 0.120 | 14.60 | 1846 | 0.12 | 14.60 | 1.406 | 1.026 | 1.538 | 3.28 | 56.16 | 10.8 | 25.2 | 36.0 | | 0.011 | 0.004 | 0.004 |

RC44-141H

| 287 | 0.080 | 0.110 | 9.30 | 135 | 5.00 | 500.0 | 0.896 | 0.359 | 0.261 | 3.54 | 57.35 | 11.9 | 4.7 | 16.6 | 0.470 | 0.040 | 0.003 | 0.003 |

RC47-302/329V

| 875 | 0.110 | 0.100 | 10.00 | 247 | 5.00 | 500.0 | 1.352 | 0.796 | 0.875 | 2.57 | 56.71 | 8.5 | 15.0 | 23.5 | 0.282 | 0.005 | 0.009 | 0.009 |

Strain rate = 10^{-2} s^{-1}, Temperature = −20°C (−4°F)

01	02	03	04	05	06	07	08	09	10	11	12	13	14	15	16	17	18	19

RA01-009/036

| 597 | 0.080 | 0.100 | 0.12 | 597 | 0.10 | 0.12 | 0.765 | 0.746 | 0.597 | 0.01 | 46.95 | 0.0 | 182.4 | 182.4 | | 0.003 | 0.003 | 0.003 |

RA01-078/105

| 1130 | 0.130 | 0.140 | 0.16 | 1130 | 0.14 | 0.16 | 0.887 | 0.869 | 0.807 | 0.02 | 50.14 | 0.1 | 126.9 | 126.9 | | 0.006 | 0.004 | 0.004 |

RA01-339/366

| 1361 | 0.130 | 0.140 | 0.16 | 1361 | 0.14 | 0.16 | 1.068 | 1.047 | 0.972 | 0.63 | 55.42 | 2.0 | 35.5 | 37.5 | | 0.004 | 0.003 | 0.003 |

RA01-428/455

| 1476 | 0.160 | 0.160 | 0.17 | 1476 | 0.16 | 0.17 | 1.024 | 0.923 | 0.923 | 0.98 | 55.68 | 3.2 | 31.3 | 34.5 | | 0.037 | 0.010 | 0.010 |

RA06-058/085

| 971 | 0.090 | 0.120 | 0.13 | 971 | 0.12 | 0.13 | 1.522 | 1.079 | 0.809 | 0.02 | 52.04 | 0.1 | 93.8 | 93.8 | | 0.007 | 0.017 | 0.017 |

RA06-266/293

| 1194 | 0.130 | 0.120 | 0.15 | 1194 | 0.12 | 0.15 | 0.882 | 0.919 | 0.995 | 0.24 | 50.51 | 0.7 | 120.6 | 121.3 | | 0.008 | 0.003 | 0.003 |

RC29-251/278

| 1448 | 0.130 | 0.120 | 0.16 | 1448 | 0.12 | 0.16 | 1.232 | 1.114 | 1.207 | 2.58 | 56.51 | 8.5 | 18.5 | 27.0 | | 0.006 | 0.004 | 0.004 |

RC31-350/377

| 1058 | 0.090 | 0.090 | 0.13 | 1058 | 0.09 | 0.13 | 1.156 | 1.176 | 1.176 | 2.14 | 56.19 | 7.0 | 23.6 | 30.6 | | 0.006 | 0.007 | 0.007 |

RC31-416/443

| 1520 | 0.120 | 0.160 | 0.18 | 1520 | 0.16 | 0.18 | 1.255 | 1.267 | 0.950 | 1.83 | 57.07 | 6.1 | 8.0 | 14.1 | | 0.004 | 0.001 | 0.001 |

Constant-strain-rate tension data

This section contains the results from the constant-strain-rate, uniaxial tension tests. The parameters listed for each test are defined in the Index. Tension sample numbers are defined in the same manner as compression sample numbers.

Strain rate = 10^{-3} s^{-1}, Temperature = −5°C (23°F)

01	02	03	04	05	06	07	08	09	10	11	12	13	14	15	16	17	18	19

RA03-073/100

| 115 | 0.013 | 0.015 | 0.32 | | | | 0.812 | 0.885 | 0.767 | 0.01 | 51.12 | 0.1 | 107.6 | 107.7 | | 0.006 | 0.001 | |

RA07-149/176

| 116 | 0.011 | 0.012 | 0.33 | | | | 1.124 | 1.055 | 0.967 | 0.04 | 52.53 | 0.4 | 83.1 | 83.4 | | 0.015 | 0.005 | |

RA07-263/290

| 71 | 0.008 | 0.009 | 0.26 | | | | 0.943 | 0.891 | 0.792 | 0.57 | 52.94 | 5.2 | 76.7 | 81.9 | | 0.006 | 0.004 | |

RB14-232/259

| 76 | 0.008 | 0.009 | 0.26 | | | | 0.945 | 0.950 | 0.844 | 3.43 | 53.13 | 31.4 | 77.7 | 109.2 | | 0.049 | 0.012 | |

RB14-263/290
120 0.012 0.014 0.33   1.054 1.000 0.857 1.38 54.67 13.0 47.9 60.9   0.009 0.000

RB20-039/066
 60 0.007 0.008 0.23   0.977 0.863 0.755 0.21 50.60 1.8 116.9 118.8   0.006 0.006

RB20-161/188
 91 0.009 0.009 0.27   0.931 1.017 1.017 0.38 53.77 3.5 62.0 65.5   0.010 0.003

RB20-193/220
 84 0.007 0.010 0.25   1.207 1.203 0.842 2.20 55.42 21.0 36.0 57.0   0.004 0.014

RB21-005/032
 69 0.011 0.012 0.27   0.616 0.633 0.580 0.02 40.80 0.1 287.9 288.0   0.026 0.018

Strain rate = 10^{-5} s^{-1}, Temperature = $-5°C$ ($23°F$)

01	02	03	04	05	06	07	08	09	10	11	12	13	14	15	16	17	18	19

RA07-181/208
135 0.018 0.022 21.80   0.913 0.750 0.614 0.05 52.87 0.5 77.2 77.6   0.006 0.007

RA09-036/063
149 0.022 0.026 21.20   1.100 0.677 0.573 0.03 50.85 0.3 112.3 112.6   0.006 0.009

RA09-291/318
138 0.019 0.029 28.60   1.020 0.726 0.476 0.76 56.36 7.4 17.3 24.7   0.006 0.004

RB20-129/156
 94 0.014 0.014 14.00   0.990 0.676 0.676 0.94 53.25 8.6 71.9 80.5   0.006 0.000

RB21-164/191
113 0.020 0.020 19.80   0.889 0.565 0.565 1.63 54.64 15.4 48.8 64.2   0.005 0.006

RB21-196/223
 82 0.019 0.032 32.30   0.887 0.432 0.257 1.99 55.31 19.0 37.5 56.5   0.007 0.009

RB21-257/284
136 0.019 0.026 25.30   0.817 0.716 0.523 1.12 53.96 10.4 59.8 70.2   0.005 0.009

RB22-018/045
 94 0.021 0.025 24.90   0.786 0.451 0.378 0.02 49.33 0.2 138.9 139.1   0.010 0.005

RB22-163/190
130 0.018 0.017 17.00   0.940 0.722 0.765 0.91 53.37 8.4 69.8 78.1   0.005 0.003

Strain rate = 10^{-3} s^{-1}, Temperature = $20°C$ ($-4°F$)

01	02	03	04	05	06	07	08	09	10	11	12	13	14	15	16	17	18	19

RA03-042/069
123 0.012 0.013 0.31   1.039 1.025 0.946 0.02 51.78 0.1 98.2 98.2   0.020 0.008

RA03-127/154
121 0.012 0.014 0.32   0.967 1.008 0.864 0.01 51.53 0.0 102.5 102.6   0.004 0.004

RA09-234/261
 69 0.009 0.009 0.28   0.955 0.767 0.767 0.22 52.37 0.7 88.1 88.8   0.011 0.001

RB14-025/052
 84 0.009 0.010 0.16   1.003 0.936 0.842 0.19 50.00 0.6 129.3 129.9   0.004 0.004

Sample	01	02	03	04	05	06	07	08	09	10	11	12	13	14	15	16	17	18	19
RB14-294/321	133	0.012	0.013	0.31				1.177	1.108	1.023	1.58	55.27	5.1	38.9	44.0		0.012	0.004	
RB20-089/116	134	0.012	0.013	0.32				1.158	1.117	1.031	0.69	53.89	2.2	62.1	64.2		0.010	0.013	
RB20-262/289	92	0.009	0.010	0.27				1.117	1.028	0.925	1.31	54.86	4.2	45.8	50.0		0.006	0.012	
RB21-361/388	124	0.012	0.015	0.32				1.072	1.033	0.827	1.41	54.53	4.5	51.6	56.1		0.006	0.003	
RB22-132/159	104	0.010	0.012	0.31				1.048	1.040	0.867	0.55	54.22	1.7	56.2	57.9		0.006	0.011	

Strain rate $= 10^{-5}$ s^{-1}, Temperature $= -20°C$ ($-4°F$)

Sample	01	02	03	04	05	06	07	08	09	10	11	12	13	14	15	16	17	18	19
RA03-192/219	93	0.010	0.010	9.80				1.134	0.935	0.935	0.03	53.64	0.1	65.8	65.9		0.006	0.005	
RA03-243/270	123	0.014	0.014	14.10				1.011	0.879	0.879	0.51	52.12	1.6	92.7	94.3		0.005	0.001	
RA03-341/368	126	0.014	0.016	15.50				1.069	0.900	0.788	1.41	55.46	4.6	35.4	40.0		0.007	0.002	
RA07-005/032	78	0.014	0.015	14.60				0.604	0.557	0.520	0.01	45.93	0.0	200.1	200.1		0.003	0.010	
RA09-129/156	92	0.011	0.012	12.10				0.967	0.841	0.771	0.08	52.69	0.2	82.4	82.6		0.011	0.007	
RA09-160/187	89	0.012	0.012	12.30				0.788	0.745	0.745	0.01	51.40	0.0	104.8	104.8		0.003	0.003	
RB14-185/212	71	0.009	0.011	10.60				0.919	0.793	0.649	0.47	53.23	1.5	73.3	74.8		0.005	0.003	
RB14-368/395	134	0.022	0.025	24.50				1.039	0.609	0.536	3.16	56.84	10.4	18.4	28.8		0.016	0.007	
RB20-231/258	124	0.012	0.018	15.80				1.006	1.033	0.689	0.97	55.03	3.1	42.5	45.6		0.005	0.008	

Triaxial test data

This section contains the results from the constant strain-rate triaxial tests. The parameters listed for each test are defined in the Index. As no displacement transducers were placed directly on the sample, the initial tangent modulus data given in column 8 are based on the full sample strain. The strain and modulus data are measured values and have not been corrected for deformation of the synthane end caps. Corrected data are given in the text. Triaxial sample numbers are defined in the same manner as compression sample numbers.

Strain rate $= 10^{-3}$ s^{-1}, Temperature $= -5°C$ ($23°F$), $\sigma_r / \sigma_a = 0.5$

Sample	01	02	03	04	05	06	07	08	09	10	11	12	13	14	15	16	17	18	19
RA10-490/517	1830		0.590	5.80	1369	5.00	50.00	0.574		0.310	0.32	53.58	3.0	65.2	68.2	0.748	0.004	0.006	0.006

RA11-233/260

01	02	03	04	05	06	07	08	09	10	11	12	13	14	15	16	17	18	19
1544	0.440	4.20	979	5.00	50.00	0.461			0.351	0.04	52.34	0.4	86.4	86.7	0.634	0.007	0.016	0.016

RB13-286/313

1870	0.410	4.00	1432	5.00	50.00	0.650			0.456	1.34	55.14	12.7	39.5	52.2	0.766	0.010	0.003	0.004

RB16-124/151

1926	0.520	4.70	979	5.00	50.00	0.685			0.370	1.50	53.32	13.8	71.5	85.3	0.508	0.007	0.010	0.010

RB16-262/289

1294	0.350	3.10	1019	5.00	50.00	0.526			0.370	0.95	51.61	8.5	100.4	108.9	0.554	0.012	0.013	0.014

RB17-236/263

1838	0.420	3.90	1424	5.00	50.00	0.601			0.438	0.40	53.13	3.7	73.2	76.8	0.775	0.005	0.006	0.006

RB17-267/294

1584	0.600	5.60	1424	5.00	50.00	0.531			0.264	0.95	55.13	9.0	39.0	48.1	0.899	0.019	0.008	0.008

RB17-399/426

2602	1.010	10.60	1806	5.00	50.00	0.715			0.258	0.62	56.51	6.0	14.5	20.6	0.694	0.016	0.005	0.006

RA10-059/086

788	0.280	2.80	788	5.00	50.00	0.419			0.281	0.02	48.38	0.2	155.5	155.7	1.000	0.025	0.004	0.004

Strain rate = 10^{-5} s^{-1}, Temperature = $-5°C$ (23°F), $\sigma_r/\sigma_a = 0.5$

01	02	03	04	05	06	07	08	09	10	11	12	13	14	15	16	17	18	19

RA10-236/263

>330	>5.000	>5000					0.172			0.09	47.23	0.7	175.6	176.3		0.010	0.008	0.008

RA10-459/486

446	2.810	2810	442	5.00	5000	0.267			0.016	0.29	51.48	2.6	101.7	104.3	0.991	0.004	0.010	0.010

RA10-536/563

895	0.960	960.0	641	5.00	5000	0.297			0.093	0.51	55.76	4.9	27.4	32.3	0.716	0.010	0.010	0.010

RB13-255/282

362	0.650	660.0	350	5.00	5000	0.212			0.056	2.22	55.12	21.1	41.2	62.3	0.967	0.004	0.004	0.004

RB16-230/257

489	0.730	730.0	430	5.00	5000	0.209			0.067	1.43	53.11	13.1	75.1	88.2	0.879	0.005	0.004	0.004

RB16-330/357

350	0.910	910.0	330	5.00	5000	0.362			0.038	1.15	54.69	10.8	47.2	58.0	0.943	0.006	0.006	0.006

RB17-367/394

577	0.900	910.0	525	5.00	5000	0.287			0.064	1.31	56.42	11.0	16.9	27.9	0.910	0.011	0.009	0.010

RB17-443/470

959	0.520	540.0	625	5.00	5000	0.436			0.184	1.04	56.62	10.1	15.0	25.2	0.652	0.034	0.014	0.014

RA10-372/399

557	1.320	1340	485	5.00	5000	0.339			0.042	0.09	45.66	0.7	203.1	203.8	0.871	0.006	0.006	0.006

Strain rate = 10^{-5} s^{-1}, Temperature = $-5°C$ (23°F), $\sigma_r/\sigma_a = 0.25$

01	02	03	04	05	06	07	08	09	10	11	12	13	14	15	16	17	18	19

RA08-134/161

460	0.940	930.0	360	5.00	5000				0.049	0.03	51.12	0.3	107.6	107.9	0.783	0.009	0.000	0.000

	01	02	03	04	05	06	07	08	09	10	11	12	13	14	15	16	17	18	19
RA08-166/193	427	0.790	750.0	310	5.00	5000	0.707			0.054	0.04	52.77	0.4	78.9	79.3	0.726	0.004	0.003	0.004
RA08-198/225	366	0.920	940.0	326	5.00	5000	0.168			0.040	0.16	51.22	1.4	106.1	107.5	0.891	0.009	0.007	0.008
RA08-259/286	515	0.580	590.0	334	5.00	5000	0.408			0.089	0.80	52.65	7.3	82.1	89.4	0.649	0.003	0.006	0.006
RB12-077/104	166	0.360	342.0	165	5.00	5000	0.217			0.046	1.24	54.60	11.7	48.9	60.6	0.994	0.004	0.004	0.004
RB12-163/190	555	1.000	999.0	377	5.00	5000	0.309			0.056	0.12	53.34	1.1	69.1	70.2	0.679	0.008	0.002	0.002
RB12-194/221	549	1.000	999.0	376	5.00	5000	0.245			0.055	0.33	53.75	3.1	62.3	65.3	0.685	0.009	0.009	0.010
RB13-066/093	286	0.450	444.0	230	5.00	5000	0.179			0.064	1.03	54.05	9.6	58.1	67.7	0.804	0.009	0.016	0.016
RB13-097/124	253	0.390	390.0	201	5.00	5000	0.194			0.065	1.21	53.73	11.2	64.0	75.2	0.794	0.010	0.006	0.006
RA08-290/317	573	0.790	820.0	402	5.00	5000	0.291			0.073	0.79	54.10	7.4	56.9	64.3	0.702	0.011	0.007	0.008

Strain rate = 10^{-3} s^{-1}, Temperature = $-20°C$ ($-4°F$), $\sigma_r/\sigma_a = 0.25$

	01	02	03	04	05	06	07	08	09	10	11	12	13	14	15	16	17	18	19
RA08-025/052	2125	0.610	6.00	1114	5.00	50.00	0.482			0.348	0.02	50.07	0.1	128.0	128.0	0.524	0.004	0.002	0.002
RA08-340/367	2467	0.700	7.20	995	5.00	50.00	0.334			0.352	1.10	56.46	3.6	17.7	21.4	0.403	0.031	0.012	0.012
RA11-078/105	1679	0.460	4.60	1679	0.46	4.60	0.428			0.365	0.02	50.95	0.1	112.6	112.7		0.006	0.002	0.002
RA11-127/154	1822	0.470	4.80	740	5.00	50.00	0.470			0.388	0.03	49.36	0.1	140.3	140.4	0.406	0.010	0.004	0.004
RB12-132/159	2475	0.650	6.40	1066	5.00	50.00	0.555			0.381	0.23	52.60	0.7	84.1	84.8	0.431	0.007	0.003	0.004
RB12-326/353	2157	0.610	6.30	1027	5.00	50.00	0.297			0.354	1.28	54.89	4.1	45.2	49.3	0.476	0.006	0.004	0.004
RB12-047/074	1974	0.610	6.10	788	5.00	50.00	0.546			0.324	0.81	53.36	2.5	71.4	73.9	0.399	0.003	0.006	0.006
RB12-239/266	2236	0.580	5.70	931	5.00	50.00	0.589			0.386	1.70	55.39	5.5	36.9	42.4	0.416	0.007	0.004	0.004
RB13-156/183	2332	0.690	6.90	1027	5.00	50.00	0.536			0.338	1.58	55.48	5.1	35.3	40.4	0.440	0.007	0.005	0.006

Strain rate = 10^{-5} s^{-1}, Temperature = $-20°C$ ($-4°F$), $\sigma_r/\sigma_a = 0.5$

Specimen	01	02	03	04	05	06	07	08	09	10	11	12	13	14	15	16	17	18	19
RA10-90/117	>740		>5.000	>5000				0.303			0.03	50.33	0.1	123.4	123.5		0.004	0.007	0.008
RA10-133/160	851		1.520	1530	851	5.00	5000	0.479		0.056	0.03	50.94	0.1	112.8	112.9	1.000	0.000	0.005	0.006
RA11-266/293	1039		0.700	710.0	772	5.00	5000	0.297		0.148	0.04	51.92	0.1	95.8	95.9	0.743	0.007	0.006	0.006
RB16-156/183	>573		>5.000	>5000				0.282			1.96	50.55	5.8	121.3	127.1		0.005	0.010	0.010
RB16-188/215	820		1.010	1030	820	5.00	5000	0.300		0.081	0.66	51.88	2.0	97.0	99.0	1.000	0.006	0.022	0.022
RB16-361/388	971		0.780	750.0	812	5.00	5000	0.318		0.124	1.00	55.71	3.3	30.7	33.9	0.836	0.025	0.004	0.004
RB16-432/459	1600		0.680	670.0	947	5.00	5000	0.452		0.235	1.47	56.53	4.9	16.9	21.7	0.592	0.015	0.010	0.010
RB17-191/218	963		1.390	1380	939	5.00	5000	0.386		0.069	0.53	53.11	1.6	75.5	77.1	0.975	0.007	0.013	0.014
RB17-335/362	1050		1.100	1110	955	5.00	5000	0.391		0.095	1.83	54.96	5.9	44.5	50.4	0.910	0.008	0.005	0.006

Strain rate = 10^{-3} s^{-1}, Temperature = $-20°C$ ($-4°F$), $\sigma_r/\sigma_a = 0.5$

Specimen	01	02	03	04	05	06	07	08	09	10	11	12	13	14	15	16	17	18	19
RA10-194/221	2674		0.610	5.40	1942	5.00	50.00	0.830		0.438	0.02	51.77	0.1	98.4	98.4	0.700	0.002	0.004	0.004
RA10-341/368	2578		0.790	7.80	1958	5.00	50.00	0.689		0.326	0.11	51.48	0.3	103.5	103.8	0.760	0.011	0.003	0.004
RA10-567/594	4011		0.880	8.50	2196	5.00	50.00	1.021		0.456	0.83	56.43	2.7	18.0	20.7	0.547	0.007	0.003	0.004
RB13-225/252	3008		0.680	6.60	1448	5.00	50.00	0.901		0.442	2.22	55.25	7.2	39.9	47.0	0.481	0.004	0.004	0.010
RB13-342/369	4584		1.000	9.40	2992	5.00	50.00	0.936		0.458	1.65	55.60	5.4	33.2	38.6	0.653	0.004	0.004	0.004
RB16-089/116	3374		0.490	4.50	3374	0.49	4.50	0.838		0.689	0.29	52.55	0.9	85.0	89.9		0.006	0.004	0.004
RB16-392/419	3629		0.910	9.00	1974	5.00	50.00	0.860		0.399	1.78	56.22	5.8	22.6	28.4	0.544	0.007	0.010	0.010
RB17-052/079	1210		0.210	2.00	1210	0.21	2.00	0.639		0.576	0.14	53.71	0.4	64.7	65.1		0.007	0.002	0.002
RB18-363/390	5602		1.200	12.00	2929	5.00	50.00	1.000		0.467	0.55	56.60	1.8	14.8	16.6	0.523	0.005	0.005	0.006

Constant-load compression data

This section contains the results from the constant-load compression tests. Most variables have been defined in the Index, with the following exceptions: σ is the applied stress on the sample, $\dot{\varepsilon}_{min}$ (FS) is the strain-rate minimum determined from the full sample displacement; ε_f (FS) is the full sample strain at the strain-rate minimum or failure, t_f is the time to failure, and $\dot{\varepsilon}_e$ (FS) is the full sample strain rate at the end of the test.

CONSTANT LOAD COMPRESSION TEST DATA

Sample No.	σ (lbf/in.²)	T (°F)	$\dot{\varepsilon}_{min}$ (FS) (s⁻¹)	ε_f (FS) (%)	t_f (s)	$\dot{\varepsilon}_e$ (FS) (s⁻¹)	ε_e (FS) (%)	t_e (sec)	S_i (°/oo)	ρ (lb/ft³)	V_b (°/oo)	V_a (°/oo)	n (°/oo)	ISQ. (in.)	ESQ (in.)
BELLOFRAM TESTS															
RC31-473/500	100	23	8.47×10^{-8}	0.70	6.39×10^4	1.46×10^{-7}	2.10	3.33×10^5	1.94	56.87	19.0	10.5	29.6	0.012	0.005
RA02-036/063	100	23	1.65×10^{-7}	1.28	6.31×10^4	2.40×10^{-7}	4.35	2.20×10^5	0.01	49.89	0.1	129.2	129.3	0.004	0.003
RA02-086/113	100	23	1.47×10^{-8}	0.18	7.50×10^4	2.22×10^{-8}	1.15	5.69×10^5	0.02	51.45	0.2	102.0	102.2	0.005	0.000
RC28-158/185	100	23	4.45×10^{-8}	0.51	1.01×10^5	7.46×10^{-8}	2.75	5.13×10^5	0.79	55.12	7.5	39.1	46.6	0.003	0.009
RA06-368/395	100	23	7.78×10^{-8}	0.65	6.53×10^4	1.60×10^{-7}	2.64	2.42×10^5	1.22	53.26	11.2	72.3	83.5	0.004	0.011
RA02-268/295	100	23	6.31×10^{-8}	0.47	6.36×10^4	1.51×10^{-7}	4.85	5.81×10^5	0.26	54.07	2.4	56.7	59.1	0.003	0.005
RC31-383/410	100	23	2.77×10^{-8}	0.69	2.03×10^5	3.68×10^{-8}	2.10	6.67×10^5	1.69	56.62	16.5	14.5	31.0	0.005	0.007
RA01-047/074	100	23	9.12×10^{-7}	0.77	6.59×10^3	1.07×10^{-6}	2.82	2.75×10^4	0.02	48.52	0.2	153.1	153.3	0.007	0.003
RC28-322/351	100	23	6.70×10^{-8}	0.74	8.31×10^4	2.95×10^{-7}	6.57	4.92×10^5	1.51	55.12	14.4	40.2	54.6	0.008	0.004
MTS TESTS															
RC31-309/336	300	23	8.72×10^{-6}	0.45	3.02×10^2	1.65×10^{-4}	5.00	1.78×10^3	1.42	56.62	13.9	14.0	27.9	0.003	0.005
RC31-537/564	300	23	1.15×10^{-4}	0.55	4.22×10^1	1.40×10^{-3}	5.00	1.71×10^2	3.72	56.43	36.2	21.0	57.2	0.025	0.027
RC29-374/401	300	23	7.59×10^{-5}	0.22	1.59×10^1	1.15×10^{-3}	5.00	1.43×10^2	4.67	55.56	44.8	37.6	82.4	0.009	0.009
RC29-455/482	300	23	1.66×10^{-4}	0.20	8.29	2.08×10^{-3}	5.00	1.23×10^2	2.93	56.12	28.4	25.1	53.5	0.009	0.003
RC28-190/217	300	23	9.12×10^{-6}	0.49	3.98×10^2	2.09×10^{-4}	5.00	1.61×10^3	0.46	53.26	4.2	71.2	75.4	0.002	0.004
RC28-126/153	300	23	3.63×10^{-6}	0.64	9.12×10^2	1.09×10^{-5}	5.00	6.16×10^3	0.48	54.81	4.5	44.0	48.6	0.008	0.008
RA01-370/397	300	23	3.29×10^{-6}	0.80	1.68×10^3	8.96×10^{-6}	5.00	1.00×10^4	0.89	56.12	8.6	21.9	30.5	0.008	0.003
RA02-339/366	300	23	7.94×10^{-6}	0.55	3.31×10^2	7.94×10^{-5}	5.00	1.97×10^3	1.71	55.56	16.4	32.9	49.3	0.005	0.012
RC29-406/433	300	-4	3.03×10^{-5}	0.07	1.82×10^1	4.67×10^{-4}	5.00	3.29×10^2	3.87	56.12	12.7	26.4	39.1	0.003	0.005
RA06-432/459	300	-4	3.77×10^{-6}	0.35	6.65×10^2	1.60×10^{-6}	5.00	3.00×10^3	1.09	55.19	3.5	40.0	43.5	0.006	0.007
RC31-166/193	300	-4	1.20×10^{-6}	0.72	3.55×10^3	3.47×10^{-6}	3.94	1.89×10^4	0.70	55.06	2.3	41.8	44.0	0.008	0.005
RC29-148/175	300	-4	3.98×10^{-7}	0.38	3.98×10^3	3.09×10^{-7}	1.33	3.45×10^4	1.19	56.62	3.9	15.1	19.0	0.012	0.008
RA06-162/189	300	-4	2.09×10^{-5}	0.05	7.94	1.11×10^{-3}	5.00	3.30×10^2	0.10	50.63	0.3	118.4	118.7	0.004	0.011
RC31-247/274	300	-4	4.79×10^{-6}	0.17	2.63×10^2	1.85×10^{-4}	5.00	1.34×10^3	0.77	56.69	2.5	13.6	16.1	0.007	0.005
RA06-089/116	300	-4	2.01×10^{-6}	1.03	3.16×10^3	2.31×10^{-6}	4.20	1.59×10^4	0.03	50.38	0.1	122.7	122.8	0.004	0.008
RA06-463/490	300	-4	1.28×10^{-6}	0.83	4.57×10^3	1.51×10^{-6}	2.24	1.59×10^4	0.73	55.38	2.4	36.4	38.7	0.006	0.004
RC28-251/278	300	-4	7.4×10^{-7}	0.56	4.79×10^3	1.11×10^{-6}	1.17	1.18×10^4	2.58	56.50	8.5	18.6	27.2	0.009	0.008
RC31-089/116	600	-4	9.52×10^{-5}	0.13	6.75	3.11×10^{-3}	4.23	6.98×10^1	0.45	55.87	1.5	27.4	28.9	0.004	0.007
RA01-294/321	600	-4	6.92×10^{-5}	0.10	11.0	3.05×10^{-3}	3.80	1.00×10^2	1.39	55.13	4.5	41.4	45.8	0.006	0.004
RC31-505/532	600	-4	1.74×10^{-4}	0.18	7.59	5.32×10^{-3}	3.94	4.81×10^1	2.25	56.62	7.4	16.1	23.6	0.008	0.005
RC29-488/515	600	-4	6.92×10^{-5}	0.12	8.71	3.31×10^{-3}	2.95	6.64×10^1	2.64	55.94	8.6	28.5	37.1	0.012	0.007
RA02-299/326	600	-4	1.10×10^{-4}	0.12	12.0	3.92×10^{-3}	5.00	1.64×10^2	0.42	55.19	1.4	39.3	40.7	0.004	0.003
RA01-131/158	600	-4	5.75×10^{-5}	0.14	13.2	1.32×10^{-3}	1.23	6.68×10^1	0.02	51.88	0.1	96.6	96.6	0.004	0.010
RA06-297/324	600	-4	2.00×10^{-5}	0.10	12.0	2.75×10^{-3}	1.85	6.68×10^1	0.19	50.07	0.6	128.2	128.8	0.007	0.002
RC29-283/310	600	-4	1.00×10^{-4}	0.14	11.0	3.00×10^{-3}	3.45	8.23×10^1	2.33	56.12	7.6	24.9	32.5	0.005	0.007
RA02-128/155	600	-4	4.79×10^{-5}	0.15	17.4	1.10×10^{-3}	1.50	8.59×10^1	0.01	50.88	0.0	114.0	114.0		

APPENDIX C: STATIC DETERMINATION OF YOUNG'S MODULUS IN SEA ICE

Numerous tests are being performed at CRREL to determine the mechanical properties of arctic sea ice. By far the most difficult measurement to obtain accurately has been the initial tangent modulus, given by the force displacement curve and interpreted as Young's modulus. The purpose of this appendix is to reemphasize a warning by Mellor (1983) that a reliable initial tangent modulus cannot be determined unless axial strain measurements are made directly on the test specimen.

In unconfined, uniaxial, constant-strain-rate compression tests, we successfully determined the initial tangent modulus by mounting direct current displacement transducers (DCDTs) directly on the ice sample (Mellor et al. 1984). Two DCDTs were located in the center portion of the sample, measuring the axial displacement over a gauge length of 14 cm (5.5 in.). The output of the transducers was averaged and recorded on an $x-y$ plotter and strip chart. An extensometer was also used to measure full-sample axial displacements and to provide a control signal for the closed-loop testing system. This extensometer, mounted between the bonded end caps of the sample, measured displacements over a length of 25.4 cm (10 in.). The ice-mounted DCDTs were not used to control the strain rate because each test was designed to measure force-displacement characteristics to 5% full-sample strain. At these large strains the sample undergoes gross deformations, making the readings from the DCDTs unreliable. Measurements from both the DCDTs and the extensometer were reliable to $\pm 0.5\%$ of the reading for axial displacements greater than 2.54×10^{-3} mm (0.0001 in.). The axial strain measurements recorded by the DCDTs and the extensometer agreed very well up to peak load. The initial tangent modulus value was determined for each test using the initial slope of the force-displacement curve as recorded by the average of the DCDT measurements. Using the tangent modulus, we defined a Young's modulus which, on an average, agreed quite well with previous results (Cox et al. 1984).

We were also interested in investigating the effect of confinement on the compressive behavior of sea ice. This included the influence that confinement might have on the initial tangent modulus. A conventional triaxial cell (see Fig. 29) was developed for maintaining a constant ratio between the applied axial stress and the confining pressure ($\sigma_1 > \sigma_2, \sigma_3; \sigma_2 = \sigma_3; \sigma_2/\sigma_1 =$ constant). On-ice axial displacement measurements were complicated by the fact that the ice sample was to

be completely immersed in a high-pressure fluid. Considering the favorable agreement between the full-sample (extensometer) and on-ice (DCDTs) axial displacement measurements in the uniaxial tests, we felt that a feasible alternative would be to measure the full-sample strain externally.

This alternative meant, however, that the recorded displacements would include ice end effects, end cap compression and closure across an interface. The end cap compression was minimized by using aluminum end caps, which were very stiff relative to the ice. The interface of closure occurred between the loading piston and the top end cap of the sample. At this interface, we often had an imperfect contact because of a lack of parallelism in our machined samples. To correct for any lack of squareness, we measured the variation in sample height by running a comparator around the perimeter of the top end cap. Steel shimstock of the required gauge was then placed at the low point of the top end cap. Earlier evaluation of the uniaxial compression tests indicated that the use of shimstock was an effective means of compensating for the machining error.

It was still necessary to test the reliability of the external measurement more thoroughly. A series of three uniaxial compression tests was performed on ice samples at $-10°C$. Two of the samples were tested at a constant strain rate of 7.14×10^{-6} s^{-1}, and one was tested at a rate of 7.14×10^{-4} s^{-1}. The ice samples were instrumented with DCDTs and an extensometer as described earlier. In addition, a pair of extensometers was mounted between the loading ram and the top end cap as shown in Figure C1. These extensometers were 180° apart, with one extensometer located at the low point of the upper end cap. Axial displacement measurements were recorded by the DCDTs mounted on the ice sample, the extensometer mounted between the bonded aluminum end caps and the extensometers mounted across the shimmed interface. A comparison was then made of the initial portion of the force-displacement curves using 1) the DCDT output and 2) the full-sample extensometer output plus the displacement measurement across the shimmed interface. The latter curve simulated the axial displacements that would be obtained using the externally mounted extensometers on the triaxial cell.

The results are presented in Table C1, and Figure C2 shows a representative pair of curves. The initial tangent modulus values reported in Table C1 were defined by the initial slope of the record-

ed force–displacement curve. $E_i(GL)$ represents the modulus value determined using the axial displacement measured by the ice-mounted DCDTs, and $E_i(FS+P)$ is the modulus value determined using the full-sample and interfacial displacements. The percent reduction indicates the effect that external measurement techniques would have on the modulus value. The squareness value denotes the comparator readings on each sample and hence the shimstock used to correct for machining error. It is apparent that while the displacement across the shimmed interface is small, it is significant during the initial portion of the test, where displacements in the ice are also small. If we used the externally mounted extensometers in the triaxial tests, we could expect the initial tangent modulus value to be reduced to as much as one half the value that would be obtained in a uniaxial compression test on the same sample. As the axial force increases, the ice displacement continues to increase while the displacement across the shimmed interface remains constant. Therefore,

the closure has a significant influence only during the initial portion of the test. Measurement of the displacement between the loading ram and the top end cap indicates that the shimstock reduces the net closure at this interface to less than 0.051 mm.

These tests do indicate that displacement measurements made on the ice itself are necessary for reliably determining the initial tangent modulus, and hence Young's modulus. As a result of this study, modifications will be made to our triaxial cell so that it can accommodate an instrumented sample. Displacement transducers that can withstand high pressures, low temperatures and immersion will be used to measure the axial strain. These transducers will be mounted on the ice and the electrical signals that they transmit will pass through bulkhead connectors located in the cell wall. Once these changes have been completed, tests will be performed on ice samples to demonstrate the reliability of the displacement measurements.
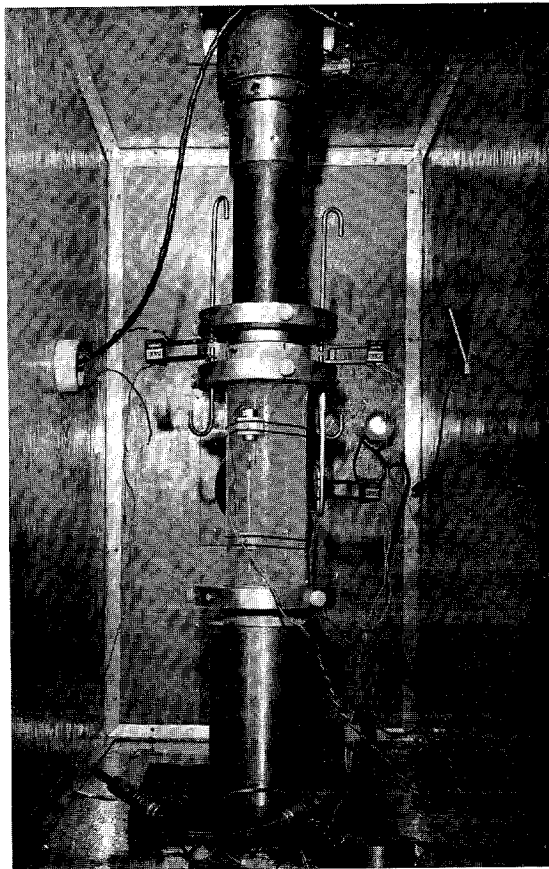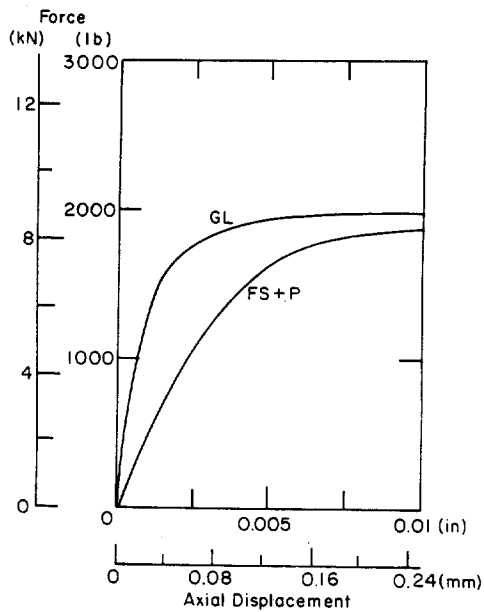

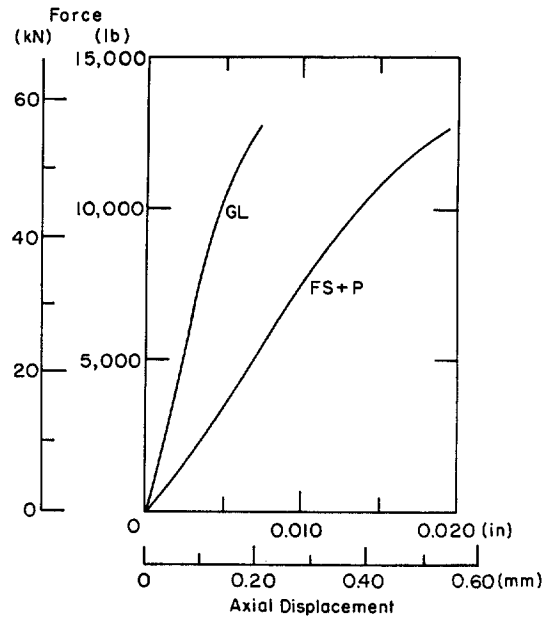*Figure C1. Test configuration to determine effect of closure.*

Table C1. Test results.

Sample no.	E_i(GL) (GPa)	E_i(FS + P) (GPa)	Reduction (%)	Squareness (mm)
$\dot{\epsilon} = 10^{-5}$ s^{-1}, $T = -10°$C				
12B	5.61	3.24	42	0.178
14C	5.14	4.26	17	0.229
$\dot{\epsilon} = 10^{-3}$ s^{-1}, $T = -10°$C				
1C	7.19	4.53	37	0.076

a. Sample 12B ($T = -10°C$, $\dot{\epsilon} = 7.14 \times 10^{-6}$ s^{-1}).   *b. Sample 1C ($T = -10°C$, $\dot{\epsilon} = 7.14 \times 10^{-4}$ s^{-1}).*

Figure C2. Force–displacement curves.

A facsimile catalog card in Library of Congress MARC
format is reproduced below.